

Abstract

The aim of this thesis is to study the growth and the properties of metallic nanostructures on vicinal surfaces. Coverages between 0 and 3 monolayers are studied. The thesis focuses on the formation of single atomic rows at the substrate steps, monolayer formation and the occurrence of alloying between adsorbate and substrate.

The decoration of Pt(997) and Pt(779) surfaces by Ag is well characterized from earlier studies [Gambardella *et al.* Phys. Rev. **B 61**, 2254 (2000)] and is employed here to obtain information on the role which steps play in the sticking behavior of O₂, H₂, and CO adsorbing from the gas phase. These molecules preferentially occupy step sites. The Ag decoration allows to change the electronic structure at the step edges without changing the substrate morphology. It is found that the sticking coefficient of H₂ and O₂ are drastically reduced for a Ag coverage of 13% (one Ag row covering the Pt step completely) while no significant change for CO adsorption is observed. The modification of the step affects all three adsorbates and the marked differences in observed adsorption can be rationalized by the details of adsorption path and energy barriers. In the case of O₂ the reduced sticking probability is due to a change of the chemisorbed molecular precursor state: Ag decoration shifts the partitioning between desorption and dissociative adsorption towards desorption. For H₂ it appears likely that a changed adsorption site is at the origin of the reduced sticking probability as it is found that preferential adsorption after Ag decoration is no more close to the step edges. The adsorption energy of CO is reduced by Ag step decoration which, however, does not affect the sticking probability in a significant way.

The growth of metals on the vicinal surfaces is investigated for the elements Fe, Mo, and Rh. Over a limited temperature range Fe and Rh exhibit monatomic row growth and

monolayer formation, whereas Mo grows in a three-dimensional growth mode. Mo is the first metal for which a monatomic row with low defect density cannot be prepared. For Fe deposition on Pt(997) at temperatures around 500K the formation of a surface restricted alloying is found. The kinetics of the alloying process are investigated and diffusion barriers of 0.32eV and 0.66eV have been obtained. The elementary processes associated with these barriers may be Pt-Fe exchange at the step edge or the creation of vacancies in the substrate terrace.

We studied the growth of ordered Cu-Ag and ordered Ag-Cu structures at the substrate step edges. While the deposition of Ag at a Cu pre-covered step edge results in an energetically stable structure with high reflectivity (200K - 300K sample temperature), also the reversed elemental order at the step can be obtained. This agrees well with a theoretical study [Gambardella & *al.* Phys. Rev. **B 64**, 045404 (2001)] which suggest that the second case which does not result in the arrangement with the lowest total energy can still be obtained as a metastable structure.

We finally demonstrate that the diffractive analysis spectrometer integrated in the He scattering set-up is working and reaches a relative energy resolution of better than 1.3%.

Version abrégée

Le sujet de cette thèse est l'étude de la croissance et des propriétés de nanostructures métalliques sur des surfaces vicinales. Des recouvrements allant de 0 à 3 mono couches sont étudiés. Cette thèse se concentre sur la formation de rangées monoatomiques le long des marches du substrat, la formation de mono couches et l'apparence d'alliage entre adsorbat et substrat.

La décoration de surface de Pt(997) et Pt(779) est bien caractérisée par de précédentes études [Gambardella *et al.* Phys. Rev. **B 61**, 2254 (2000)] et est employée afin d'obtenir des informations sur le rôle que joue les marches dans l'adsorption de O₂, H₂ et CO depuis la phase gazeuse. Ces molécules occupent de préférence les sites à la marche. La décoration par l'Ag permet de changer la structure électronique à la marche sans changer la morphologie du substrat. On a trouvé que le coefficient d'adsorption d'H₂ et d'O₂ est drastiquement réduit pour un recouvrement de 13% (une rangée d'Ag recouvrant complètement la marche) alors qu'aucun changement significatif ne fut observé pour l'adsorption du CO. La modification de la marche affecte les adsorbats (H₂, O₂ et CO). La claire différence observée dans l'adsorption peut être expliquée par les détails du chemin d'adsorption et la barrière en énergie. Dans le cas de l'O₂, la réduction de la probabilité d'adsorption est due à un changement de l'état du précurseur moléculaire chimisorbé. La décoration par Ag pousse la répartition entre désorption et dissociation du côté de la désorption. Pour H₂, il apparaît probable qu'un changement du site d'adsorption est à l'origine de la réduction du coefficient d'adsorption car après la décoration des marches par Ag le site d'adsorption ne se trouve plus préférentiellement à la marche. L'énergie d'adsorption du CO est réduite par la décoration des marches par l'Ag. Cependant cette réduction de l'énergie d'adsorption n'altère pas de façon significative la probabilité d'adsorption.

La croissance de métaux sur des surfaces vicinales est étudiée pour les éléments Fe, Mo et Rh. Pour un domaine de températures limitées Fe et Rh forme une rangée monoatomique ainsi qu'une mono couche alors que le mode de croissance de Mo est tridimensionnel. Mo est le premier métal pour lequel une rangée avec une faible densité de défauts ne peut pas être préparé. Lors de la déposition de Fe sur Pt(997) à des températures proche de 500 K la formation d'un alliage limité à la surface est observée. La cinétique du processus d'alliage est étudiée et des barrières de diffusion de 0.32eV et 0.66eV sont obtenues. Les processus élémentaires associés à ces barrières peuvent être soit l'échange Pt-Fe à la marche soit la création de lacunes dans la terrasse du substrat. Nous avons étudié la croissance de structures ordonnées de Cu-Ag et Ag-Cu aux marches du substrat. Alors que la déposition de l'Ag à une marche pré-decorée par du Cu résulte en une structure énergétiquement stable avec une haute réflectivité (température de l'échantillon 200K – 300K); de plus l'ordre inverse peut aussi être obtenue à la marche. Cela est en accord avec une étude théorique [Gambardella & *al.* Phys. Rev. **B 64**, 045404 (2001)] qui suggère que le second cas qui ne résulte pas en l'arrangement ayant l'énergie totale la plus basse peut encore être obtenue comme structure métastable. Finalement nous démontrons que premièrement le spectromètre à analyse par diffraction qui a été intégré dans le dispositif de diffraction de He fonctionne; et deuxièmement que sa résolution relative en énergie est supérieur à 1,3%.

Contents

Abstract	i
Version abrégée	iii
Contents	v
CHAPTER 1	1
Introduction.....	1
CHAPTER 2	5
Helium scattering.....	5
2.1 Introduction.....	5
2.2 Principles	6
2.3 Applications	8
2.3.1 Structure determination.....	8
2.3.2 Determination of growth modes	10
2.3 Study of surface dynamics	13
CHAPTER 3	15
Experimental set up	15
3.1 Introduction.....	15
3.2. The He source	16
3.3 The sample chamber	18
3.4 The detection unit	19
CHAPTER 4	21
Vicinal surfaces as template	21
4.1 Introduction.....	21
4.2 Pt vicinal surfaces	22
4.3 Diffraction patterns	24
4.4 Growth on vicinal surfaces	26

CHAPTER 5	31
Modification of the Pt step reactivity by Ag deposition.....	31
5.1 Introduction.....	31
5.2 The reactivity of decorated steps	34
5.3 Adsorption of oxygen	36
5.4 Adsorption of carbon monoxide	43
5.5 Adsorption of hydrogen	45
5.6 Conclusion	46
CHAPTER 6	47
Fe growth on Pt (997)	47
6.1 Introduction.....	47
6.2 Experimental	48
6.3 Results.....	48
6.3.1 Row formation	48
6.3.2 Layer formation	50
6.3.3 Growth below 450K.....	52
6.3.3 Alloying	58
6.4 Conclusions.....	63
CHAPTER 7	65
Mo and Rh growth on Pt(997)	65
7.1 Introduction.....	65
7.2 Experimental	66
7.3 Results.....	66
7.3.1 Mo growth.....	66
7.3.2 Rh growth	71
7.4 Conclusions.....	75
CHAPTER 8	77
Ag-Cu bimetallic wires.....	77
8.1 Introduction.....	77
8.2 Experimental	79
8.3 Results.....	82

8.3.1 Ag/Cu-row/Pt(997)	82
8.3.2 Cu/Ag-row/Pt(997)	84
8.4 Discussion and Conclusion	86
CHAPTER 9	87
New energy analysis detector	87
9.1 Introduction.....	87
9.2 Detector set up	88
9.3 Energy analysis	89
9.3 Calibration of the detector	92
9.4 Results.....	94
CHAPTER 10	97
Conclusions and Outlook.....	97
References.....	99
Remerciements.....	105
Curriculum Vitae	107

CHAPTER 1

Introduction

Surfaces play a fundamental role in many aspects of technology such as corrosion or catalysis. The fabrication of well-defined surfaces and interfaces is also crucial to the performance of microelectronic devices. The need to grow smaller and smaller structures and to understand the new physical phenomena occurring in reduced dimensions [1] have been two reasons behind the efforts of the last decades to understand phenomena occurring at surfaces and interfaces. This includes the investigation of magnetic and electronic properties and their coupling (e.g. giant magneto-resistance). Of particular interest to present research is the controlled fabrication of structures with lateral dimensions reaching down to the nanometer scale and the control of their size and shape. Generally, the fabrication of nanostructures can be achieved by top-down or bottom-up strategies. The top-down strategies try to create smaller and smaller structures by improving the lithographic techniques. The bottom-up approach, in contrast, takes advantage of the strong influence of the morphology of the surface on the growth of adlayers. A surface with a pre-defined structure can be used as a template to grow specific structures. This bottom-up approach uses processes occurring on the atomic scale such as diffusion on the surface or preferential nucleation at step-edges and at kink sites. An example of this bottom-up approach is e.g. the use of a domain wall network exhibited by the second layer of Ag grown on Pt(111). These domain walls act as diffusion barrier supporting the growth of nanometer islands with a narrow size distribution [2].

Another class of templates are formed by vicinal surfaces. A Pt(997) surface can be prepared to exhibit an array of regularly spaced monoatomic steps with an average step distance of 2.02 nm. This corresponds to terraces consisting of only eight rows of atoms. The standard deviation of the width is only about one atomic row. The terraces form a closed packed structure similar to the Pt(111) surface. The stability of the vicinal surface is due to the repulsive interaction between the steps. Throughout this thesis the Pt(997) and Pt(779) surfaces are used as templates to study the growth of adsorbate structures like e.g. nanowires [3].

The thesis contains the following sections:

Chapter 2 and 3 present the method which is primarily employed to study nanostructure growth at vicinal surfaces, namely Thermal Energy Atom Scattering (TEAS). The diffracted intensity gives us information about the structure of the surface. The evolution of the diffracted intensity with time provides us with information on the growth mode of deposited adsorbates.

Chapter 4 describes the Pt(997) and Pt(779) surfaces in more detail: Their morphology, their diffraction patterns, and how information on growth modes is obtained on vicinal surfaces.

In chapter 5 we study the sticking coefficient of O₂, H₂, and CO for a Ag pre-covered substrate. Ag decorates the substrate steps with continuous, monatomic rows. In contrast to Pt, Ag is a comparatively inert metal with respect to catalytic activity, and one can expect that the adsorption of gases can be strongly modified.

It was reported that Co monatomic wires are superparamagnetic and show hysteresis at very low temperatures (< 15K) [1]. When approaching nanometer dimensions the magnetic properties of a material can drastically depend on the size of the structure. Detailed studies of the properties (e.g. magnetic moments) require, however, a precise knowledge of the morphology of the structures. In chapter 6 we study the growth of Fe on Pt(997). The aim is to determine the conditions which allow to prepare the sample in different well-defined structures (monolayers, nanowires, or alloys).

In chapter 7 we study the growth modes of Rh and Mo on Pt(997). These two elements, which are non-magnetic as bulk crystals have been predicted to exhibit a magnetic

moment when they form small cluster or nanowires on the surface of Ag (001) [4]. It is for this reason that it is of interest to study their growth on surfaces.

A recent theoretical study suggested that it may be possible to grow bimetallic nanowires by depositing Cu on a Pt(997) surface on which the steps were pre-covered by a monatomic row of Ag [5]. This arrangement is not energetically stable but metastable. Only deposition in the reverse order (first Cu, then Ag) corresponds to the stable structure. In chapter 8 we investigate these two deposition orders and characterize the observed behavior.

In the last chapter (chapter 9) we present a first spectrum measured by an energy analysis detector based on the new concept of diffraction from a Pt(997) surface. This Diffractive Analysis Spectroscopy (DAS) may replace conventional Time of Flight (TOF) spectrometry.

CHAPTER 2

Helium scattering

2.1 Introduction

The methods employed to study surface properties can be divided into two main groups: The first group comprises the methods probing surfaces locally, some even on the atomic scale. They give information on a small region of the surface typically (less than $1 \mu\text{m}^2$). Among these methods one finds Scanning Tunneling Microscopy (STM) and Atomic Force Microscopy (AFM). They give real space images of the studied surface even though the interpretation of the images is not always straightforward because the contrast often is the result of different interactions. For example in the case of STM the image contains information on topography, the electronic density and the characteristics of the tips. It can be difficult to separate the different contributions. To get global properties of the surfaces those methods require the acquisition a large number of images.

The second group comprises the methods probing the surfaces on a larger scale (typically 1 mm^2). Apart from methods probing real space on this large scale, like e.g. angle resolved ion scattering, these methods are generally diffraction methods accessing data in reciprocal space coordinates. Diffraction methods can use various particles to probe the surface, e.g. electrons, photons, neutrons, and atoms. As the probed area is often larger than the largest structures resolvable by the diffraction technique the obtained information represents averaged properties of the surface. One of the methods belonging to this later group is Thermal Energy Atom Scattering (TEAS), which is the basic method employed in this thesis and which will be further introduced in the following sections.

2.2 Principles

In a He scattering experiment a monochromatic He atom beam generated by a supersonic expansion of He gas into the vacuum is directed towards a surface. The neutral He atoms impinge on the surface and the part of the beam scattered into a defined direction is detected. The energy of incident and detected beams be E_i and E_f , their wave vectors k_i and k_f , respectively (Fig. 2.1). The interaction between the incoming beam and the surface determine the intensity of the detected beam.

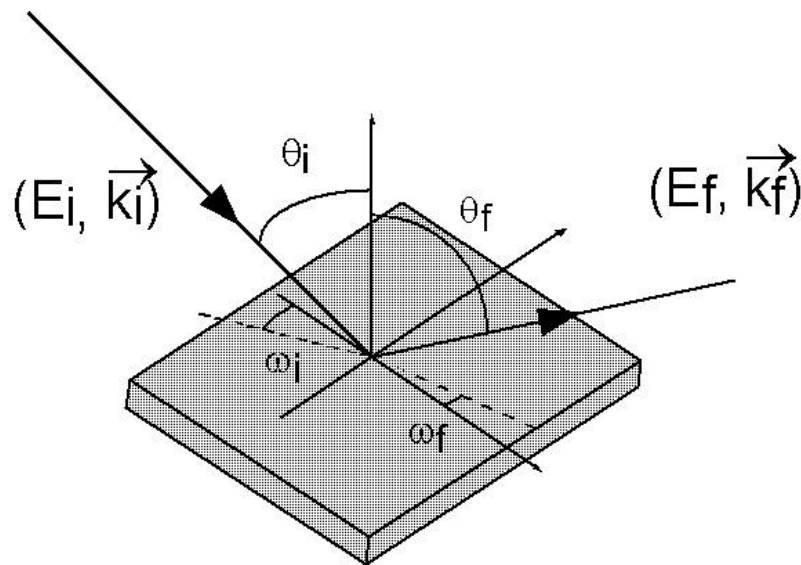


Fig. 2.1: Geometry in a He scattering experiment.

Information on the properties of the surface can be extracted by measuring the angular distribution of the scattered beam and the energy distribution in each geometry. From such measurements one can obtain information on the surface structure and surface dynamics (e.g. surface vibrations). By time dependent measurements one can study dynamic processes occurring at the surface and, during the adsorption of adsorbates, the growth mode of adlayers.

The energy of the impinging He-beam can be chosen between 10 meV and 100 meV depending on the temperature of the nozzle from which the beam is generated. Because of this low kinetic energy the He beam does not damage the surface. It does not induce

desorption even for weakly bound systems like physisorbed rare gases. The interaction between He atoms and the surface is dominated by two contributions: A weak long-range attractive potential due to Van der Waals-forces and a stronger short-range repulsive potential which is due to Pauli's exclusion principle and which prohibits that the electronic cloud of the He atoms overlaps with the electrons of the solid at its surface [6]. The reflection of the He atoms takes place, in a classical picture, about 3-4 Å above the surface atom cores. This prevents He atoms from penetrating the surface and makes He scattering an exclusively surface sensitive method.

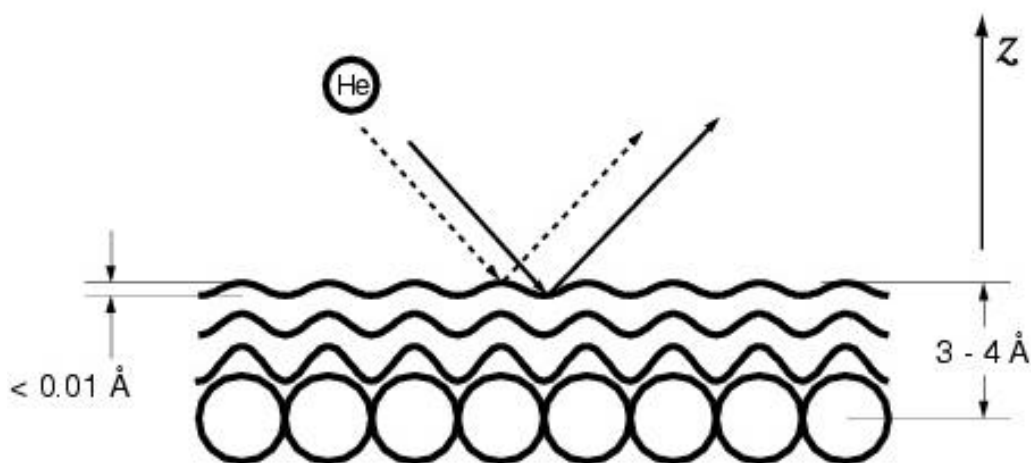


Fig. 2.2: He atom being reflected by the surface. The classical turning point is about 3-4 Å above the surface.

The corrugation of the repulsive potential, which is due to the periodic modulation of the electron density at the surface, is typically as low as 0.01 Å for metallic surfaces (Fig. 2.2).

Fig. 2.3 shows that energy and de Broglie wavelength of He atoms make them well-suited tools to study surfaces. First, the energy of a thermal energy beam is of the same order of magnitude as the energy of surface phonons. Second, the wavelength is slightly

smaller than inter-atomic distances and typical periodic structures at single crystal surfaces.

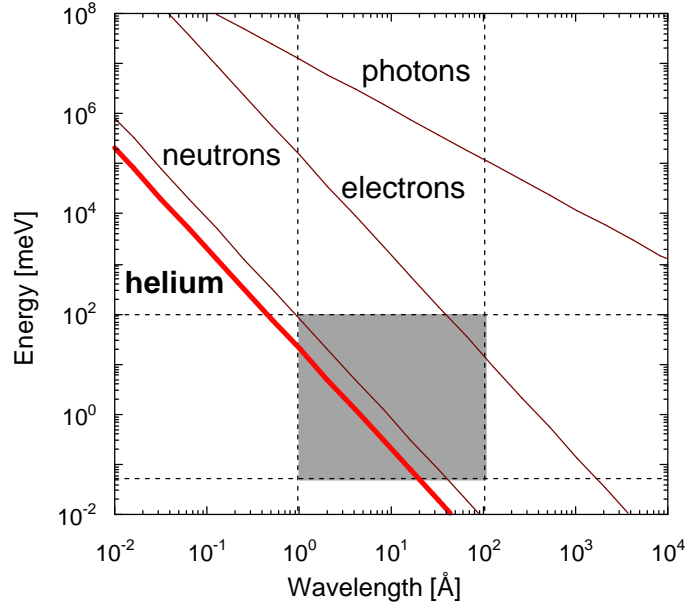


Fig. 2.3: Energy and associated wavelength of different particles. The shaded area corresponds to typical periodicities of surface structures (diffraction) and the energy of surface phonons (inelastic scattering).

2.3 Applications

2.3.1 Structure determination

TEAS is a powerful tool to determine the structure of a surface because the wavelength of the Helium beam is comparable to inter-atomic distances at the surface of a solid. As a result, the reflected He beam exhibits a diffraction pattern, which is defined by the energy of the Helium beam and the periodicity of the surface. For a simple 1-dimensional periodicity the position of diffraction peaks is given by:

$$d (\sin(\mathbf{q}_i) - \sin(\mathbf{q}_f)) = n \mathbf{l} \quad (2.1)$$

where q_i is the incident angle of the He beam, q_f is the angle of the diffraction peak, d is the period on the surface (e.g. the lattice constant), n is the diffraction order, and λ is the wavelength.

An example of a two-dimensional diffraction pattern is given in the Fig. 2.4. The Ni (110) surface is represented as a hard sphere model in 2.4 a, the reciprocal lattice is drawn under 2.4.b and the He diffraction pattern along the [110] direction is given in 2.4.c. The diffraction pattern corresponds to a cut in reciprocal space. The angle between the specular peak (00) and the first order diffraction peak (01) allows the determination of the reciprocal lattice vector \mathbf{b}_2 . By rotating the sample by 90° and measuring another scan the reciprocal vector \mathbf{b}_1 can be determined. With these two vectors one can then calculate the lattice vectors in real space \mathbf{a}_1 and \mathbf{a}_2 .

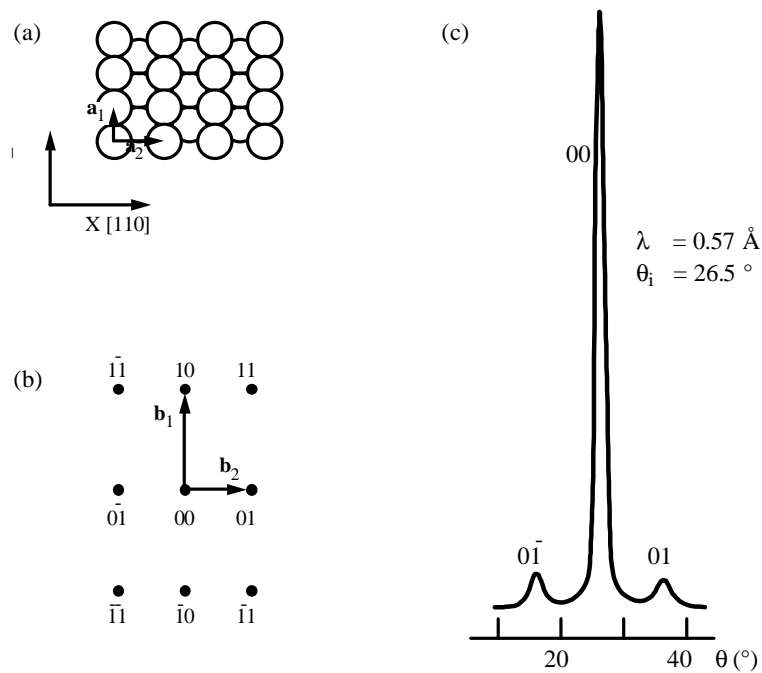


Fig. 2.4: (a) Hard sphere model of the Ni (110) surface (b) reciprocal lattice (c) He diffraction spectrum, taken in the direction [110], showing the specular reflection and the two first order diffraction peaks (from Ref [7]).

2.3.2 Determination of growth modes

During the deposition of adsorbates on a surface the incoming atoms or molecules can change the surface morphology. By recording the intensity of a diffraction peak during the deposition we can obtain information on these changes and thus study in detail the growth of the adsorbate layer [6, 8].

The sensitivity of TEAS to the growth modes results from the large cross section of surface defects (kinks, adatoms, vacancies...) for diffuse scattering [6] and from the monochromaticity of the beam which allows interference of beams reflected from adjacent regions on the surface. Defects induce a strong local perturbation of the weakly corrugated potential of a plain surface. The perturbation reduces the intensity in the diffracted peaks and increases the He intensity scattered diffusely.

Figure 2.5 shows a sketch of a single adsorbate on a flat surface. Atoms impinging in region I are reflected specularly and scatter into the detector positioned in this case on the specular (i.e. zeroth order) diffraction peak. Atoms coming from region II are deviated by the attractive part of the potential whereas atoms from region III are deviated by the attractive and the repulsive part of the potential. Atoms impinging into regions II and III are thus removed from the specular beam when the defect is created.

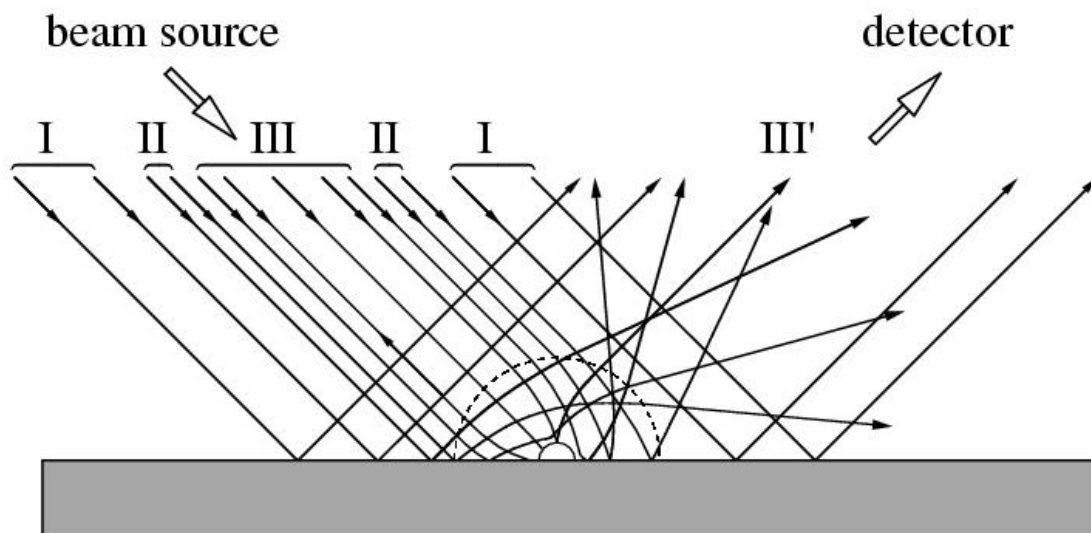


Fig. 2.5: Diffuse scattering from a single adsorbate on a flat surface, (from Ref. [6]). The solid half circle represents the repulsive potential and the dashed half circle represents the attractive potential.

The attractive part of the potential is thus essentially responsible for the high sensitivity of TEAS to the existence and generation of defects. It results in cross sections for diffuse scattering of the order of 100 \AA^2 [6].

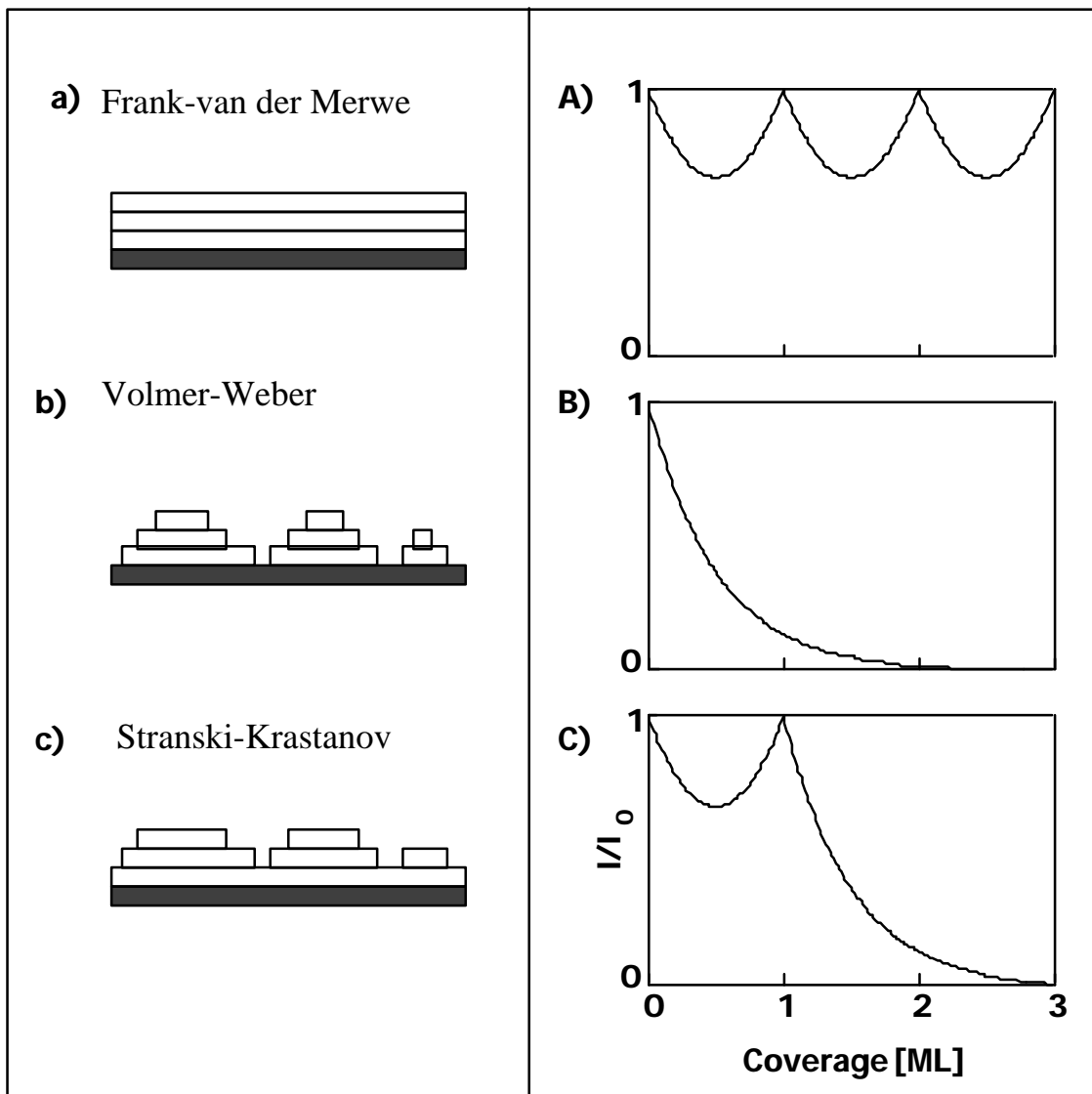


Fig.2.6: Three principal growth modes and the corresponding variation of diffracted intensity during evaporation in an in-situ experiment.

During the deposition of adsorbates the number of defects can change. Recording the intensity in a diffraction peak as a function of time helps to determine the prevailing growth mode of the adsorbate. Generally, three distinct growth modes are known:

- a) Frank-van der Merwe growth, 2-D growth or layer-by-layer growth
- b) Volmer-Weber growth or 3-D growth
- c) Stranski-Krastanov growth.

These growth modes are illustrated together with the corresponding variation of He reflectivity in Fig. 2.6.

In the layer-by-layer growth mode (Figure 2.6a) the defect density oscillates with the number of created layers in such a way that it is at a minimum for a complete layer and a maximum for a half completed layer. The reflected intensity varies correspondingly in a periodic fashion with a minimum corresponding to a high density of defects and a maximum corresponding to a minimum of defects i.e. a completed layer.

A special case of 2-D growth can occur on surfaces with high step density. If the adsorbates are exclusively attaching to substrate steps, the layers grow in a step flow growth mode and the defect density may essentially stay constant. In that case no oscillation in intensity will be observed during growth. In the ideal case it will even stay constant during the adsorption of several layers.

For the 3-D growth mode (Figure 2.6b) the defect density increases monotonically and the He intensity decreases continuously (often exponentially). In this growth mode the adlayer forms three-dimensional structures on the surface with a large number of layers exposed at the surface.

For the Stranski-Krastanow growth mode (Figure 2.6c) the growth starts like a 2-D growth until a critical thickness is reached after which the growth continues in the 3-D mode. If e.g. the critical thickness corresponds to one monolayer the He intensity reaches a maximum at that coverage and then decreases continuously. The change in behavior, which occurs for this growth mode, is due to the relaxation of strain in the overgrown layer.

The density of defects is not the only factor that results in intensity changes during adlayer growth. The interference condition between surface areas with different heights

also determines the observed reflectivity. One may regard two atomically flat areas separated by steps as e.g. an adatom island on a flat terrace. Two limiting cases can be considered: First, the beams reflected from two different levels are interfering constructively (in phase condition); second, they may interfere destructively (anti-phase condition). In the anti-phase condition the signal can become zero in the ideal case when a coverage of half a monolayer is reached. For the in-phase condition the decrease in intensity is only due to the presence of defects created during the growth and thus corresponds to the case discussed in detail above.

2.3 Study of surface dynamics

Inelastic scattering experiments allow accessing vibrations at a surface and thus open up a way to study elastic properties of the surface and analyze the coupling within adlayers and between adlayer and substrate. Such studies are based on the determination of phonon dispersion relations along high symmetry directions of the system. The basic requirement for this is the determination of energy and momentum transfer between the scattered He atoms and the surface for a large number of geometries [9-11]. The new energy analyzer described in Section 9.2 was developed in order to make this type of energy analysis and record inelastic spectra. The momentum transfer is then simply calculated from energy transfer and the chosen scattering geometry. As no measurements of inelastic scattering from a surface are reported in this thesis, the inelastic scattering is not discussed in more detail here.

CHAPTER 3

Experimental set up

3.1 Introduction

The He scattering apparatus (Fig. 3.1a,b) introduced in this chapter allows performing diffraction measurements with monochromatic He beams. It was initially designed and built by V. E Marsico and H. Schief during their PhD thesis [12, 13] and provides in addition standard ultra-high vacuum preparation and characterization tools. A special feature for He scattering is the highly variable geometry, which allows varying independently the incidence and exit angle over a wide range without breaking the vacuum, and while diffraction measurements can be continued. The total scattering angle $\theta = \theta_i + \theta_f$ can be varied between 59° and 181° . A second feature is the realization of a new concept for energy analysis of the scattered He beam, a concept that will be discussed separately in chapter 8. The set-up was optimized to monitor in-situ the growth of adlayers for varying scattering geometries.

The apparatus consists of three functional parts that define the subjects of the following three sections (3.2-3.4). The functional parts are separated from one another by ultra-high vacuum (UHV) valves which remain UHV-tight with atmospheric pressure on one side so that each part of the apparatus can be vented independently. This allows doing repairs on one chamber without having to vent the whole system. The He beam is created by a source in the nozzle chamber from where the beam passes to the sample chamber. In the sample chamber the beam hits the sample and is scattered. The scattered beam is detected into the third part containing an electron impact ionization detector.

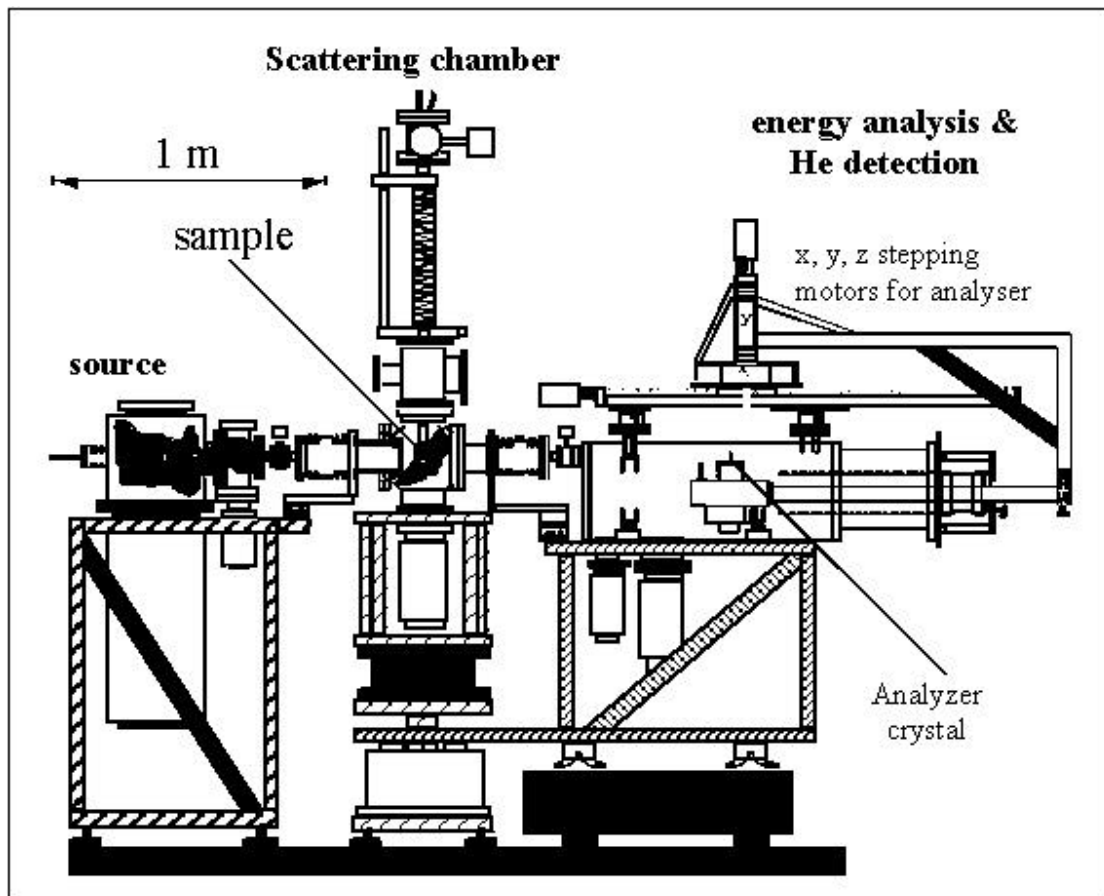


Fig. 3.1a: Instrument side view.

3.2. The He source

The He beam is generated in chamber I by a nozzle [14] with an aperture of 10 μ m diameter. Its temperature can be stabilized between 50K and 350K by resistive heating against the constant cooling power by a helium cold head coupled via a copper braid. Depending on the selected temperature the stagnation pressure in the tube that ends in the nozzle is chosen between 100 and 300 bars. The limiting parameter for the stagnation pressure is the pressure in the vacuum chamber where the nozzle is located and in which the vacuum is sustained by a 6000 l/s diffusion pump. The diffusion pump is boosted by a roots pump. In chamber I the pressure is about 10⁻⁵ mbar.

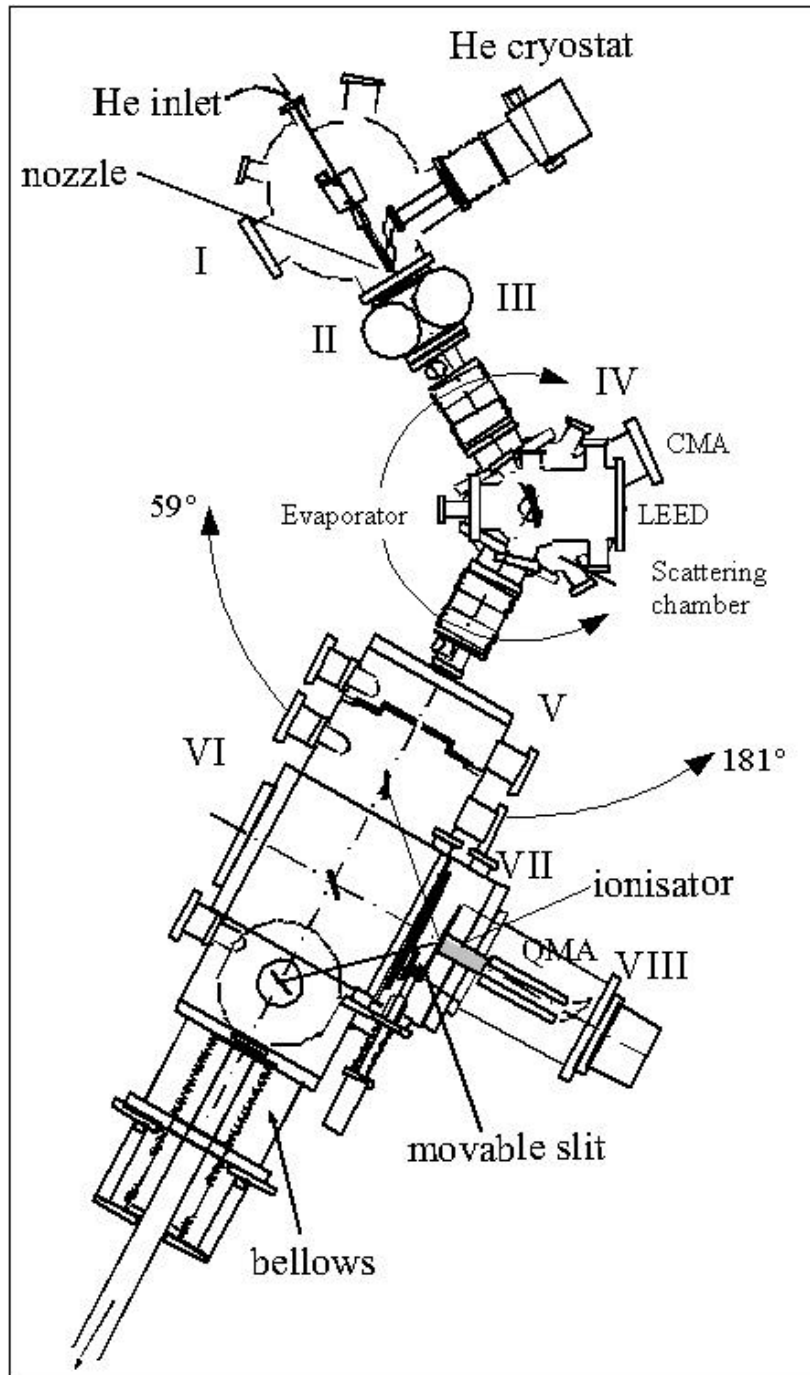


Fig. 3.1b: Instrument top view.

Two skimmers (\varnothing 0.28 and \varnothing 0.20 mm) are located between chamber I and II and between chamber II and III, respectively. The skimmers collimate the supersonic beam and serve as apertures for the differential pumping states. The chambers II and III are

pumped each by a turbomolecular pump. A pinhole (\varnothing 0.23 mm) is located between chamber III and the sample chamber. The divergence of the beam (0.07°) is determined by the size of that pinhole. The wavelength of the He beam can be set between 0.5 Å and 1.5 Å (80 meV to 10 meV in energy) by adjusting the nozzle temperature. The monochromaticity of the beam, $\Delta E/E$, is typically 1.5%.

3.3 The sample chamber

The scattering chamber is mounted on a motorized rotary table (supplier: Franke GmbH). The precision of angular positioning is better than 0.01° . The axis of rotation defines the main axis of the instrument. The scattering chamber is connected to the nozzle chambers and to the detector chambers by flexible bellows. Those bellows allow to rotate the chamber by $\pm 30.5^\circ$ with respect to a "neutral position" in which there is no lateral strain on the bellows.

The sample is mounted on a manipulator with six degrees of freedom (three for linear positioning on the axis of the chamber and three angles for the surface orientation: tilt, polar angle, and azimuth). The sample can be cooled by a cooling finger through which a flow of liquid He or liquid nitrogen can pass. The sample is heated by electron bombardment from a tungsten filament close to its backside. To achieve temperatures up to 700K radiative heating from the filament is sufficient; for higher temperatures an accelerating voltage of 600V is applied between sample and filament. By use of liquid N₂ cooling the accessible temperature range for the sample is 100K to 1400K. Temperatures below 30K can be achieved using liquid He. The sample can be prepared by use of an ion sputter gun and several metal evaporators. Four different elements can be deposited when the sample is in the He scattering position (i.e. "in-situ"). In different sample positions the sample can be characterized by LEED (Low Energy Electron Diffraction) and AES (Auger Electron spectroscopy). A magnetic turbomolecular pump pumps the sample chamber. It is backed by a small turbomolecular pump necessary to achieve a sufficient compression ratio for He gas. The basic pressure in the sample chamber is 2×10^{-10} mbar.

Upon admitting the He beam into the chamber the ionization gauge indicates 1×10^{-9} mbar, which corresponds to an additional He pressure of approximately 6×10^{-9} mbar.

3.4 The detection unit

The differentially pumped chambers V to VIII contain the energy analysis and detection unit. The He background pressure must be reduced strongly in the chamber VIII where the ionization detector is located. The detection unit is mounted on a frame which rests on air cushions and which slides over a polished granite plate. It moves on a circle centered on the main axis of the sample chamber. A robotic rotary motor (Megatorque motor) drives the rotation. The detection unit can be rotated by $\pm 30.5^\circ$ with respect to the scattering chamber.

A Pt(111) and a Pt(997) crystal are mounted on a manipulator with six degrees of freedom (x, y, z, tilt, polar, azimuth). The precision of the displacements in x, y and z direction is $5 \mu\text{m}$, the precision of the polar angle is of $\pm 0.001^\circ$. The Pt(997) crystal can be employed as an energy analyzer (see chapter 9). In most of the measurements shown in this thesis, however, the Pt(111) surface is used for reflecting the He beam into the detector. To keep both surfaces clean over a long period of time the analyzer chamber VI is filled with an atmosphere of $5 \cdot 10^{-9}$ mbar of oxygen and $5 \cdot 10^{-7}$ mbar of hydrogen [13].

The electron beam ionizer situated in chamber VIII is based on a Pirani type manometer. It stores the incoming He flux for a short time and thus increases the ionization probability of the He atoms [15]. This set-up is more favorable for the new analyzer set-up than "open" ionizers because its detection efficiency depends on the angle of the incoming beam in a simple geometric way. For further details see chapter 9. The He ions created in the ionization chamber pass through a quadrupole mass spectrometer set to the mass $m=4$ (He) and are counted by a Channeltron multiplier. The background counting rate of the detector is about 30 counts/s. The contribution from the adjacent peak $m=2$ (H_2) is negligible. The counting rate of the He beam passing from the nozzle chambers directly into the analyzer-detection unit (without scattering from a sample) can reach 5 million count/s.

CHAPTER 4

Vicinal surfaces as template

4.1 Introduction

The morphology of a surface has a strong influence on the growth of adlayers. A surface with a pre-defined structure can be used as a template for the growth of specific adlayer structures. Such a bottom-up approach for nanostructuring has to make use of processes on the atomic scale, which are based on the properties of the surface. Bottom-up strategies have the advantage that large areas can be prepared uniformly and simultaneously. The use of different materials and the selection of temperature to activate certain diffusion processes and suppress others are one way to employ the laws of nature in order to generate desired structures. For instance, the domain wall network exhibited by the second layer of Ag grown on Pt(111) can be used as diffusion barriers, which help to grow nanometer islands with a narrow size distribution [2]. If such islands are, e.g. ferromagnetic they may be employed as units for magnetic information storage. Another example is the vicinal Mo surface on which wires with nanometer width have been grown [16] making use of the step decoration. For such structures arises the need to understand their physical properties in more detail and thus a fundamental interest for the creation and characterization of these structures: Even thinner wires than on Mo are obtained by step decoration on Pt(997) and Pt(779) surfaces [3, 17, 18]. In the limit, a perfectly regular array of one atom thick wires with large aspect ratios can be created on these surfaces if the template is prepared well and the growth conditions for the adsorbate are chosen properly. In this chapter we describe these two vicinal Pt surfaces, which are used

as templates throughout this thesis. We then discuss how TEAS can be employed to study the growth of adsorbates on these surfaces.

4.2 Pt vicinal surfaces

Pt(997) and Pt(779) (Fig. 4.1) are both surfaces with a regular step array. They have monatomic steps of $h = 2.27 \text{ \AA}$ height separating Pt(111)-like terraces of approximately 20 \AA width. The surface of Pt(997) is obtained by cutting a Pt single crystal so that the surface normal is $\alpha = 6.45^\circ$ ($\alpha = -7.01^\circ$ for Pt(779)) off the [111] direction. The step periodicity d of the two surfaces is slightly different: $d = 20.2 \text{ \AA}$ for the (997), and $d = 18.6 \text{ \AA}$ for the (779) surface. The main difference between the surfaces is the different step geometry. The steps on the (997) surface have (111) micro-facets whereas the steps on the (779) have (110) micro-facets. It is of interest to study surfaces with different step structures because these may influence the adsorbate growth and the chemical reactivity of the surface (see chapter 5).

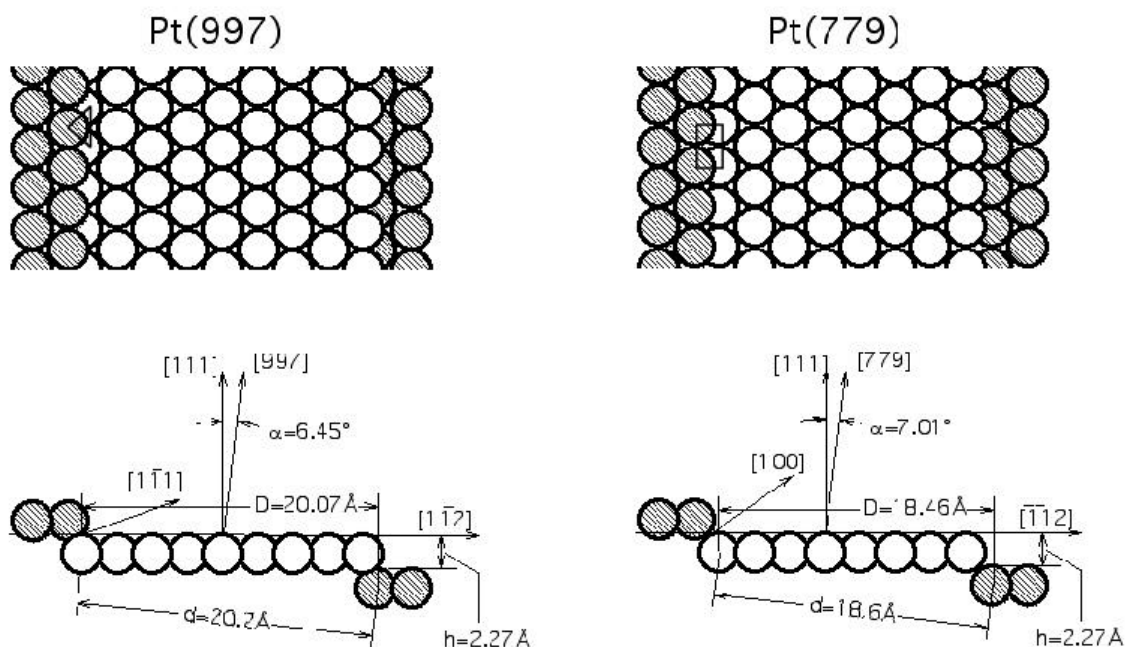


Fig. 4.1: Structure of the Pt(997) and the Pt(779) surface.

Fig. 4.2 shows an STM image of a well-prepared Pt(997) surface with almost perfect step periodicity. The high regularity of the terrace width can be explained by a repulsive interaction between steps [19]. The detailed analysis of the surface has shown a Gaussian distribution of the step-step distance with a root mean square deviation of one row. The best preparation is obtained by cycles of Ar^+ ion sputtering at a sample temperature of 750K followed by annealing at 900K. For new crystals repeated cycles of annealing are carried out in an oxygen (10^{-7} mbar) atmosphere to remove e.g. carbon segregating from the bulk at elevated temperatures.

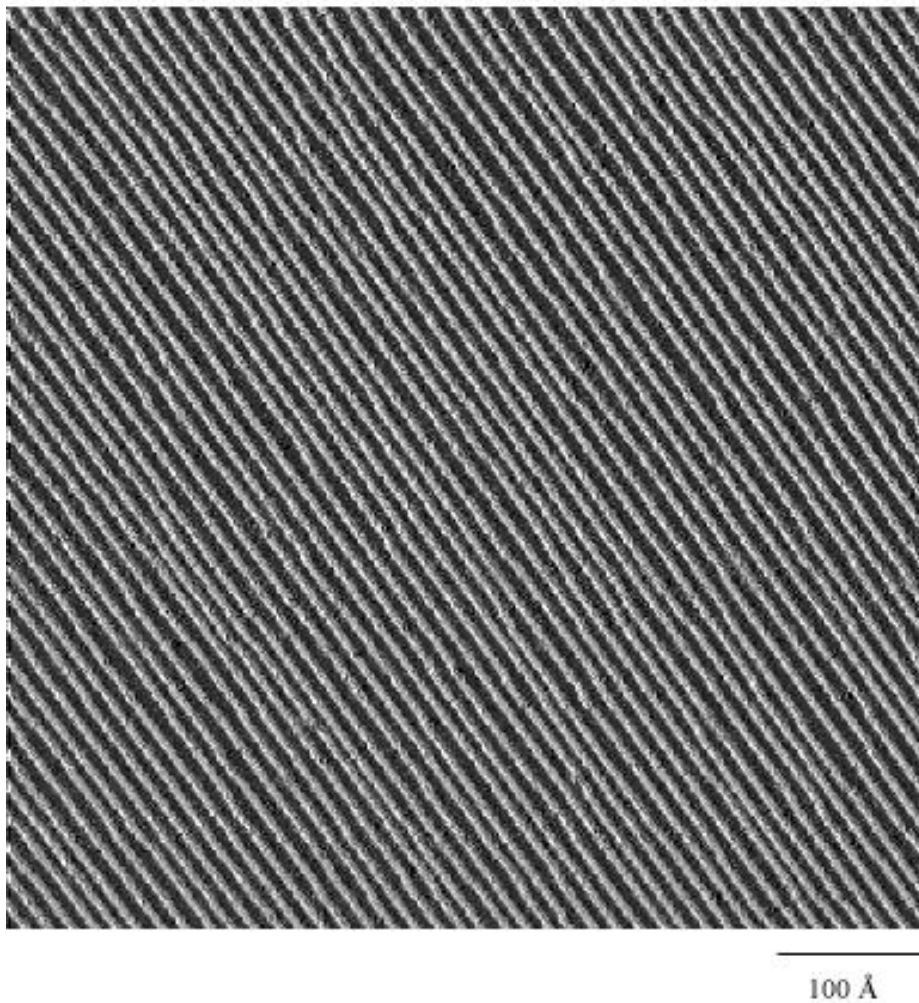


Fig. 4.2: STM image of a well-prepared (997) surface.

4.3 Diffraction patterns

In this section we discuss the diffraction pattern of the surface (997). The results can equivalently be applied to the geometry of the (779) surface [20].

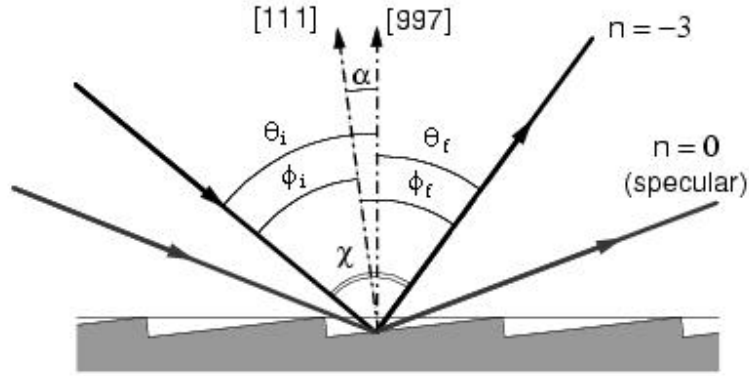


Fig. 4.3: Schematic diffraction pattern for a (997) surface.

The diffraction geometry is schematically shown in Fig. 4.3. The angles of the incident and diffracted beams, θ_i and θ_f respectively, are defined with respect to the [997] direction (normal to the macroscopic surface) and the angles ϕ_i and ϕ_f are defined with respect to the [111] direction (normal to the terraces) for scattering step down direction. θ and ϕ are linked by the miscut angle α as follows: $(\theta_i, \theta_f) = (\phi_i + \alpha, \phi_f - \alpha)$. The total scattering angle is given by $\chi = \theta_i + \theta_f = \phi_i + \phi_f$.

The He diffraction pattern obtained from these surfaces can be described by:

$$I = c \cdot A^2 \cdot G^2 \quad (4.1)$$

where I is the intensity of the reflected He beam, c is a normalization factor, A is the form factor for a single terrace, and G is the structure factor of the surface grating. I , A , and G are all functions of the incident and scattering angles.

The structure factor G gives the positions of the diffraction peaks. These positions can be calculated from the one dimensional Bragg equation:

$$\sin(\mathbf{q}_f) - \sin(\mathbf{q}_i) = \frac{n\lambda}{2d} \quad (4.2)$$

where λ is the wavelength and n is the diffraction order.

The function A describes the diffraction from a single terrace. It can be derived in analogy to the diffraction from a single slit.

$$A^2 = \frac{\sin\left(\frac{\mathbf{f}}{2}\right)}{\left(\frac{\mathbf{f}}{2}\right)} \quad (4.3)$$

$$\text{where } \mathbf{f} = \frac{2p}{\lambda} \tilde{D}(\sin(\mathbf{f}_i) - \sin(\mathbf{f}_f)) \quad (4.4)$$

λ is the wavelength and $\tilde{D} = h \cdot \left(\frac{1}{\tan \alpha} - \tan \mathbf{f}_i \right)$ is the effective length of the terrace. The factor in brackets takes into account the shadowing effect of the step [6].

To obtain (4.3) we assumed that the terraces are perfectly flat. This is reasonable for close-packed metallic surfaces due to their small corrugation (see chapter 2). However, if we want to take into account the atomic surface corrugation we have to write:

$$\sin(\mathbf{f}_f) - \sin(\mathbf{f}_i) = \frac{m\lambda}{2a} \quad (4.5)$$

where m is the diffraction order defined for a structure on the terraces with periodicity a , which may correspond, for example, to the distance between atomic rows on the (111) terraces.

If we choose the order $m=0$, i.e. specular scattering with respect to each terrace, then we obtain $\mathbf{f}_i = \mathbf{f}_f = \mathbf{f}$ and eq. 4.2 becomes

$$\cos(\mathbf{f}) = \frac{n\lambda}{2h} \quad (4.6)$$

In this so-called *ideal* condition all atoms on adjacent terraces scatter in phase. The width of the n^{th} peak reaches its minimum that is determined only by the instrumental resolution. An example of a diffraction pattern from a clean (997) surface is given in Fig. 4.4. The peak $n=-3$ is close to its ideal condition ($m=0$) while the diffraction orders $n=-2$

and $n=-4$ are substantially broadened. This broadening reflects the deviation from a perfectly periodic step arrangement.

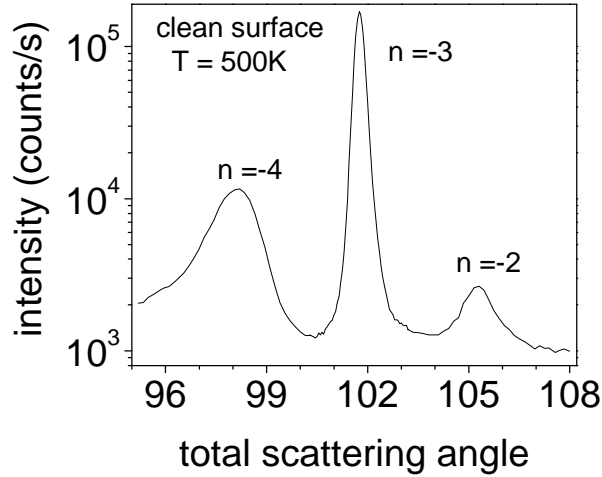


Fig. 4.4: Diffraction pattern for a clean Pt(997) surface. $q_i = 57.8$, $l_{\text{He}} = 1.01 \text{ \AA}$

4.4 Growth on vicinal surfaces

In chapter 2 different growth modes on flat surfaces have been discussed. Because of their high step density the growth on vicinal surfaces can exhibit a larger variety of features in both, the growth modes and the corresponding variations in He reflectivity. Basic crystallography tells us that in the case of cubic geometry the distance between two planes indexed by the Miller indexes (hkl) , $d(hkl)$, is given by

$$d(hkl) = \frac{a}{\sqrt{h^2 + k^2 + l^2}} \quad (4.7)$$

The interplanar spacing reduces when the Miller indexes of the planes increase [21]. At the same time the number of atoms belonging to each layer reduces. In fact, a complete atomic plane on a vicinal surface like Pt(997) consists of a single row of atoms attached to all steps on the surface. In this case new plane thus corresponds to only 13% of the atoms required for a plane on Pt(111). Accordingly, one may expect that layer-by-layer growth for the vicinal surface is reflected in intensity oscillations with maxima at completion of one additional crystallographic plane, i.e. one row attached to each step.

This is, in fact, observed; however, only for scattering geometries which exhibit an increased sensitivity to the step edges, i.e. for scattering under grazing incidence (Fig. 4.5).

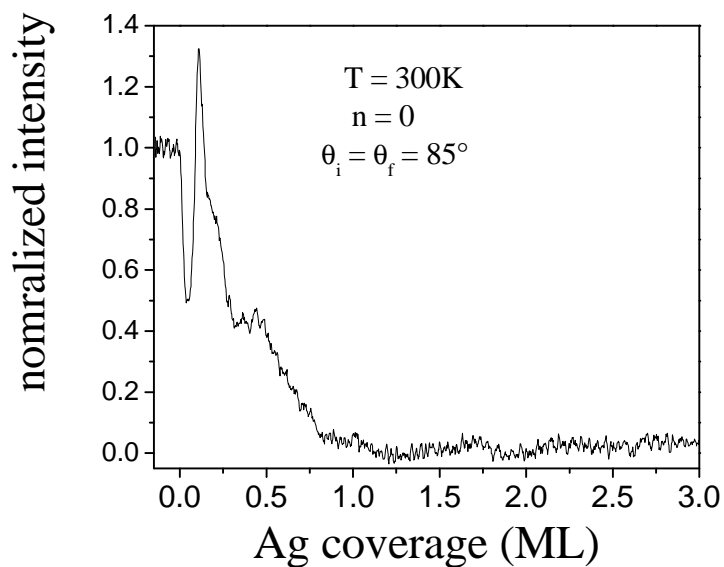


Fig. 4.5: Normalized intensity as function of the Ag coverage on Pt(997) under grazing scattering geometry.

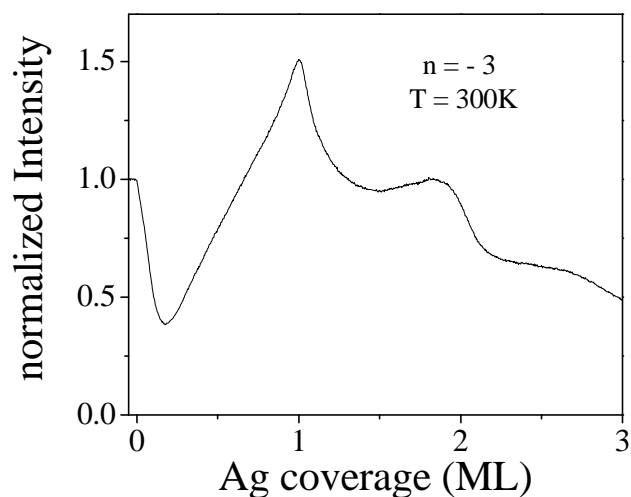


Fig. 4.6: Normalized intensity as a function of Ag coverage on Pt(997) in the $n=-3$ diffraction peak, far from grazing scattering geometry, $q_i = 46.9^\circ$, $q_f = 59.8^\circ$.

The intensity maximum in this measurement is located at a coverage of approximately 13% of a monolayer. This corresponds to the formation of a row along the step edge. In contrast, far from grazing scattering condition (Fig. 4.6) the first reflectivity maximum is observed for the formation of an adlayer covering the terraces completely. As a completely covered surface better corresponds to the intuitive idea of a monolayer we will define the monolayer (ML) coverage for the vicinal surfaces as being the same as for Pt(111) and as it is used in Figs. 4.5 and 4.6. This avoids paradox situations, which may arise when the number of atoms per monolayer reduces with miscut angle (and becomes zero in the limit of the low-index surface). In addition, the oscillations in non-grazing scattering geometry can in general be observed more easily than in grazing geometry as the counting rate is much higher. Thus the calibration of the ML coverage is easier.

The reflectivity maxima under grazing scattering conditions can be interpreted based on results from earlier studies [3, 17, 18, 22]. As far as the observed intensity is concerned an element specific reflectivity and a Debye-Waller factor defined for the steps would have to be considered. These contributions, however, have not been studied in detail yet. The morphological contribution to the reflectivity is easier to access and to interpret. In general, it can be assumed that a first-row-peak with a higher intensity corresponds to a higher perfection of the row formed at the step. This corresponds to a lower minimum of kink density at one instant during its growth. At the microscopic origin of such an increased order is the activation of diffusion processes near the step edge, specifically diffusion around kink corner sites [2, 23] which is the 1-D equivalent to downward diffusion from islands over the Ehrlich-Schwoebel barrier during layer-by-layer growth. In earlier studies a rather broad intensity maximum near half-monolayer coverage was observed for several systems [5, 24]. It was interpreted as the continuing growth of rows with low defect density, so-called row-by-row growth. The oscillations connected with the completion of successive rows are in general strongly damped so that a direct monitoring of continuing formation of rows cannot be obtained. This damping may result from a local inhomogeneity in the adatom flux. It has, however, been shown by calculation [5, 24] that already the known terrace width distribution of a perfectly prepared Pt(997) substrate provides a rapid loss of coherence between the growth phases

of rows on different terraces. Even under optimum deposition conditions the oscillations connected with a row-by-row growth are damped out completely after the second row.

When the growth on a vicinal surface continues it has been found that a new diffraction peak can occur under non-grazing scattering conditions [20, 24, 25]. Its position allows assigning it to reflection of the He beam from (111) oriented terraces with strongly increased width. This situation is called surface faceting, and analysis of the facet diffraction peak allows obtaining additional information on the morphology of the surface. The formation of facets requires a substantial material transport on the surface and the possibility of diffusion over step edges.

To summarize, we can employ non-grazing scattering geometries in order to observe the continuing growth of layers parallel to the terraces and to calibrate the coverage scale. In grazing incidence geometry the quality of the rows formed at the substrate steps can be monitored and indications of the growth mode at the steps can be obtained.

CHAPTER 5

Modification of the Pt step reactivity by Ag deposition

5.1 Introduction

Adsorption from the gas phase plays a fundamental role in heterogeneous catalysis and corrosion. It is a basic process involved in surface reactions to provide the reactants for a chemical reaction at the surface (e.g. in Langmuir-Hinshelwood reaction mechanisms). Dissociative adsorption, moreover, involves a chemical reaction in itself and can thus provide information on qualitative changes of chemical reactivity for modified surface structures even though active sites and dissociation barriers are in general different for different reactions.

Adsorption is a site-specific process, and for many systems point defects and steps play an eminent role due to steric and electronic properties, which are important for the adsorption or dissociation process. It is therefore possible to modify adsorption from the gas phase by comparatively small modifications of the surface chemical composition. The dependence on the local environment is well known for alloy catalysts.

Substrate step decoration is a way to control processes occurring preferentially at steps sites or in their immediate vicinity. To give an example, step decoration has been employed to eliminate the influence of steps on the alignment of adsorbate phases [26]. In this chapter we use the well-characterized step decoration by monatomic Ag rows [17, 24] in order to locally modify the electronic properties at the steps of the vicinal Pt(997) and Pt(779) surfaces without changing the surface morphology. Ag evaporated on vicinal Pt(111) surfaces attaches to the lower step edge and grows in a step-flow mode. At 13% of a ML a monatomic row of Ag forms at the Pt step edges with a low defect density. Fig. 5.1 and 5.2 show two images of the growth of Ag at the step edge taken by Scanning Tunneling Microscopy (STM).

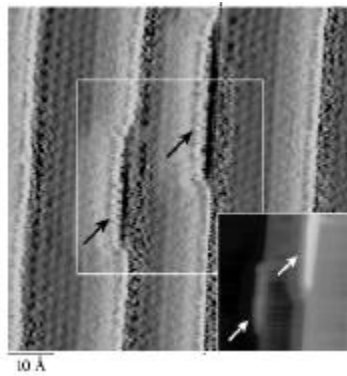


Fig. 5.1: $\partial z/\partial x$ differentiated image of the row formation at 340 K. Step down direction is from right to left, the Pt step edge is marked by a dotted line. (From ref [3])

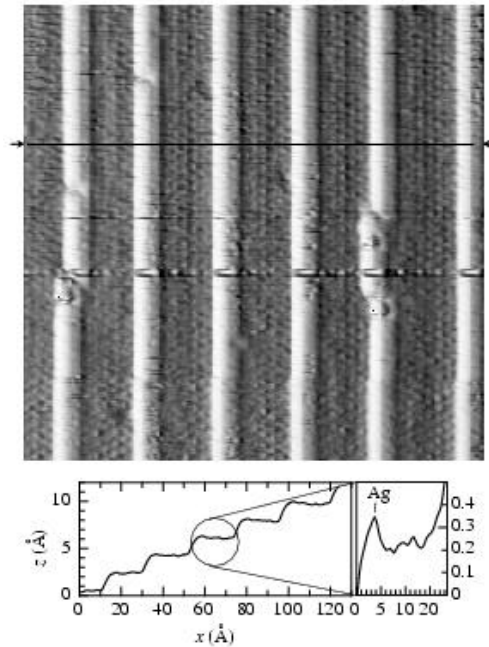


Fig. 5.2: Differentiated image of monoatomic Ag wires at the step edge of Pt (997). The line on the image shows the position of the line scan given below. (From ref [3])

The image in Fig 5.1 was taken after the deposition of 0.03 ML of Ag at 340K in $\partial z/\partial x$ representation to increase the contrast on the terrace. Two Ag islands (indicated by the arrows) are visible at the bottom of two steps edge. At 340 K the Ag atoms can easily migrate to the step edge where they diffuse along the step until they meet another Ag atom and start the growth of a wire. The insert in Fig 5.1 shows the same region imaged in a

constant current representation. Fig 5.2 shows the formation of monoatomic Ag wires after the deposition of 0.13 ML. Their length is only limited by the kink density. The chemical contrast between Ag and Pt, due different electronic densities, is clearly visible. In order to monitor the reactivity of step sites we study the sticking probability of different molecules on the surface. The sticking coefficient (or sticking probability) is defined as the ratio between the number of molecules impinging on a surface and the number becoming trapped [27]. This value can be used to investigate changes in the adsorption process.

Adsorption of molecules on a surface is a problem, which can be fully described only by a multi-dimensional energy surface. Translational, vibrational and rotational coordinates of the impinging molecule and the properties of the surface site, which is hit, enter into a complete model of the adsorption processes. Often simplified models are used which are reduced to only two coordinates, molecular bond length (for diatomic molecules) and distance from the surface. The molecular axis is assumed at a fixed angle with respect to the surface normal and a high symmetry site on the surface is selected [27, and references therein]. In the framework of such a model a two-dimensional energy surface can be calculated in which trajectories for adsorption (or desorption) can be simulated. We will restrict ourselves to basic arguments here, which do not include the complexity of such trajectories. Our discussion will be based on the adsorption energies, adsorption barriers and the existence of precursor states in the adsorption process.

In this chapter we discuss measurements of the adsorption of O₂, H₂, and CO. The adsorption of these gases has been widely studied on closed packed Pt(111) surfaces. As the important role of steps and defects in adsorption was recognized early (see e.g. [28]) the influence of the step density on adsorption on Pt(111) has also been addressed in many studies (e.g. [6, 29-31]).

In the experiments, the adsorption is monitored by TEAS on different diffraction peaks and for different Ag coverages. He scattering was employed to calibrate the Ag coverage, to monitor adsorbate coverage and to deduce the changes in O, H and CO sticking coefficient with Ag coverage. The gases were dosed by backfilling the sample chamber at a pressure between 10⁻⁷ mbar and 10⁻⁶ mbar for O₂ and H₂, and between 10⁻⁸ mbar and

10^{-7} mbar for CO. The measurements were complemented by an STM study in order to obtain local information on adsorption and dissociation sites.

5.2 The reactivity of decorated steps

Fig.5.3 shows TEAS reflectivity measurements during gas exposure for vicinal Pt surfaces. In these measurements we contrast the adsorption on a clean vicinal surface with the adsorption on a surface whose steps were decorated by one row of Ag.

The slope of the curves in the limit of small doses ($\epsilon \rightarrow 0$) is proportional to the initial sticking coefficient of the molecular species [6] and can be taken as a measure of surface reactivity. In the case of O_2 and H_2 the slope of the TEAS curve is drastically changed (by a factor of 10 for O_2 and by a factor of 4 for H_2) by the presence of only 13% of a ML of Ag. In contrast, for CO adsorption there is no change of similar magnitude.

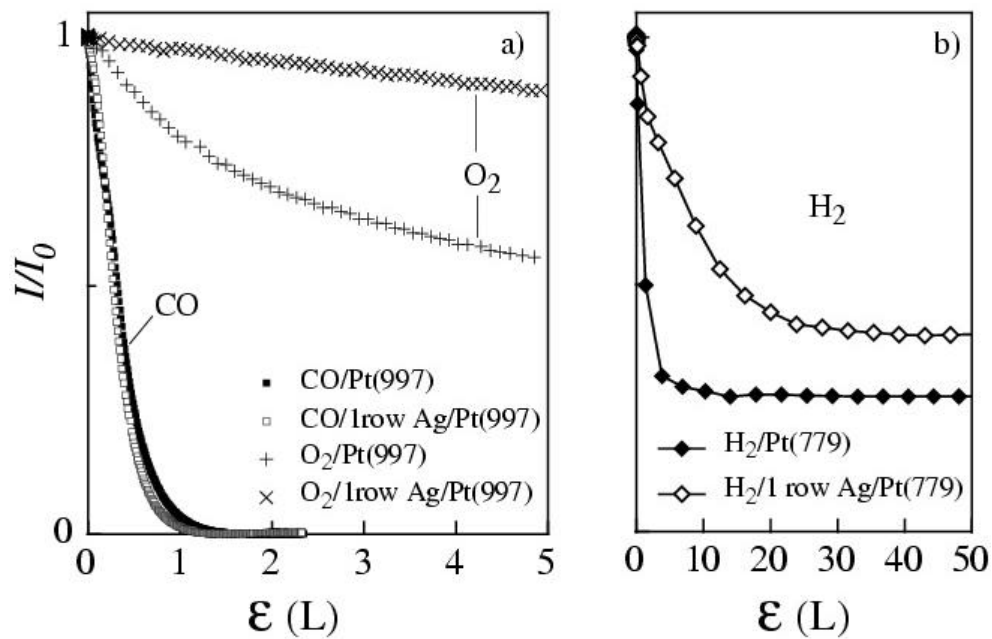


Fig. 5.3 a) TEAS intensity as function of the gas exposure for O_2 at 400K and CO at 340K on clean and on 1 row Ag/Pt(997) in non-grazing geometry, $q_i = 55.6^\circ$; $q_f = 44.2^\circ$. b) Same as a) for H_2 on Pt(779) and on 1 row Ag on Pt(779) at 315 K. $q_i = 56.6^\circ$; $q_f = 42.5^\circ$.

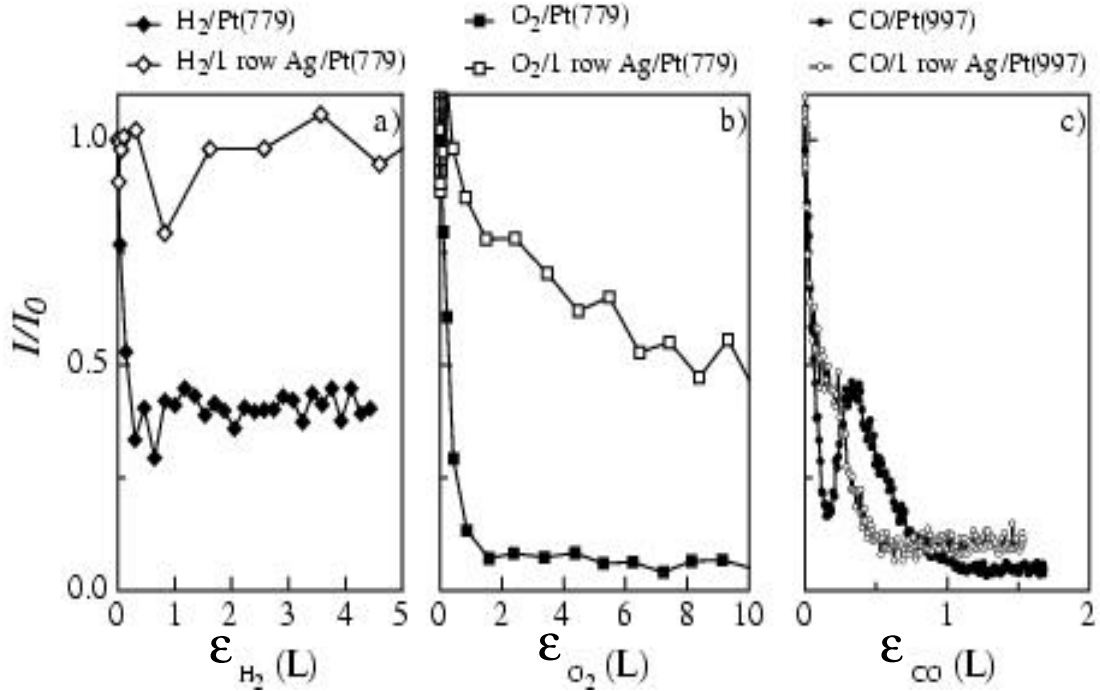


Fig. 5.4: Reflectivity in grazing geometry ($\theta_i = \theta_f = 83^\circ$) as a function of dose for the three indicated gases. (a) H_2 adsorption on Pt(779) at 400K, 10^{-7} mbar gas pressure. (b) O_2 adsorption on Pt(779) at 400K, 10^{-7} mbar. (c) CO adsorption on Pt(997) at 340K, 10^{-8} mbar; the peak for CO/Pt(997) at 0.5L is due to completion of a monomolecular row of CO at the step edge.

Fig.5.4 shows reflectivity curves under grazing incidence, which allow monitoring specifically the adsorption near the steps. There, again, CO adsorption is not strongly changed by Ag decoration. In contrast, the initial slope reduces for O_2 by a factor of 10 and for H_2 by more than 100. This demonstrates that the behavior of all three adsorbates is different. We will discuss the details in the following sections.

The initial slope of the adsorption curve can be described by $I/I_0 = 1 - \Sigma s_0 \epsilon$ where Σ is the adsorbate cross section, s_0 is the sticking coefficient, and ϵ is the gas exposure [6]. When comparing the reduction of He reflectivity for different sample morphology or different adsorption sites it is not evident that the slope can directly be used to determine the sticking coefficient because this requires that the same value for the scattering cross section Σ may be used. It is known that the cross section can vary with incidence angle and He beam energy [6]. One may assume that a minor change in adsorption site alone

will not result in a substantial variation of cross section. Σ can, however, be drastically different for the same adsorbate but different structures of the formed layer [6]. Moreover, the cross section of an adsorbate can vary depending on whether the adsorbate is adsorbed near a defect or on a terrace. In this study it was not possible to determine diffuse cross sections for He scattering for the different adsorbates and Ag coverages. While we think that the substantial changes of initial slope, which we observe cannot be explained by the variation of scattering cross section, we will discuss possible errors for each adsorbate. In the following sections we will find as a general result that due to Ag step-decoration the preferential adsorption site of the adsorbates shifts from a step site towards the terrace. Scattering in non-grazing geometry in a condition close to specular reflection from the (111) terraces exhibits a reduced sensitivity to the step region due to the curvature of the interaction potential in the step region. We can thus expect that the cross section Σ increases rather than decreases when the adsorbate shifts towards the terrace. The observation for both, O and H is that the initial slope of reflectivity and thus the product $\Sigma*s_0$ is reduced if Ag decorates the step. Thus the reduction in sticking coefficient with Ag coverage, which we derive, will rather be underestimated. We can thus assume that the observed tendency for the sticking coefficients for O and H are correct. For the case of O (section 5.3) also the quantitative value has been explicitly verified.

5.3 Adsorption of oxygen

Oxygen can adsorb on a Pt(111) surface as a physisorbed molecule, as a chemisorbed molecule and as chemisorbed atoms. Three chemisorbed molecular states were found for vicinal Pt surfaces [32-36]: An fcc and a bridge bonded terrace species and a bridge bonded step species. Molecules at the step site are stable until 150K [32, 36]. For temperatures above 100 K oxygen adsorbs dissociatively on Pt. Dissociation proceeds via a chemisorbed molecular precursor state [35-39]. Steps on Pt(111) are preferential adsorption sites for both the precursor state and O atoms. The preferential adsorption site of atomic oxygen has been identified by STM images as being the near-edge fcc sites at the upper step edge [40] in agreement with calculations by Slijivananin *et al.* [41].

Fig. 5.5 compares TEAS reflectivity curves in grazing ($n=0$) and non-grazing ($n=-3$) geometry. The result confirms that for both, Pt(997) and Pt(779), step sites are occupied preferentially in agreement with earlier studies [42]. In the measurement no adsorbate reorganization is observed, which Hammer et al. suggested for NO on Pd(211) [43].

For temperatures below 190 K O atoms are immobile on the surface [44]. After O₂ adsorption at 140K the atomic species were found at the same sites as for adsorption at higher temperature [45]. The two atoms emerging from molecular dissociation are found two lattice constants apart. This result clearly demonstrates that O₂ dissociates at the upper step. The most likely path is that dissociation takes place from a bridge position with the O₂ molecule oriented parallel to the step [45]. This process is markedly different from the dissociation of N₂ on Ru(0001), where the atoms dissociate on the step facet with the two atoms moving towards different terraces [46].

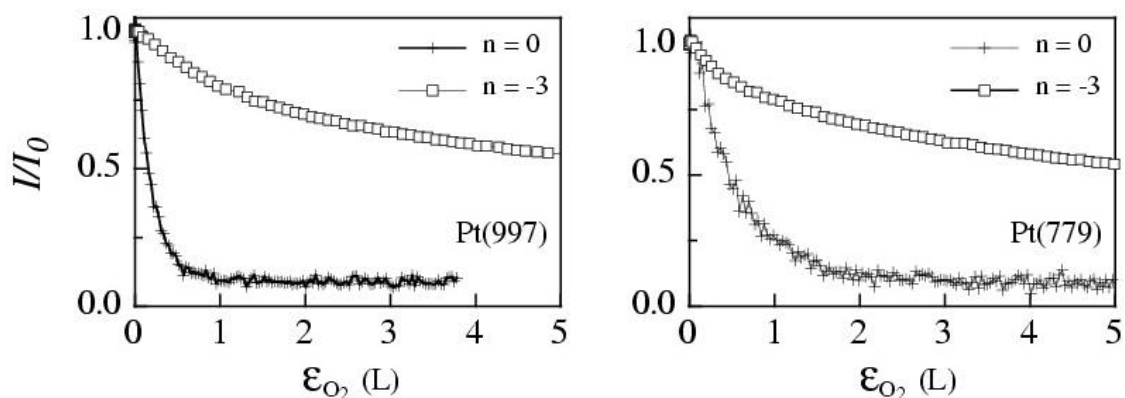


Fig. 5.5: TEAS intensity during dosing of O₂ on Pt(997) (left) and Pt(779) (right) at 400K. The decrease in intensity of the $n = 0$ curve ($\mathbf{q}_i = \mathbf{q}_f = 83^\circ$) is due to O adsorption at the step edges whereas the decrease in intensity of the $n = -3$ curve ($\mathbf{q}_i = 55.6^\circ$, $\mathbf{q}_f = 44.2^\circ$) is mainly due to the coverage of terraces by O and is only weakly dependent on the step edges coverage.

Fig. 5.6 shows the He reflectivity in non-grazing scattering geometry as a function of O₂ dose measured for pre-adsorption of the indicated Ag coverages. For both, Pt(997), and Pt(779) the sticking probability reduces continuously with increasing Ag coverage. The evaluation of the data for the initial sticking probability is represented in Fig. 5.5. To calculate the relative variation in dissociation rate we take the value $d(I/I_0)/de|_{e=0}$ for each curve and divide it by the value obtained for the clean surface. For Ag coverages between 0 rows and 1 row we find a rapid decrease by a factor of 10. This absolute ratio between adsorption on the clean step edge and on a Ag decorated step edge was verified by evaluating the coverage observed in STM images for equal gas doses; in this way the change by one order of magnitude was confirmed independent from the He reflectivity measurements.

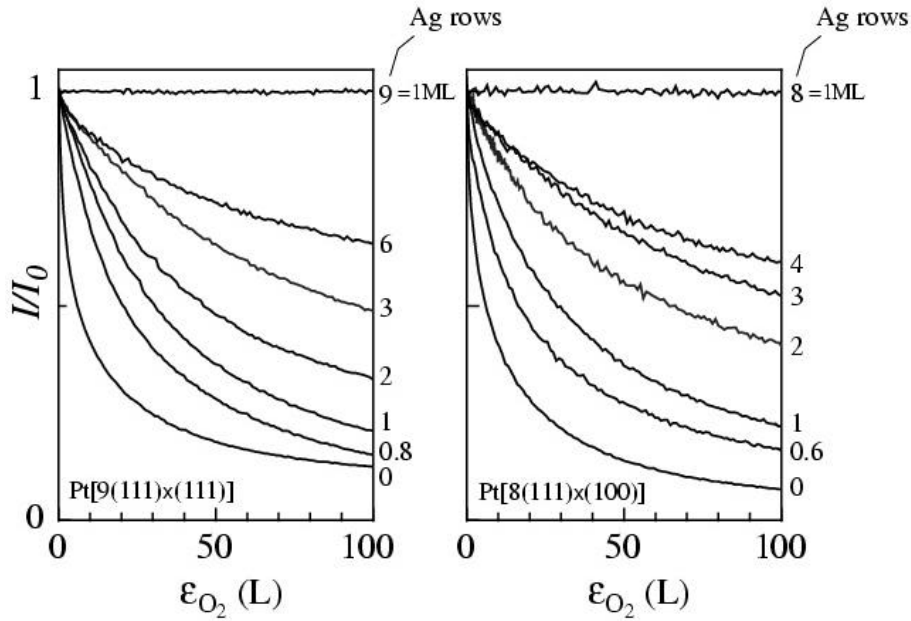


Fig. 5.6: TEAS intensity as a function of O₂ exposure for different Ag coverages. The Ag coverage in units of monatomic rows is indicated on the right of the figures. The beam energy is 22 meV. Left: $q_i = 55.6^\circ$; $q_f = 44.2^\circ$ for Pt(997); right: $q_i = 56.6^\circ$; $q_f = 42.5^\circ$ for Pt(779).

Due to the mobility of Ag atoms at the Pt step edge, Ag atoms form 1-dimensional chains at the step edges. In consistency with this observation, the dissociation rate is proportional to $(1-\Theta_{\text{Ag}})$, as shown in Fig.5.7, and not to $(1-\Theta_{\text{Ag}})^2$ as it would be the case for a random distribution of single Ag atoms attaching at the steps. The decrease between the completion of the first row and the monolayer can be explained by assuming that O_2 molecules impinging on the Ag layer are efficiently reflected back into the gas phase [47]. Approaching Ag monolayer coverage the initial sticking coefficient drops abruptly by several orders of magnitude.

STM images of a Pt(997) surface after decoration by one row of Ag followed by exposure to 19 L O_2 at 350K show that O adsorbs on the same site as on the clean Pt(997) surface. This is in agreement with density function theory (DFT) calculations for both, Pt(221) and Ag/Pt(221) [41].

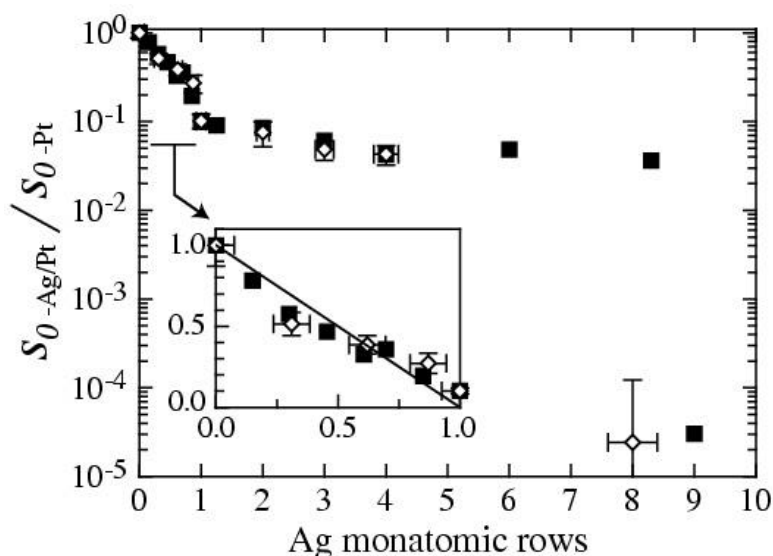


Fig. 5.7: Variation of the sticking coefficient of O_2 compared to the clean surface. Full square and open diamonds represent results for Pt(997) and Pt(779), respectively. The solid line in the inset represents the behavior following a $(1-\Theta_{\text{Ag}})$ function (see text).

Due to the different processes involved in O adsorption, the origin of the reduced sticking probability cannot be derived directly from these results. The theoretical study [41] finds that the O₂ dissociation barrier at the upper step edge is reduced due to the presence of the Ag row. This would mean that Ag decoration increases the dissociation rate, which would be in contrast to the observed behavior. In addition, the calculations provided the result that the binding energy of the precursor state at the upper step is reduced from 0.8 eV to 0.3 eV [41]. Such a substantial reduction results in a reduced occupation of the precursor state, which must be occupied in order to enable dissociative adsorption. It is therefore a plausible reason for the reduced sticking probability. In other words one can say that the partitioning between dissociation and desorption from the precursor state is shifted by Ag decoration towards desorption.

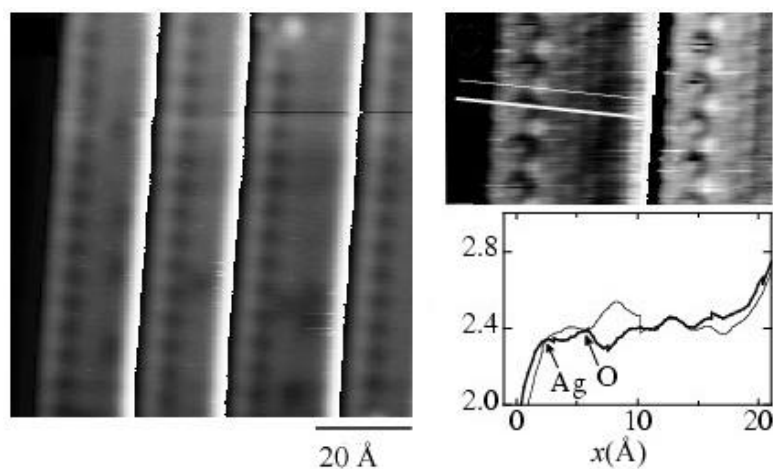


Fig. 5.8: a) STM picture taken after the deposition of one row of silver followed by dosing 19 L of O₂ at 350K. b) Detail of the steps with O adsorbed on top of the step a few Å away from the step edge. c) Height profiles (line scans) along the white lines indicated in image b).

It is often assumed that the occupation of chemically reactive step sites results in an effective reactivity that is close to the reactivity of the defect-free surface [48]. In the

following we will demonstrate, that this assumption is at least not valid in the case of oxygen on a vicinal Pt(779) surface.

O forms a $p(2 \times 2)$ superstructure on Pt(111) terraces. This superstructure gives rise to additional peaks in the TEAS diffraction pattern from the Pt(779) surface as shown in Fig 5.9. The intensity of such a diffraction peak is a measure for the area over which the superstructure has formed. Fig.5.8 shows an adsorption measurement on such a peak. For O-Ag pre-decorated steps the saturation of peak intensity is reached after much higher dose than for a surface prepared with O-saturated steps. This indicates a slower filling of the terrace sites. Modification of the step reactivity thus affects the overall adsorption rate even after "poisoning" the reactive site.

There are two possible reasons for this behavior: First, O atoms dissociating at the steps may migrate to the terrace leaving free step sites. Second, the occupied dissociation sites may remain active for the dissociation. Concerning the first argument, one can estimate that for a realistic adsorption energy difference between step and terrace sites (> 0.25 eV), the concentration of unoccupied step sites remains negligible at 400K. The second explanation appears to be more likely, especially in the light of the results of T. Zambelli *et al* [48] who observed an increased O_2 dissociation in the vicinity of chemisorbed O atoms on the Pt(111) surface.

A further confirmation of the persistent reactivity of occupied dissociation sites is given by comparison of the intensity of a diffraction peak of the oxygen induced $p(2 \times 2)$ reconstruction on the Pt(779) and Pt(111) surfaces as a function of gas dose. Saturation is reached after $\sim 800L$ for a Pt(111) surface, a dose approximately a factor of 8 larger than it is necessary to obtain saturation on the clean vicinal surface. If the O-saturated steps would not participate in the dissociation process we would expect that the O_2 dose required to saturate the O $p(2 \times 2)$ superstructure in these two cases would differ by only 2L, which is the dose necessary to saturate all step sites.

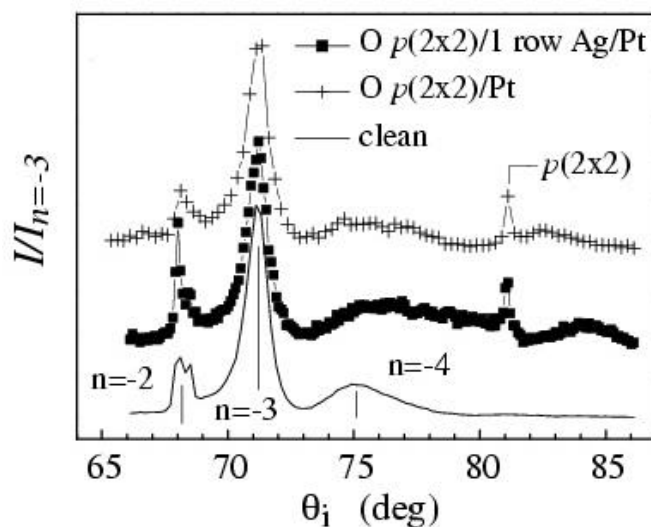


Fig. 5.9: TEAS diffraction pattern for clean Pt(779) surface and for the same surface after saturation with O with and without a row of silver deposited at the step edges. The total scattering angle is $\chi = 123.5^\circ$ and $\lambda_{\text{He}} = 0.98 \text{ \AA}$.

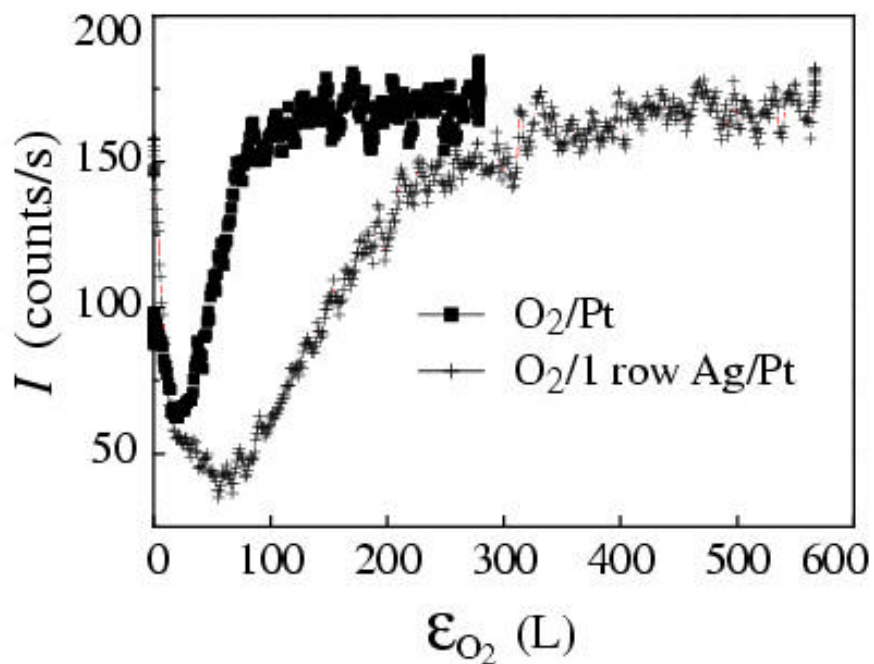


Fig. 5.10: Evolution of the diffraction peak monitoring the $p(2 \times 2)$ reconstruction on a clean Pt(779) surface and for a surface with one row of Ag. $T = 400\text{K}$, $q_i = 81.1^\circ$, $\chi = 123.5^\circ$, and $\lambda_{\text{He}} = 0.98 \text{ \AA}$.

5.4 Adsorption of carbon monoxide

From a simplified perspective, the sticking probability of CO depends on the energy in the external and internal degrees of freedom and the orientation of the molecule. The molecule does neither have to overcome a substantial energy barrier during absorption nor pass through a precursor state, which may increase the probability of desorption back into the gas phase before adsorption occurs. One might expect that in such a case the sticking probability may depend on orientation and internal degrees of freedom of the incoming adsorbate but not on the adsorption potential as long as it remains low enough.

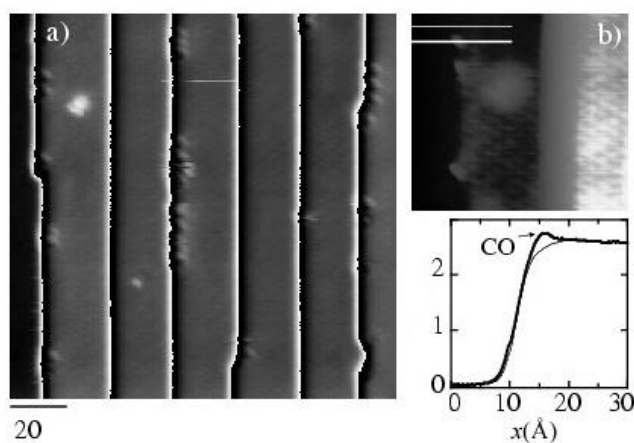


Fig. 5.11: (a) CO molecules (white dots) adsorbed at the step edges of Pt(997) step-down direction is from right to left. (b) Detail showing CO occupying the edge on top (top left), the terrace (center) and the kink on top position (bottom left). The graph below shows two height profiles, one passing over a CO molecule the other over a Pt edge atom.

The preferential adsorption site of CO on Pt(997) is the upper step in an on-top position with its axis essentially parallel to the surface normal [49]. The theoretical result is in good agreement with experiment. Fig.5.11 demonstrates that on-top adsorption is not only observed at the upper step edge but also on the terraces and at kink positions. Interestingly enough, STM data show that after decoration of the Pt step with one row of Ag the adsorption site remains essentially the same (Fig.5.12b). Due to the decoration the Pt atom to which the CO molecule is bound has obtained additional neighbors. A higher coordination of the Pt atom results, however, in a reduced binding energy for CO [49]. This can also be expected in this case. The observation that for partially Ag covered steps CO is preferentially found in the step regions not decorated by Ag (Fig. 5.12c) confirms this conclusion. We observe that this change of adsorption energy has no significant effect on the observed sticking coefficient as demonstrated in Figs. 5.3 and 5.4. Due to the uncertainty to determine the change in He scattering cross section the sticking coefficient may, in fact, be somewhat reduced in the case of Ag decorated steps.

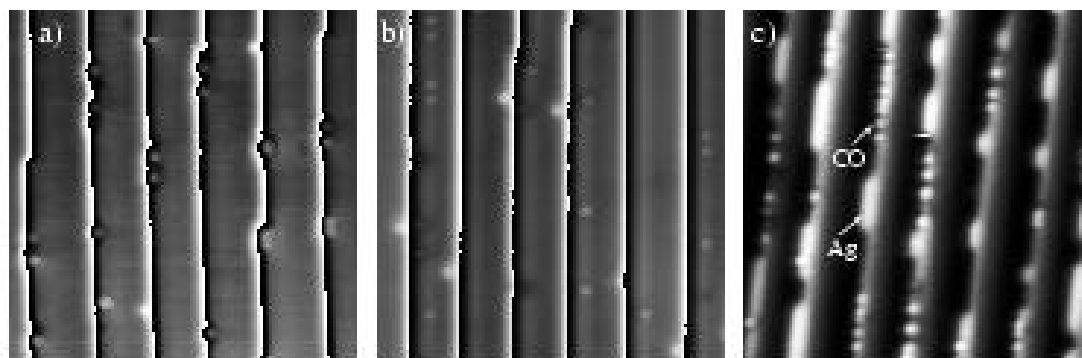


Fig. 5.12: (a) CO molecules (white spots) adsorbed on top of Pt(997) step edges (step down direction is from right to left). (b) Adsorption after complete step decoration with a monatomic Ag row. (c) Adsorption for partial step decoration: The molecules bind preferentially to Ag free step regions.

5.5 Adsorption of hydrogen

H adsorption on Pt(111) has been studied intensively and several studies discuss the adsorption on vicinal Pt(111) surfaces [50, 51]. For incident thermal energy H_2 the steps play an essential role for adsorption [6, 30]. For our experimental conditions H adsorbs on Pt(997) by direct adsorption. A precursor-mediated process was observed only for low incidence energies [30] or for low surface temperature [6]. Moreover, hydrogen can adsorb on Pt(111) without energy barrier [52]. This may suggest that – apart from geometrical and orientational effects – the dissociative adsorption of H_2 should resemble CO adsorption rather than O_2 adsorption. This assumption appears to be in contradiction to the result presented in Fig.5.3. The reason for the discrepancy is a change of adsorption site and probably also of dissociation sites. The actual step adsorption site of H on vicinal Pt(111) surfaces is still debated. For A steps (as present on Pt(779)) an adsorption on the step facet is assumed [53]. A study using the cluster based extended Hückel molecular orbital (EHMO) method, however, suggest that an adsorption site on top of the step atoms is favored for both A and B steps (as on Pt(997)) [54]. An EELS study by Baró and Ibach [50] provides evidence from vibrational spectroscopy that H at the B step is adsorbed in bridge position. The model proposed by the authors suggests an adsorption site on the step facet although the bridge site at the upper step edge is not excluded. If the adsorption site were on the step facet this would mean that the preferential H adsorption site would actually be blocked by the Ag row. Fig.5.4 demonstrates that after Ag decoration H adsorbs not even close to the step edge. In this scattering geometry adsorption a few Ångstroms away from the step edge can be monitored. Moreover, adsorption both at the bottom (observed e.g. for Ag and other metals) as well as at the top of the step (observed e.g. for O_2 and CO) can be detected. Thus, the decoration of Pt steps by a complete Ag row makes terrace sites to preferential adsorption sites.

With respect to the He scattering cross section of H adsorbed on different sites the same argument as for O holds. As the exact adsorption sites are not known for H, the reduction of sticking coefficient by a factor of four may not be regarded as a quantitative result. The tendency, however, appears correct as it is unlikely that hydrogen can occupy sites which have a four times smaller cross section than step edge sites.

5.6 Conclusion

Steps play a major role in the adsorption of O, CO, and H on Pt(111). In all three cases preferential step decoration is known to occur. We employ the decoration of the regularly stepped Pt(997) and Pt(779) surfaces by monatomic Ag rows in order to selectively modify the electronic structure at the step edge and thus the adsorption properties.

O adsorption exhibits preferential adsorption and dissociation near the upper Pt step edge. Adding a Ag row at the substrate step does not significantly displace these positions. The sticking probability is reduced by a factor of 10 upon Ag step decoration. Based on theoretical studies it is found that the dissociative adsorption of O₂ is reduced upon Ag step decoration due to a reduction of binding energy of the molecular precursor state at the upper step. This energy reduction is more efficient than the reduction of the dissociation barrier due to the Ag row at the step, which would lead to the opposite trend in sticking probability. Monitoring the formation of the oxygen 2x2 superstructure on the (111) terraces during O₂ dosing indicates that even blocked dissociation sites at the step can still lead to an enhanced dissociative adsorption with respect to a flat surface.

For CO adsorption we find that the preferential binding site remains on the Pt upper step edge after Ag adsorption. We find that the binding energy at the decorated step regions is, however, significantly reduced. This can be explained by the higher coordination of the Pt atoms to which CO binds. Although the binding energy changes for step decoration by Ag no significant change in sticking coefficient is observed.

For H, finally, the preferential adsorption site at the step edge is possibly blocked by the Ag row decorating the step. It cannot be excluded that the same applies for the site on which H₂ adsorption from the gas phase takes place preferentially. This may, in fact, explain the observed reduction of sticking probability. The measurements demonstrate that the new preferential adsorption site must be situated rather far away from the step edge.

CHAPTER 6

Fe growth on Pt (997)

6.1 Introduction

The growth of nanometer structures of ferromagnetic materials on non-magnetic substrates is attracting much attention. This is due to the search for techniques, which will allow continuing the size-reduction of mass storage media in future devices. A basic question is how ferromagnetic nanometer structures can be created and what their respective Curie temperature is. A recent study succeeded in showing that Co nanowires with single atom width exhibits magnetic hysteresis below 15K [1]. It is of interest to study the properties of various nanostructures of other, similar elements. In this chapter we study the growth of Fe on Pt(997) with respect to morphology, structure and alloy formation. The results are applicable to a controlled preparation of specific structures for studies of their magnetic properties.

While numerous studies on magnetic properties were made for thick Fe layers on Pt, FePt bulk alloys [55-58], and iron oxides on Pt(111) [59-62] so far only few studies covered the range of ultra thin Fe films on Pt(111) [63-65]. No study was yet carried out for a vicinal Pt(111) surface.

It has been shown [66, 67] that sputter-deposited or evaporated Fe layers on Pt substrate form strained γ -Fe of face-centered-cubic (fcc) lattices up to 4~5 mono layers (ML), and α -Fe of body-centered-cubic (bcc) for higher coverages. In a recent STM and LEED study [62], it was found that Fe evaporated on Pt (111) showed three-dimensional growth at room temperature.

Similarly to Co or Ni, Fe is an element for which the competition between epitaxial growth and bulk diffusion play an important role on Pt(111) or Pt(997) [18, 45]. In addition, Fe exhibits a strong tendency to form ordered alloys in the bulk as well as on the surface. The basic tendency for alloying is already obvious from the Pt-Fe bulk phase diagram [68] and results based on the effective medium theory (EMT) [69]. The strong Pt surface-segregation observed for the (111) surface of a Pt₈₀Fe₂₀ crystal [70, 71] appears to occur only to a much smaller degree for Fe layers on Pt(111) [65].

In this chapter we present a study of the growth of Fe on Pt(997) at temperatures between 175K and 800K. Growth and alloying are studied for coverages ranging from sub monolayers to a few multilayers. The measurements are performed with TEAS and Auger spectroscopy.

6.2 Experimental

The Pt(997) surface was prepared with the usual procedure (see chapter 4). The cleanliness of the surface was checked with AES and diffraction scans of the surface.

The base pressure in the chamber was 2×10^{-10} mbar. Iron was evaporated from a 2mm diameter iron rod with a purity of 99.99%, heated by electron bombardment. During the evaporation the pressure in the chamber rose to 3×10^{-10} mbar. The Fe flux from the evaporator was calibrated by identifying monolayer (ML) completion with the first reflectivity maximum on the $n = -3$ diffraction peak at 300K substrate temperature. The flux was typically 2×10^{-3} ML/s.

6.3 Results

6.3.1 Row formation

Figure 6.1 shows deposition experiments with sample temperatures between 175K and 800K monitored by He scattering at grazing scattering geometry on the $n = 0$ diffraction peak. Between 175K and 600K a reflectivity maximum can be observed for a Fe coverage of 0.125 ML.

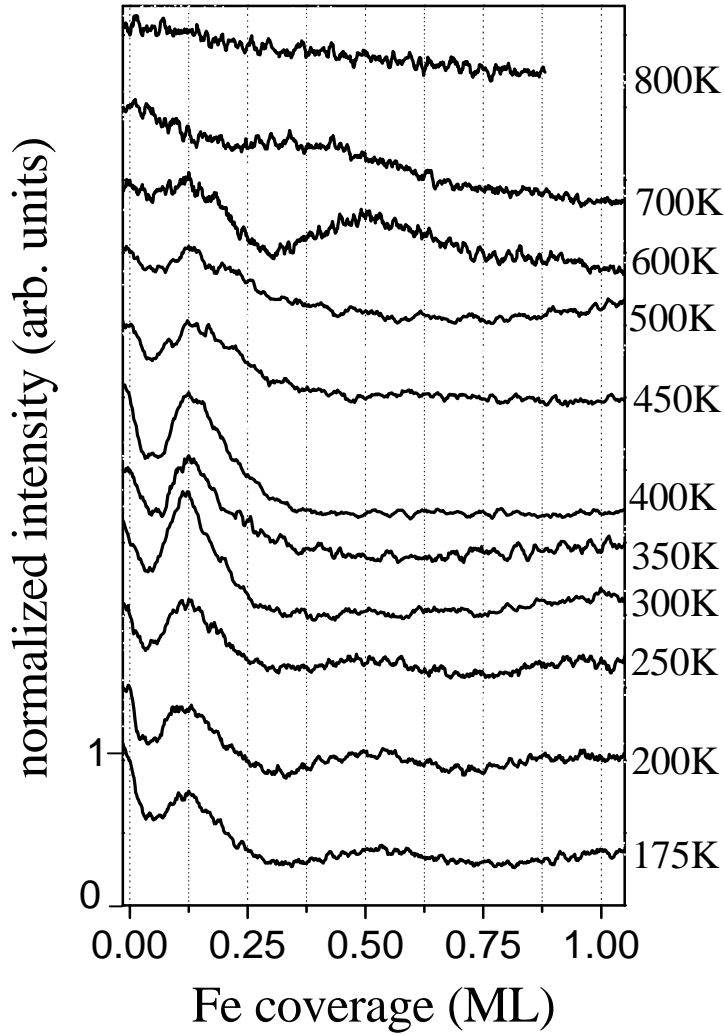


Fig. 6.1: Fe deposition monitored at grazing scattering geometry for the indicated temperatures. Flux: 2×10^{-3} ML/s, $q_i = q_f = 85.0^\circ$, $\lambda = 1.01 \text{ \AA}$. The curves have been normalized to the intensity at the beginning of the deposition; they have been offset vertically by multiples of 0.5 units.

This maximum corresponds to the formation of a complete row at the step edge. Between 175K and 250 K and also at 600K a second peak at a coverage of 0.5 ML is observed. As

discussed in chapter 4 this peak may indicate a continuing row-by-row growth, which preserves a step edge morphology with low defect density during the growth. From the maximum intensity of the first row peak one can conclude that the lowest defect density at the Fe decorated step is found around 300K.

6.3.2 Layer formation

Figure 6.2 shows deposition experiments between 200K and 700K monitored on the $n = -3$ diffraction peak (non-grazing incidence). For temperatures $T = 450$ K a reflectivity maximum is found at monolayer coverage. For temperatures $T < 300$ K and at 500K a change of slope is seen at about 0.13 monolayers, which indicates the formation of a monatomic row even under non-grazing geometry. Between 300K and 500K this change of slope is not observed even though we established in the last section that perfect row formation is still present.

A second maximum near the 2ML coverage is observed only between 300K and 400K. It is lower in intensity than the 1ML maximum. This indicates the formation of a second layer with a reduced reflectivity, probably with a rough surface morphology. Maxima for the completion of further monolayers were not observed, except under conditions when the residual gas pressure was unusually high (probably a surfactant induced behavior which was not studied in detail).

For temperatures >450 K the shape of the reflectivity curves change qualitatively. At 500K the intensity decreases only during the formation of the first row and then stays almost constant up to half monolayer coverage. For 500K and 550K a minimum is found at monolayer coverage. For 600K the curve increases slightly until row completion and then decreases continuously. At 700K, finally, a continuous decrease is observed which is overlaid with a shoulder at monolayer completion.

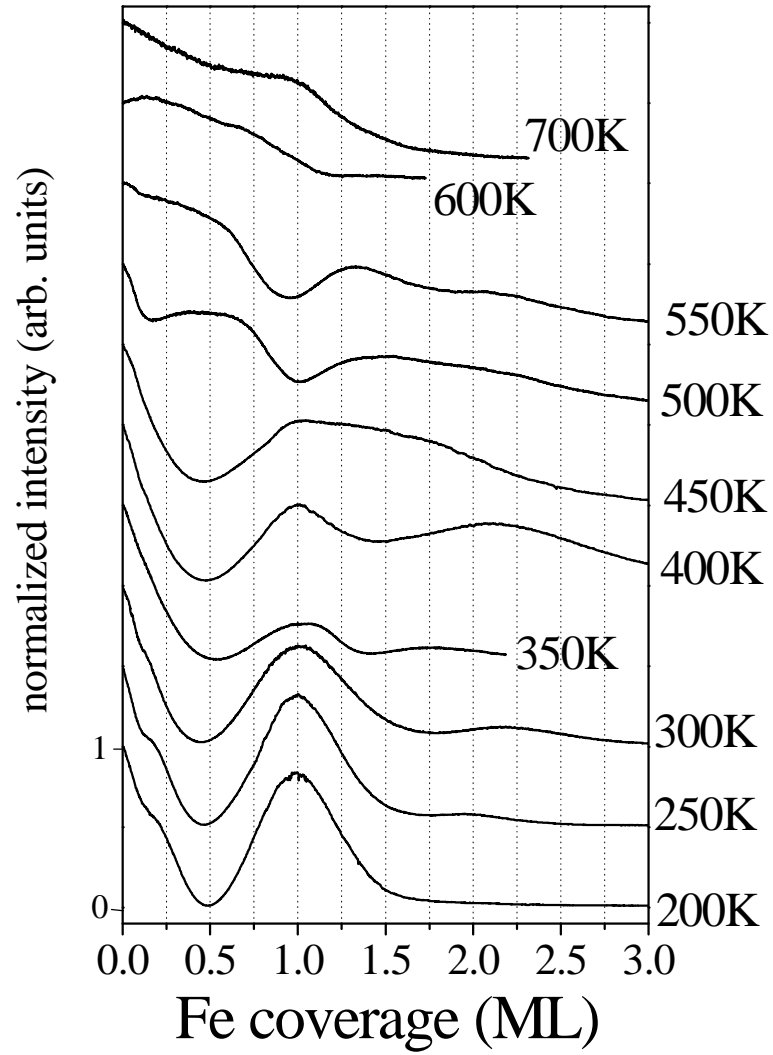


Fig. 6.2: Fe deposition monitored on the $n = -3$ peak for different temperatures. Flux = 2×10^{-3} ML/s, $q_i = 57.8^\circ$, $\chi = 101.8^\circ$, $\lambda = 1.01 \text{ \AA}$. The curves are normalized to the intensity at the beginning of the deposition. They are offset vertically by multiples of 0.5 units.

6.3.3 Growth below 450K

Fig. 6.2 demonstrates that below 450K a smooth Fe monolayer can be grown on Pt(997). It was not possible to decide from He diffraction scans whether this monolayer grows pseudomorphically or with nearest neighbor distances close to the iron bulk value; α -Fe exhibits a bcc lattice with lattice constant $a=2.866\text{\AA}$ resulting in a nearest neighbor distance of 2.48\AA i.e. 11% compressed with respect to Pt.

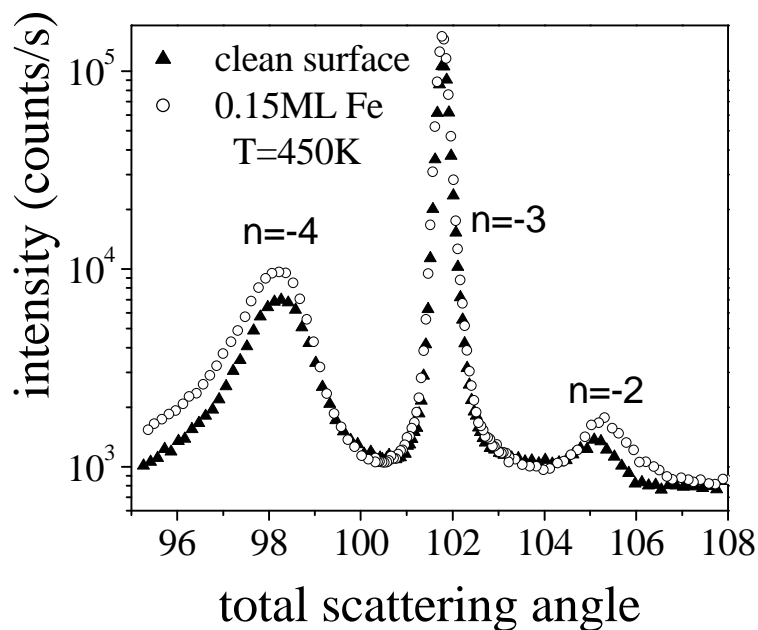


Fig. 6.3: Diffraction pattern for Pt(997) after deposition of 0.15 ML of Fe and heating at 450K compared to the pattern of the clean surface, $q_i = 57.8^\circ$, $f_i = 51.4^\circ$, $\lambda = 1.01 \text{\AA}$.

In order to obtain more information on the morphology of the deposited layers we made diffraction scans for different iron coverages and compared them with the corresponding scan of a clean surface. For 0.15 ML of Fe deposited at 350K then heated to 450K the

only noticeable difference is a slight decrease in intensity (Fig.6.3). The result is not surprising since the growth begins with the formation of a row at the steps, which represents a stable morphology even at elevated temperatures. In addition, the step region does not contribute substantially to the reflected intensity in this scattering geometry. For 0.8 ML Fe deposited at 350 K the intensity of the $n=-3$ peak has decreased by 65% (Fig.6.4). As in the preceding case we do not see evidence for a change in surface structure with respect to the clean surface. We conclude that for temperatures around 400K the growth of the Fe adlayer is preserving the Pt(997) morphology for coverages below a monolayer.

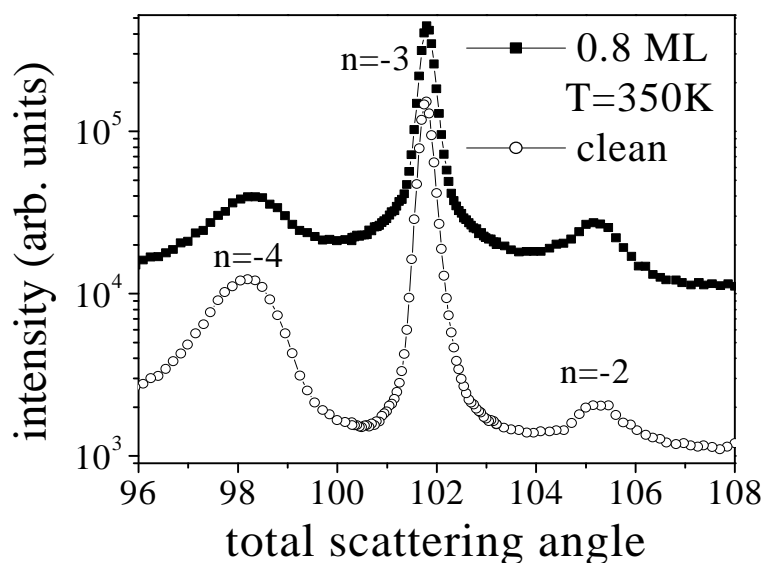


Fig. 6.4: Diffraction pattern for Pt(997) after deposition of 0.8ML of Fe at 350K compared to the pattern of the clean surface, $q_i = 57.8^\circ$, $f_i = 51.4^\circ$, $\lambda = 1.01 \text{ \AA}$. The curve corresponding to a coverage of 0.8 ML has been offset to higher intensities by a factor of 10.

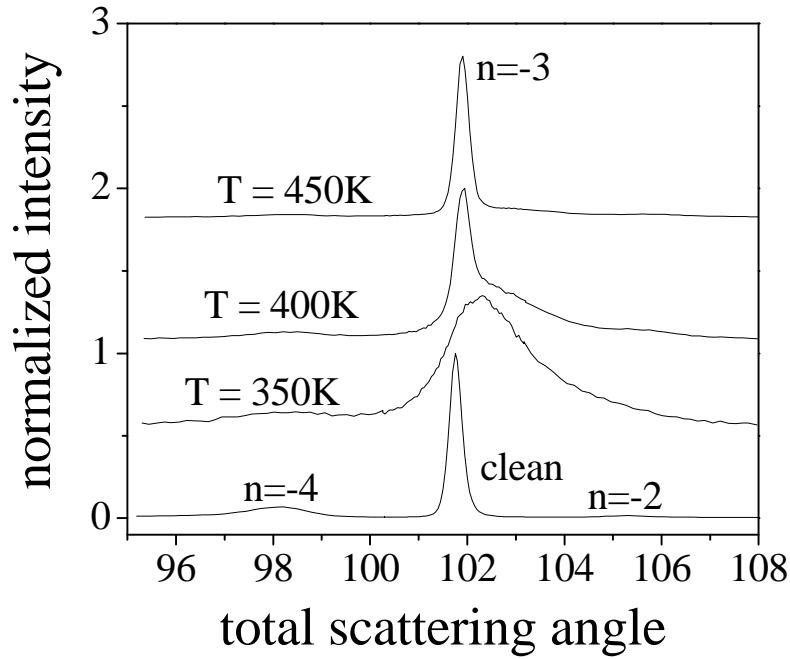


Figure 6.5: Diffraction pattern of Pt(997) after deposition of 1.5 ML at 350K and heating to the indicated temperatures; comparison to the pattern of the clean surface, $q_i = 57.8^\circ$, $f_i = 51.4^\circ$, $\lambda = 1.01 \text{ \AA}$. The curves were normalized to the peak maximum and offset vertically for clarity.

In a next step we deposited 1.5 ML of Fe at 350K then heated the sample to 400K, then to 450K. Fig.6.5 shows that substantial changes occur for this experiment. By fitting the diffraction pattern with four Gaussian peaks

$$I = I_0 + \sum_{i=1}^4 I_i \exp\left(-\frac{1}{2} \left(\frac{x - x_i}{w_i}\right)^2\right) \quad (6.1)$$

we find that in addition to the weak Pt(997) diffraction peaks we observe an additional, broad peak at a total scattering angle of 102.8° . This peak indicates the presence of (111) facets (see also chapter 4).

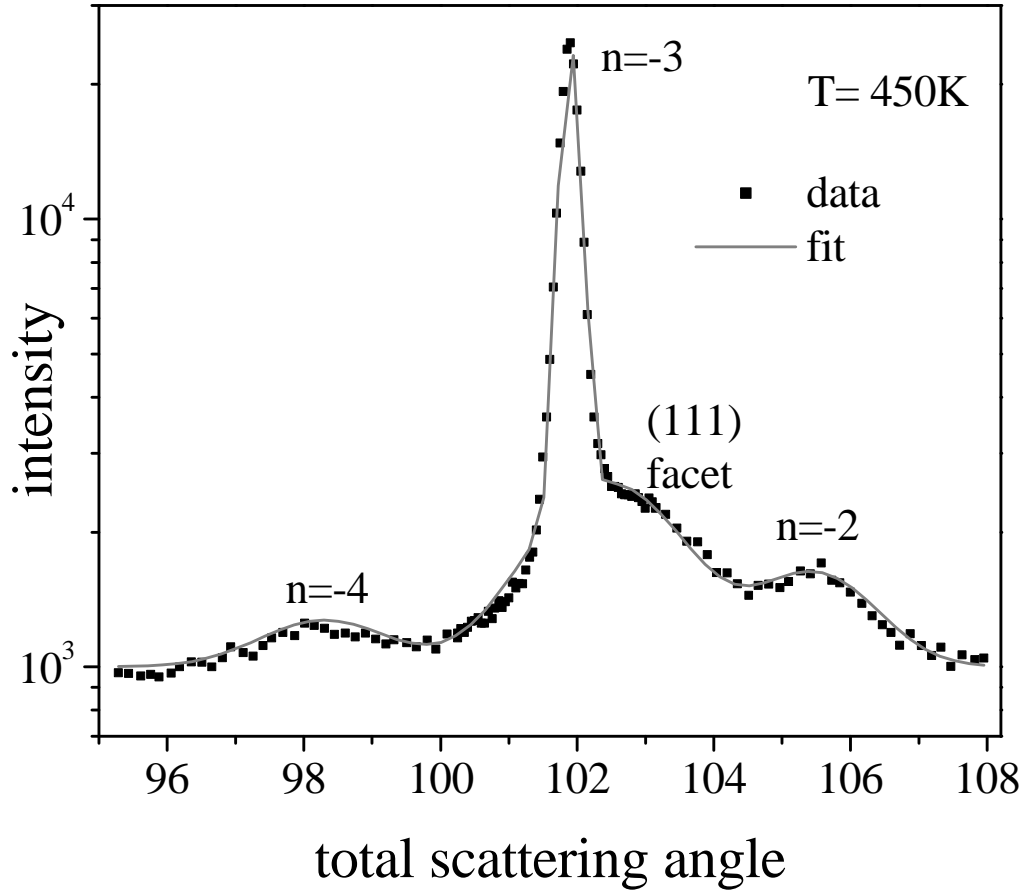


Figure 6.6: Example of a fitted diffraction pattern: Measurement after deposition of 1.5 ML at 350K and heating to 450K, $q_i = 57.8^\circ$, $f_i = 51.4^\circ$, $\lambda = 1.01 \text{ \AA}$. The thin line is the fit by the function given by eq. (6.1).

The results of the evaluation of the facet peak and the $n=-3$ diffraction peak for the scans at temperatures between 350K and 600K are given in table 1. The relative peak intensity is obtained as a product of peak width and peak height. The background intensity I_0 in eq. (6.1) was around 950 counts/s and did not vary significantly with temperature.

T (K)	facet peak			n = -3 peak		
	width (degrees)	height (counts/s)	relative intensity	width (degrees)	height (counts/s)	relative intensity
350	1.04	2115	1	0.44	993	1
400	1.1	1502	0.75	0.18	7287	2.9
450	1.2	1606	0.88	0.14	22175	6.8
500	1.65	1100	0.82	0.14	22658	7.2
550	2.03	750	0.69	0.14	21029	6.5
600	2.6	717	0.84	0.14	30431	9.4

Table 6.1: Evolution of the facet peak and the n=-3 diffraction peak from the Pt(997) step array for a positive temperature ramp.

Whereas for increasing temperature the Pt(997) diffraction peaks increase in intensity and become narrower, the facet peak increases in width (Fig. 6.7). At 350 K the facet peak has a width of about 1.1° , which corresponds to facets of an average size of about 80 \AA . At 600K the average facet size has decreased to 28 \AA , which corresponds almost to the regular terrace size on Pt(997). A plot of the intensity of the facet peak as a function of temperature is shown in Fig. 6.8. No correction for the Debye-Waller factor is taken into account. On an absolute scale the intensity reduces only slightly. With respect to the full spectrum, however, it becomes negligible already above 500 K. The behavior of the n=-3 diffraction peak indicates a reduction of roughness with increasing temperature. This decrease is most pronounced around 400K indicating that at this temperature adatom diffusion in the second Fe layer sets in and smoothens the surface morphology. This observation is in agreement with the observation (Fig.6.2) that at 400K the most pronounced maximum for the completion of the second monolayer is observed.

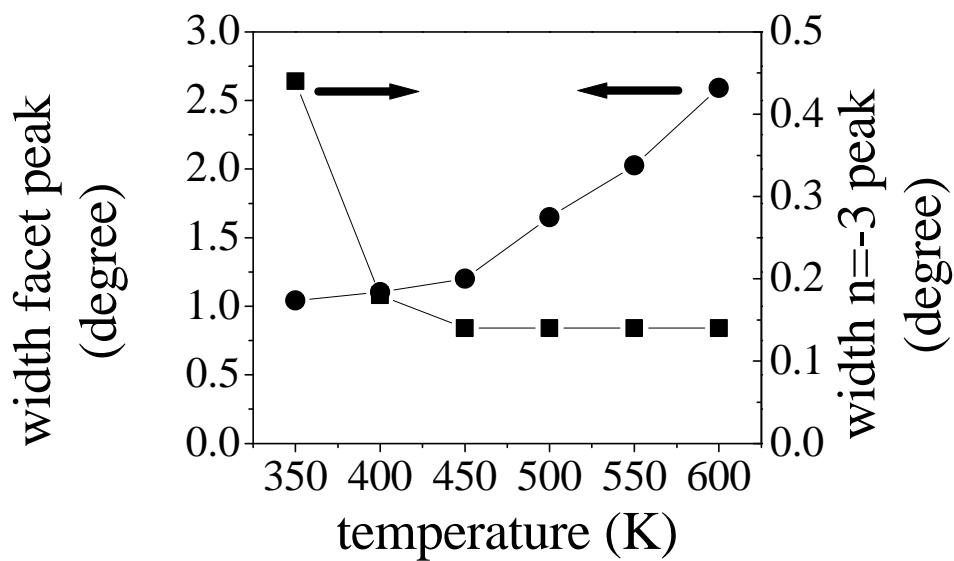


Figure 6.7: Width of the facet and $n=3$ peaks as function of the temperature.

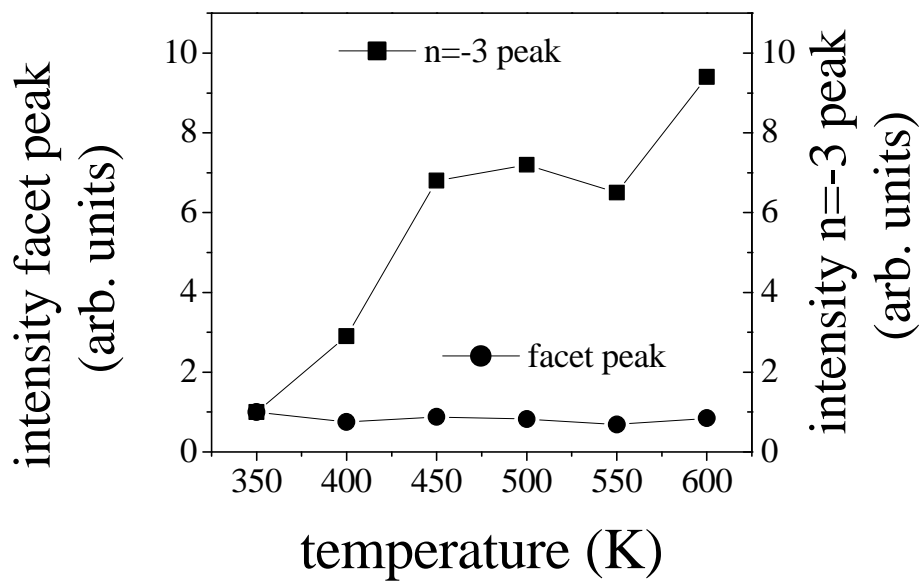


Figure 6.8: Intensity of the facet and $n=3$ peaks as function of temperature.

6.3.3 Alloying

The He reflectivity curves during Fe deposition change qualitatively at a substrate temperature of 500K. As this change can be due to the onset of alloying, we investigated this region in more detail. Fig.6.9 shows the behavior of the relative Fe concentration obtained from Auger spectra during a temperature ramp. The measurement started with the deposition of 1ML of Fe at 200K. Then the temperature was increased in steps of 50K and one Auger electron spectrum run at each point. The time between two spectra was 15 minutes. For the representation in Fig.6.9 the 64 eV peak of Pt and the 651 eV peak of Fe were evaluated. The plot shows that Fe atoms diffuse into the bulk only at temperatures above 600K which is in agreement with earlier studies [64]. Bulk diffusion of Fe thus plays a role for the adsorption curves at 600K and above. It does, however, not explain the shape of the curves at 500K-550K (Fig.6.2).

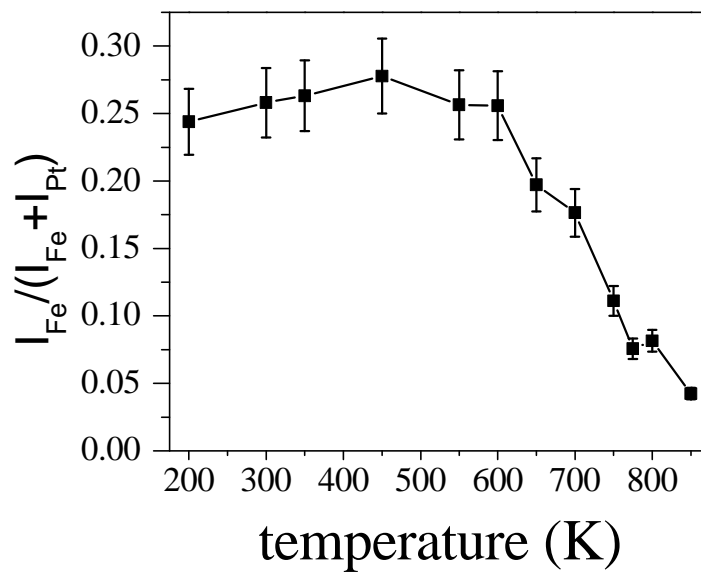


Fig. 6.9: Relative Auger intensity of a monolayer of Fe deposited at 200K, then heated; for details see text.

It is reasonable to assume that between 500K and 550K we observe the formation of a Pt-Fe alloy which is restricted to the surface layer. At these temperatures the thermal energy is not yet large enough to activate diffusion into the bulk but it may be sufficient to overcome the energy barrier for the formation of an alloy, which is energetically favored. The alloying may proceed through Pt-Fe exchange at the steps.

The fact, that below 450K an extremely low reflectivity minimum is observed at 0.5 ML coverage (Fig.6.2) cannot be explained by the presence of a strongly disordered layer. The minimum must rather be due to destructive interference of the He wave reflected from Pt and the wave reflected from Fe regions. The comparatively high reflectivity at 0.5ML above 450K would be well explained by a morphology in which no separate Pt and Fe areas exist and an alloy has formed.

At 500K and 550K we find an intensity minimum near 1ML coverage. This minimum strongly resembles the minima observed at 0.5ML for lower temperatures although it is less deep. We suggest that the minimum corresponds to the formation of a half monolayer of Fe on top of the PtFe alloy. This would mean that the alloy is completed at 0.5ML coverage, i.e. the alloy contains equal amounts of Fe and Pt atoms. A stable and ordered surface alloy with this composition has, in fact, been found by STM on the Pt(111) surface [65].

In order to study the dynamics of the process, which leads to alloying of the deposited Fe with the Pt substrate, we made experiments in which Fe deposition was stopped at small coverages and He scattering monitored the relaxation of the surface morphology. In a total of nine experiments three different Fe coverages (0.5 rows, 1 row and 1.5 rows) were deposited and the relaxation was observed at 450K, 475K, and 500K. The Figs. 6.10 to 6.12 show the results of these measurements. Evaporation begins at $t=0$. After reaching the respective coverage the evaporation is stopped by closing the shutter of the evaporator. At that instance the monitored He intensity changes from a negative to a positive slope. This change is in agreement with the above discussion, which assumed that the alloy exhibits a higher reflectivity than separated Fe and Pt areas. The initial slope of the recovery curve increases with both, temperature and coverage.

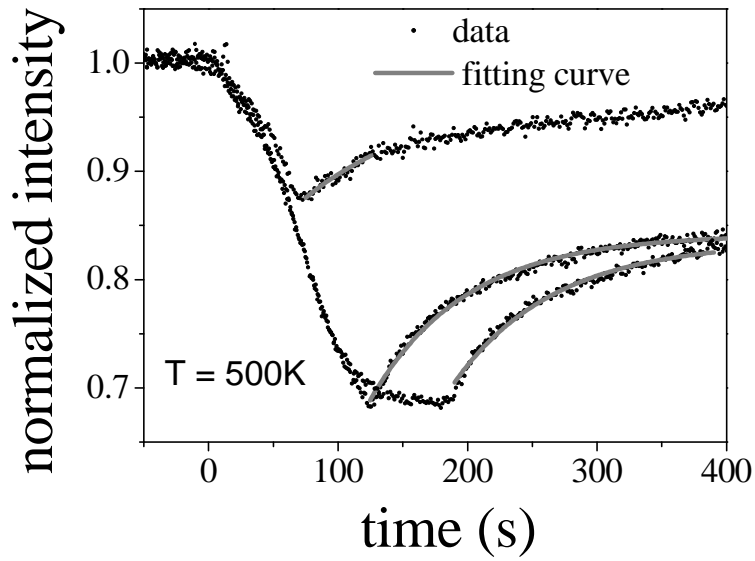


Fig. 6.10: Recovery of intensity after the deposition of 0.5 rows, 1 row, and 1.5 rows of Fe. The deposition of Fe starts at $t=0$. The end of the deposition is reflected by a substantial change of slope. $T = 500 \text{ K}$, $q_i = 57.8^\circ$, $q_f = 44.0^\circ$, peak $n = -3$, $\lambda = 1.01 \text{ \AA}$.

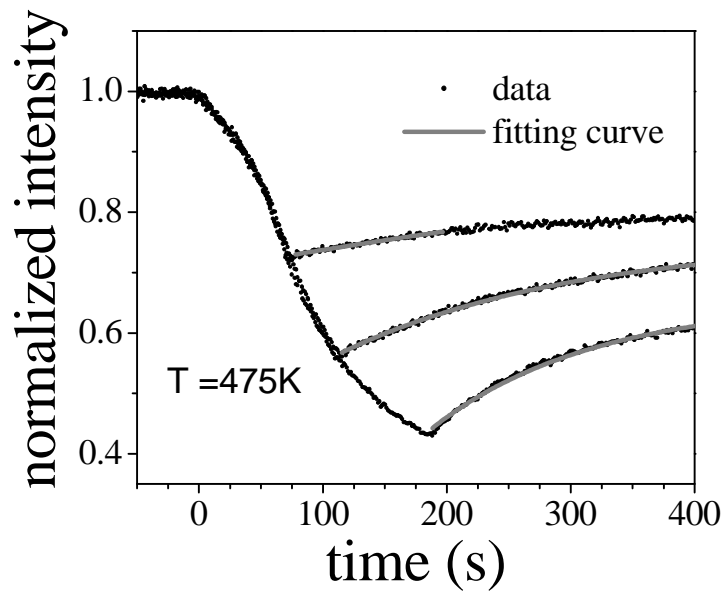


Fig. 6.11: Same as Fig.6.10 but for $T = 475 \text{ K}$.

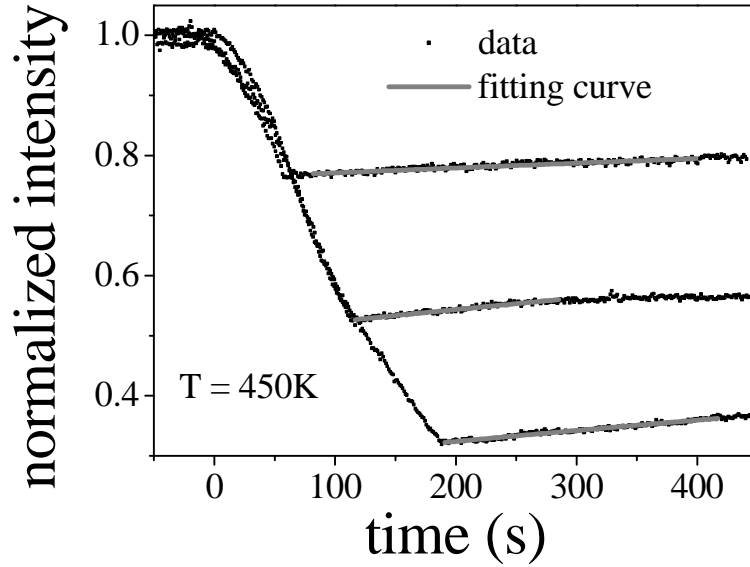


Fig. 6.12: Same as Fig.6.10 but for $T = 450$ K.

The time constants for intensity recovery were determined from fits of the data according to an exponential reflectivity increase:

$$I = I_0 - A \cdot \exp\left[-\frac{t-t_0}{\tau}\right] \quad (6.2)$$

where I_0 is the intensity after infinite time, A the change in intensity due to the structural transformations, $(t-t_0)$ is the time after the deposition was stopped, and τ is the time constant characteristic for the change of morphology. From an Arrhenius plot (Fig. 6.13) of the time constants obtained from the fitting we find, that the values for each Fe coverage lie on a straight line. This allows us to describe the recovery time by an Arrhenius function

$$\tau = \tau_0 \cdot \exp\left[\frac{E_c}{k_B T}\right] \quad (6.3)$$

where t_0 is a pre-exponential factor, E_c is the characteristic activation energy, k_B is the Boltzmann constant, and T is the substrate temperature.

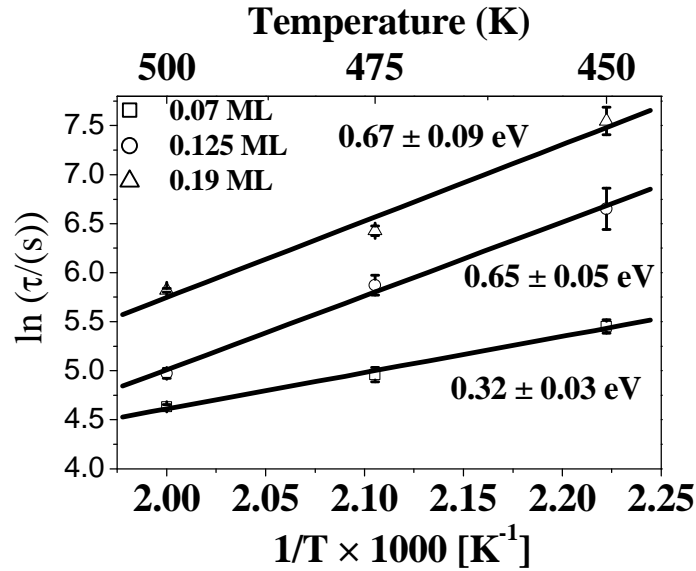


Fig. 6.13: Arrhenius plot of recovery time as a function of inverse temperature for different Fe coverages.

We can use eq. (6.3) to extract the activation energy E_c .

From Fig 6.13 we find two different activation energies depending on the Fe coverage. When the coverage is below one row we find a characteristic energy of 0.32eV. For a coverage superior or equal to one row we find an activation energy of 0.66 eV. These energies can be interpreted as the highest energy barrier to be overcome in the alloying process. They may represent one of the following energy barrier: the energy barrier for the exchange of Fe and Pt atoms at the step edge, the energy needed to create a vacancy in the terrace, or the diffusion barrier of either Pt or Fe between two vacancy sites. Only the latter possibility can be excluded, as this barrier does not depend on the number of rows attached to the step. It is not possible to choose which of the remaining two processes is connected to the measured barrier. Detailed STM measurements or theoretical calculations - both of which are not available yet - may help assigning the observed barriers.

6.4 Conclusions

For the growth of Fe on Pt(997) we found that a smooth first monolayer can be grown between 200K and 450K. A comparatively smooth second layer can only be obtained above 350K. Comparing this result to the cluster formation observed for one monolayer Fe deposited at room temperature on Pt(111) [63], one can assume that the smooth growth of the first two layers is induced by the high regular step density of the Pt(997) substrate. Decoration of the substrate step by a monatomic Fe row is observed between 175K and 600K with optimal conditions around 300K. Between 450K and 550K we find strong indications that a surface layer restricted alloy is formed. Its completion at 0.5ML coverage and the results of earlier STM studies suggest the formation of an ordered PtFe alloy. Activation energies for the alloying process have been determined experimentally. For temperatures ≥ 600 K the diffusion of Fe atoms into the Pt bulk starts to play an important role.

CHAPTER 7

Mo and Rh growth on Pt(997)

7.1 Introduction

The interest in magnetic studies of nanometer size structures is not restricted to elements that are ferromagnetic in the bulk. Several elements have been predicted to become ferromagnetic as nano-size structures adsorbed on a surface even though they do not exhibit volume ferromagnetism. In this chapter we present a study of growth morphology of Mo and Rh on a Pt(997) surface. Based on density functional calculations both, Mo and Rh, were predicted to exhibit a permanent magnetic moment for nanometer structures on Ag(100) in the low temperature limit [4].

While Pt and Rh crystals both have a face centered cubic (fcc) structure, Mo has a body centered cubic (bcc) crystal structure. The lattice constants of Rh and Mo are 3.80 Å and 3.15 Å, respectively, [72] leading to a nearest neighbor distance of 2.69 Å and 2.73 Å, respectively. Both values are slightly smaller than the Pt nearest neighbor distance of 2.77 Å. From DFT calculations it was derived that Mo on Pt has a strong tendency for alloying and antisegregation. Rh on Pt exhibits the same behavior, however, with weaker energy differences and thus weaker driving forces [69].

In a field ion microscopy (FIM) study the growth of a vacancy-free Mo adlayer was observed on a Pt(111) tip [73]. A more recent combined LEED and Auger spectroscopy study [74] arrives at the conclusion that Mo on Pt(111) does not exhibit a simple layer-by-layer growth. In the study strong effects of alloy formation were found and thus the evaluation of Mo coverages at the surface turned out to be difficult.

While alloys of Pt and Rh have been extensively studied [75-77] only one study on Rh growth on Pt(111) could be found [78]. The authors of the combined electrochemical and UHV study employing Auger spectroscopy and LEED arrived at the conclusion that below 400K a "pseudo layer-by-layer" growth takes place in which the second and third layer grow before completion of the first layer. At increased temperature the deviation from layer-by-layer growth increased and the formation of bulk-like polycrystalline Rh was observed. Alloying was observed to occur at 873K.

7.2 Experimental

The Pt(997) surface was prepared with the usual procedure (see chapter 4). The cleanliness of the surface was checked with AES.

The base pressure in the chamber was 2×10^{-10} mbar. Mo and Rh were evaporated from electron beam evaporators, which were equipped with a 1mm diameter molybdenum rod with a purity of 99.99% and a 1mm diameter rhodium rod with a purity of 99.999%, respectively. We remark that the melting temperatures of Mo and Rh are 2890K and 2239K, respectively. As a result, the heating power required for evaporation is substantially higher than for most other elements e.g. Fe or Ag. Still, during the evaporation the pressure in the chamber rose to only 4×10^{-10} mbar.

The rhodium flux was typically 1×10^{-3} ML/s. The flux was calibrated via monitoring the deposition on the $n = -3$ diffraction peak (non-grazing geometry).

7.3 Results

7.3.1 Mo growth

Figure 7.1 shows Mo growth for temperatures between 150K and 600K monitored in non-grazing geometry ($n = -3$ diffraction peak). For all temperatures the He reflectivity decreases monotonously. No local reflectivity maxima are observed which could clearly be ascribed to monolayer completion. Between 250K and 350K a change in the slope after about 750 s of evaporation is observed which may however indicate the completion of the first layer. The absence of a maximum with high reflectivity demonstrates a

continuously increasing surface roughness. At high temperatures this may be due to the formation of an alloy. At the lowest temperatures, no alloy formation should be possible and the result suggests 3-D growth due to a low mobility of Mo atoms.

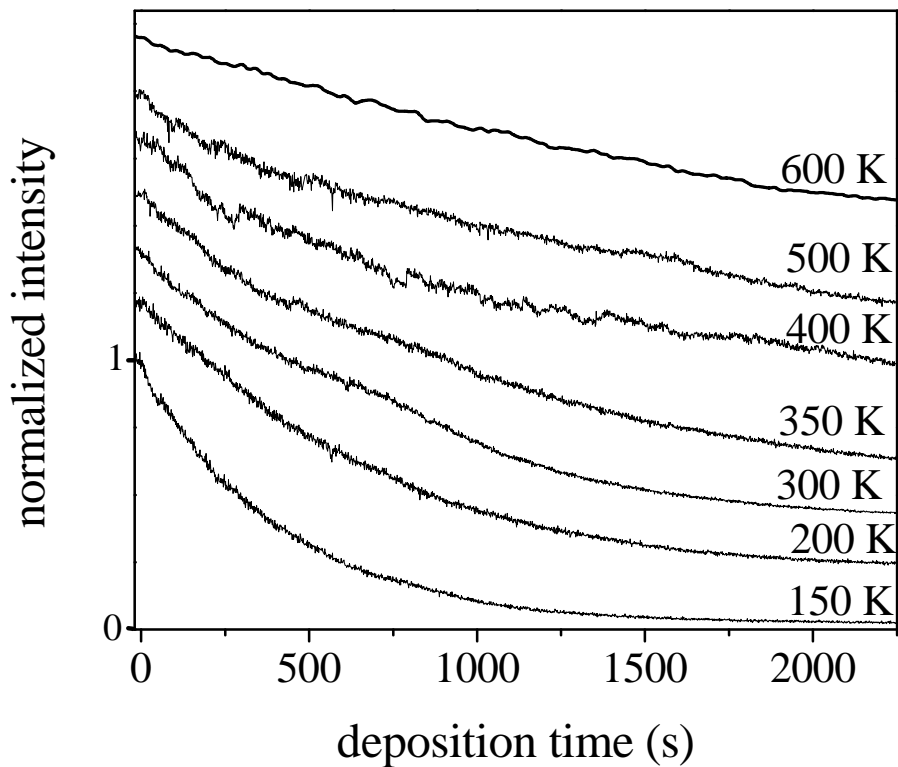


Fig. 7.1: Mo deposition monitored on the $n = -3$ diffraction peak for surface temperatures between 150K and 600K. $q_i = 57.8^\circ$, $\chi = 101.8^\circ$, $\lambda = 1.01 \text{ \AA}$. The curves have been normalized to the intensity of the clean substrate; the curves were vertically offset by multiples of 0.5 units.

In the absence of any clear monolayer peak we did not attempt to calibrate the flux from the evaporator and calibrate the Mo coverage. After stopping deposition in the above measurements full diffraction scans were taken (Fig.7.2). The total deposition time was between 2800s (at 150K) and 3500s (at 500K). If we assume that it takes 750s to

evaporate a monolayer we can tentatively suggest a coverage of 4.2 ML (± 0.5 ML). At 150K the $n=-3$ diffraction peak is still buried in the background counting rate. The peak starts to become visible at 300K and increases with increasing temperature. The behavior can be a result of two activated processes: Diffusion at the surface, which increases order, and diffusion into the bulk, which reduces the Mo coverage on the surface. Bassett [74] finds that diffusion into the bulk is present above 700K.

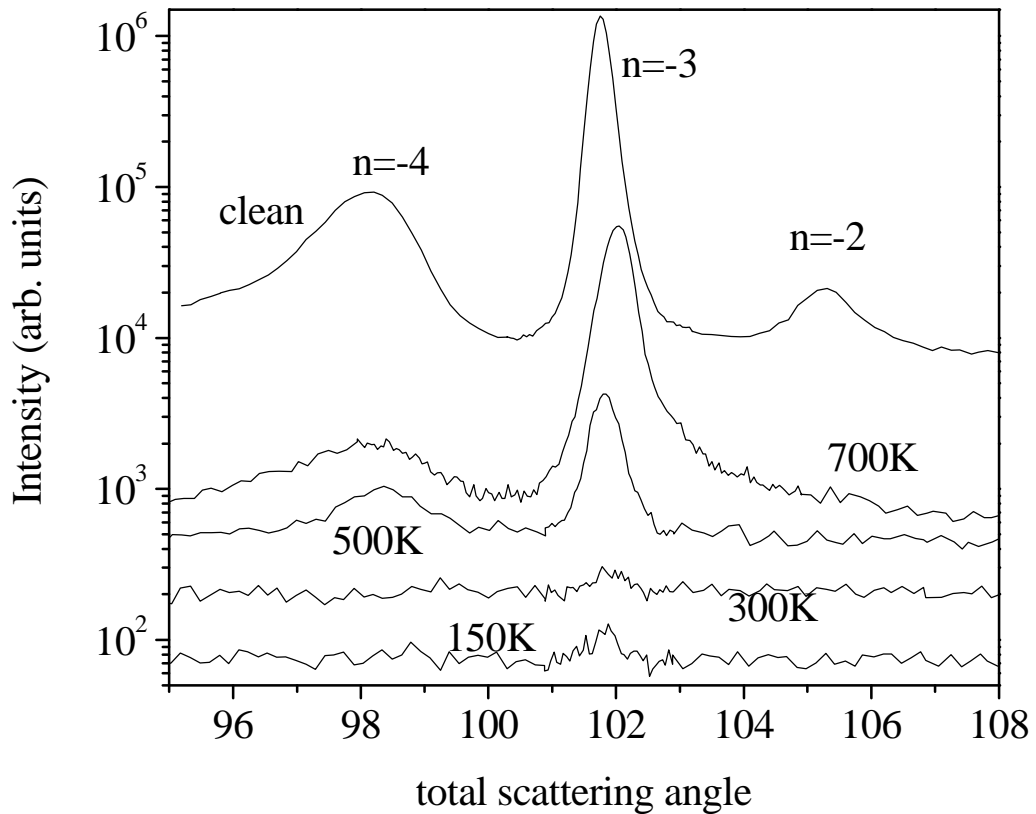


Fig. 7.2: Diffraction pattern of Pt(997) after approximately 300s of Mo deposition at the indicated temperatures, $q_i = 57.8^\circ$, $\lambda = 1.01 \text{ \AA}$. Each curves is shifted by a factor of 2 with the respect to the curve below.

This agrees with the results we obtained by Auger spectroscopy: Fig.7.3 shows the evolution of the 28 eV Mo peak and the 43 eV Pt peak as a function of annealing temperature. Initially, Mo was deposited for 2400 s at 120 K. The Auger spectra were taken at intervals of 50K (about 15 minutes). The Mo concentration starts to decrease significantly at 750 K.

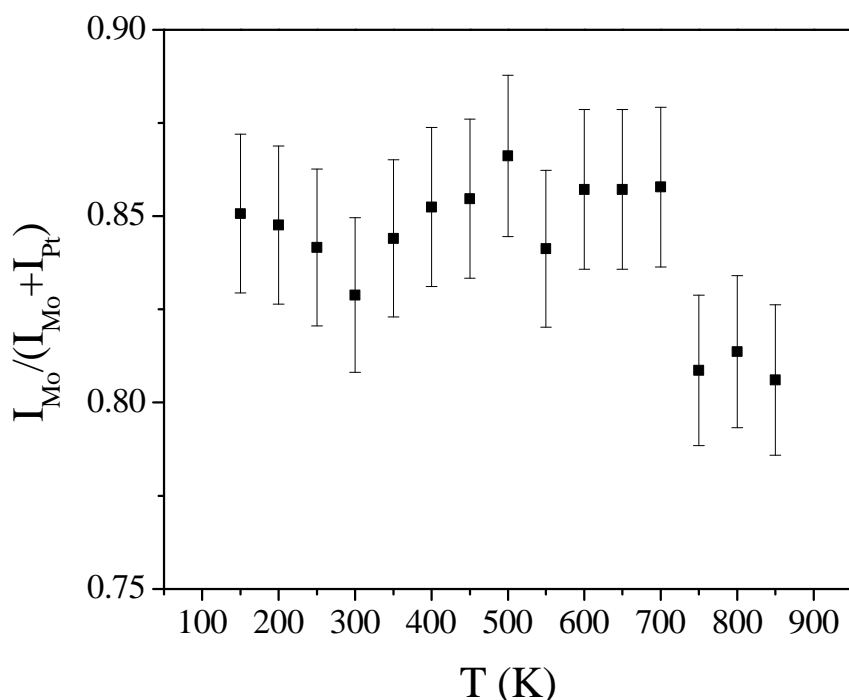


Fig. 7.3: Evolution of the ratio of Mo and Pt AES peak as function of temperature.

We now address the question of step decoration and row formation at the step. Fig. 7.4 shows adsorption curves monitored under grazing scattering geometry.

The measurement demonstrates that even at the step no regular structure with low defect density is formed for any of the temperatures (150K-500K). This indicates that diffusion from the second row at the step towards the first row (diffusion past kink sites) or possibly even Mo adatom diffusion on the terraces is suppressed. We may speculate on

the morphology during Mo growth that only small islands can form, which grow two-dimensionally.

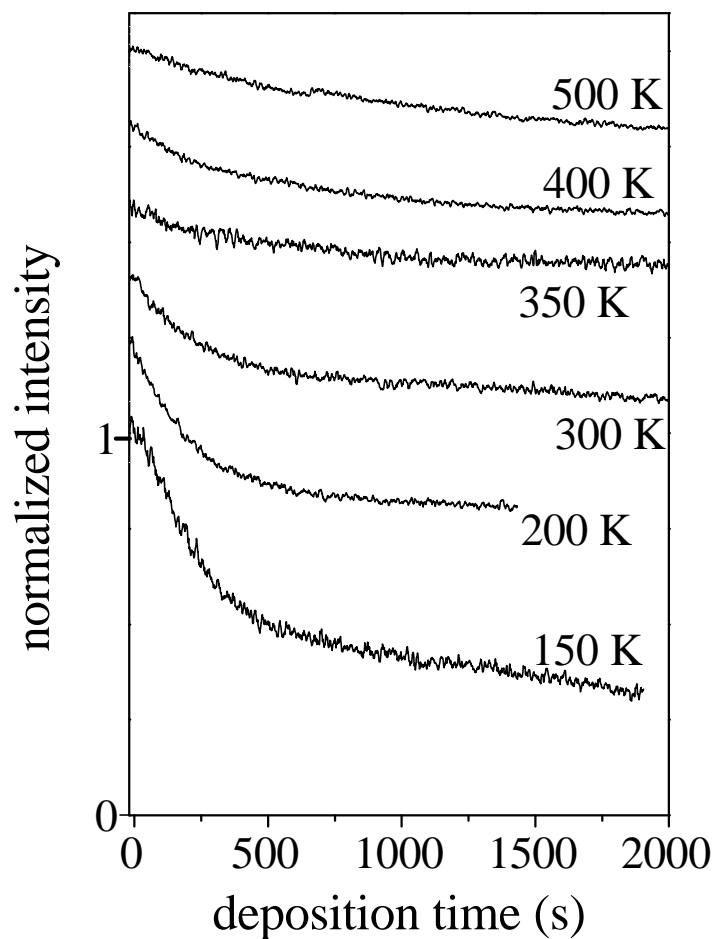


Fig. 7.4: Mo deposition on Pt (997) monitored under grazing geometry ($n = 0$ peak) for the indicated temperatures. $q_i = 85^\circ$, $\chi = 170^\circ$, $\lambda = 1.01 \text{ \AA}$. The curves were normalized and vertically offset by multiples of 0.2 units.

7.3.2 Rh growth

The study of the Rh/Pt(997) system in this chapter is only preliminary and not complete. The results are, however, sufficient to indicate the basic growth behavior.

Figure 7.5 shows the Rh growth for temperatures between 200K and 700K monitored by He scattering in non-grazing geometry ($n = -3$ diffraction peak).

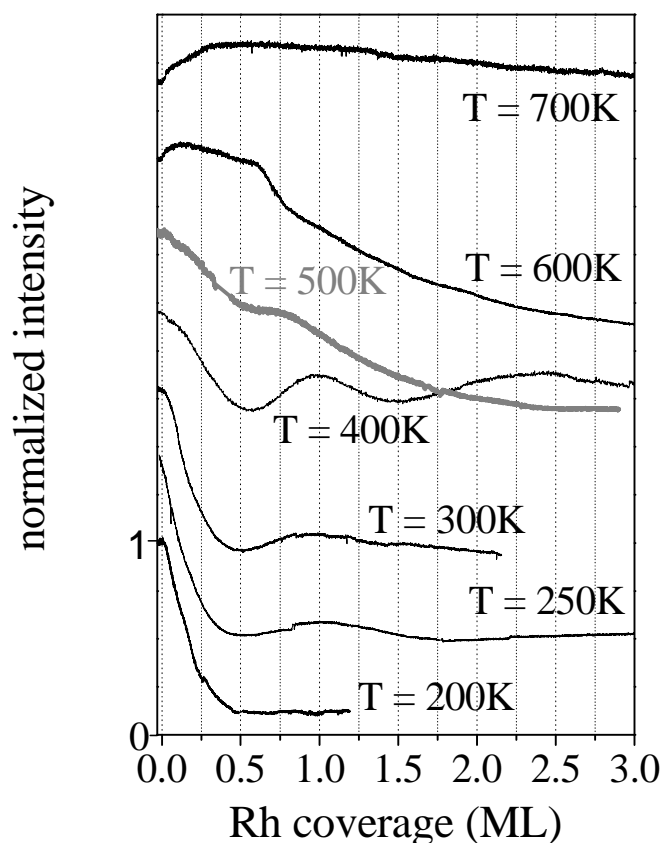


Fig. 7.5: Rh deposition on Pt (997) monitored under non-grazing geometry ($n = -3$ peak) for the indicated temperatures. $q_i = 57.8^\circ$, $\chi = 101.8^\circ$, $\lambda = 1.01 \text{ \AA}$. The curves were normalized and vertically offset by multiples of 0.4 units.

In contrast to Mo deposition and similar to the case of Fe (chapter 6), a maximum in intensity is observed which can be ascribed to the formation of a first monolayer. The maximum is most pronounced between 250K and 400K. At temperatures below 250K monolayer formation is not observed. At temperatures above 400K different features are

observed which require further investigation. Although the features appear to be different from the case of Fe/Pt(997) growth (chapter 6) their origin may be alloying similar to the case of Fe.

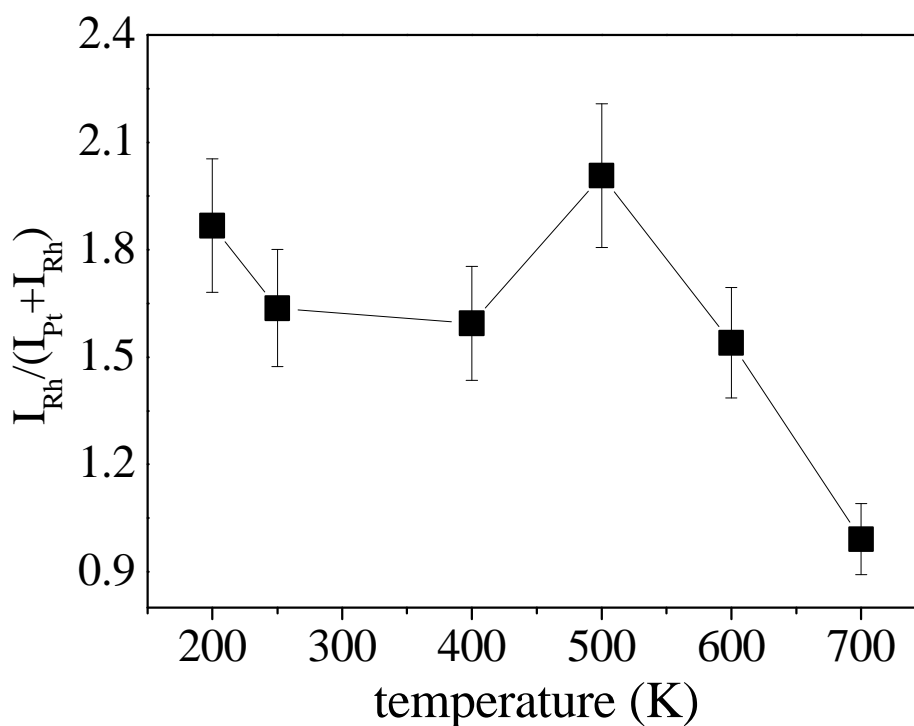


Fig. 7.6 Relative Rh Auger signal as a function of temperature.

Rh diffusion into the Pt bulk was studied by Auger spectroscopy: 1ML of Rh is deposited at 200K; then the sample is heated to a given temperature where the AES spectrum for that temperature is acquired. For the evaluation of intensities the Rh 302 eV peak and the Pt 64 eV peak were used. The result is shown in Fig.7.6. Within the precision given by the error bars the Rh concentration at the surface starts to decrease between 600K and

700K. This result is in good agreement with the electrochemically obtained result by Attard et al. [78] that alloying sets in between 623K and 873K.

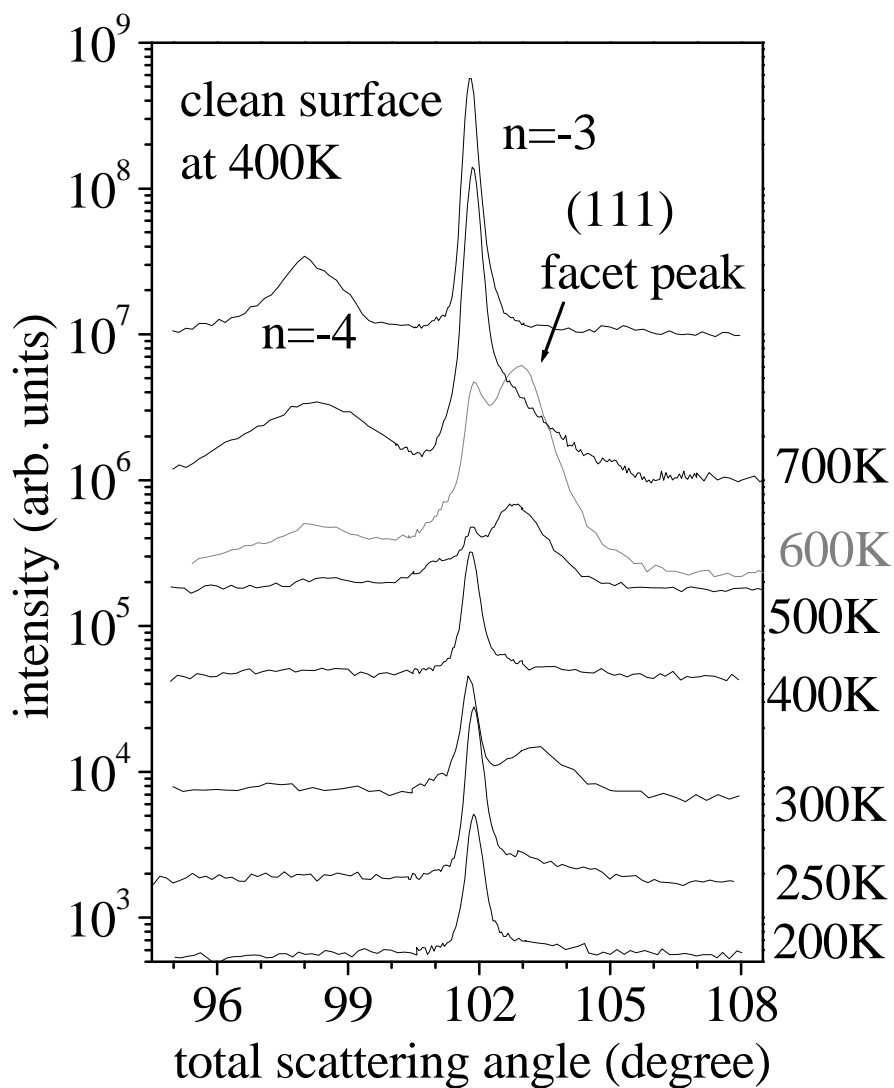


Fig. 7.7: Diffraction pattern for Pt(997) after deposition of Rh at the indicated temperatures, $q_i = 57.8^\circ$, $f_i = 51.4^\circ$, $\lambda = 1.01 \text{ \AA}$. The coverage varies between 3 and 4 ML except for the case of 200K where the coverage is only 1.25 ML. Each curve is shifted by a factor of 4 with respect to the curve below.

After the deposition of thin Rh films (for the detailed thickness see the figure caption of Fig.7.7) He diffraction scans were recorded in order to obtain information on the morphology of the surface (Fig.7.7).

The most striking feature is the appearance of a facet peak for 500K and 600K. It indicates the presence of (111) facets, about 60 Å in width at 600K. The formation of facets may be restricted to this temperature range because of the low mobility of Rh atoms at lower temperatures and the starting bulk diffusion of Rh at 700K.

The growth of Rh at the step edge was investigated at grazing scattering geometry (Fig.7.8).

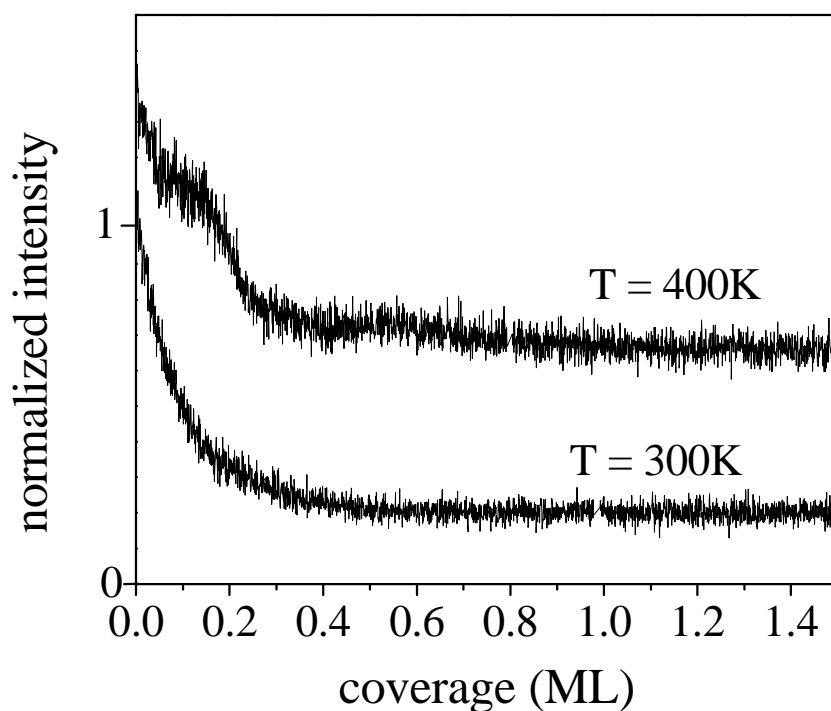


Fig. 7.8: Rh deposition on Pt (997) monitored by the $n = 0$ peak for two temperatures. $q_i = 85^\circ, \chi = 170^\circ, \lambda = 1.01 \text{ \AA}$. The 400K curve is shifted upwards by 0.3 units.

A shoulder in the reflectivity as a function of coverage indicates the formation of a row at the step edge at 400K. A similar shoulder was observed for substrate temperatures up to 600K and was absent at 700K (measurements not shown). From these preliminary results we can conclude that the growth of a row of Rh at the Pt(997) step edges occurs at and above 400K. The low intensity of the shoulder, however, may indicate that the formed row may contain a high density of defects.

7.4 Conclusions

Mo grows in a three-dimensional mode on Pt(997). The observation is in good agreement with the earlier LEED/AES study [73, 74]. We do not find a forced growth of smooth adlayers induced by the high step density of Pt(997) as it was observed for Fe (chapter 6). In our experiments no condition was found which allow a defined growth of nanowires. Mo is the first element for which we observe this behavior.

Rh exhibits the formation of a smooth first monolayer on Pt(997) between 250K and 500K. Diffusion into the Pt bulk begins around 700K. Between 400K and beginning bulk diffusion a monatomic row can be grown at the substrate steps. Although the temperature range between 500K and 700K has not been studied intensively, it appears probable that similar to the case of Fe deposition (chapter 6) a surface alloy may be obtained. The structures formed by Rh appear, however, to be less well ordered than in the case of Fe, which is indicated by the low reflectivity even under conditions where minimum defect density is obtained. In contrast to Mo the mobility of Rh is obviously high enough to realize structures with a high regularity.

CHAPTER 8

Ag-Cu bimetallic wires

8.1 Introduction

The growth of bimetallic nanometer-sized patterns is of substantial interest because of the model character of such structures in the fields of catalysis and material science. Understanding crystal growth in low dimensions is a prerequisite for creating and studying alloying in low dimensions and reactivity of well-characterized nanostructures.

A previous TEAS study [5] investigated the growth of Co-Ag and Ag-Co metallic double wires on a (997) surface. These structures were grown by the deposition of one monatomic row of a metal at the step edge followed by continuous deposition of a second metal. Information on the growth is obtained particularly by monitoring the TEAS reflectivity of the growing second metal. It was found that deposition of Co followed by the deposition of Ag resulted in smooth well-organized structures at temperatures below 250K whereas the deposition of Ag followed by the deposition of Co did not create ordered structures which indicated the on-set of alloying in the system.

These results were confirmed by theoretical calculations [5] that shed light on the energy balance of bimetallic structures at step edges and the occurrence of alloying. They opened a way to predict the thermodynamic stability of bi-metallic structures grown at substrate step edges.

The growth of monatomic wires at steps is the 1-dimensional equivalent of the creation of metallic sandwich layers [24]. The stability of element-separated sandwich layers is determined by the surface free energy of the element in the top layer and the interface energies at the two bi-metallic interfaces metal-I/metal-II and metal-II/substrate. In

addition the possible reduction of free energy due to alloying has to be taken into account. Growing rows of different elements at a step edge requires a similar reasoning whereas the determination of exact results becomes somewhat more demanding.

Studying growth at steps by monitoring the He reflectivity gives us information on the smoothness of layers and step edges. The method is not inherently chemically sensitive. Only in rare cases detailed information on alloying can be obtained. This study of bi-metallic wires is thus another step in addressing these rather complex systems. For future studies it may become necessary to employ element and site specific methods.

In this chapter we will investigate bi-metallic structures of Ag + Cu rows on Pt(997). The system is of specific interest because the theoretical study based on an Ising model [5] predicted the thermodynamic behavior of the system: An almost element-separated (i.e. non-alloyed) system is stable when Cu is deposited as the first element and the inverse order of deposition corresponds to a metastable structure which may be obtainable under typical experimental conditions.

It is known from experiment [3, 17, 22] and calculations [5] that the growth of the first row of Ag or Cu is always favorable. On inspection of the segregation energies and the mixing tendencies for binary surface systems from [69] one may obtain a first idea of the behavior of the systems from their surface properties: In equilibrium, Ag tends to segregate on the Pt surface while Cu atoms do not. Alloying at the Pt surface is favored for Cu while it is not favored for Ag. For both, the Ag/Cu and the Cu/Ag systems there is a tendency of surface segregation of Ag and miscibility of the two elements at a surface.

8.2 Experimental

To monitor the deposition of the metals we used He scattering in grazing geometry ($\theta_i = \theta_f = 85^\circ$). In this geometry we are mainly sensitive to the phenomena taking place at the step edges. The creation of a first row at the step edge is accompanied by a maximum in the reflectivity of the diffracted beam (see chapter 4). Due to the width distribution of the terraces on the Pt surface it is not possible to obtain a similarly strong peak in the diffracted intensity after the first row has been completed. A broad peak around 0.5 ML coverage can be taken as an indication for continuing row-by-row growth [5]. In our experiments we will focus on that peak and on a maximum observed around monolayer coverage.

Ag and Cu were evaporated from crucibles heated by electron bombardment. The deposition of the first element took place at the same temperature as the deposition of the second. This means that the deposition of the first element did not always take place under optimum growth conditions. After the deposition of 0.13 ML the deposition was stopped and after some 15 s the deposition of the second element started. The data points recorded between the deposition of the two elements have been removed from the presented data.

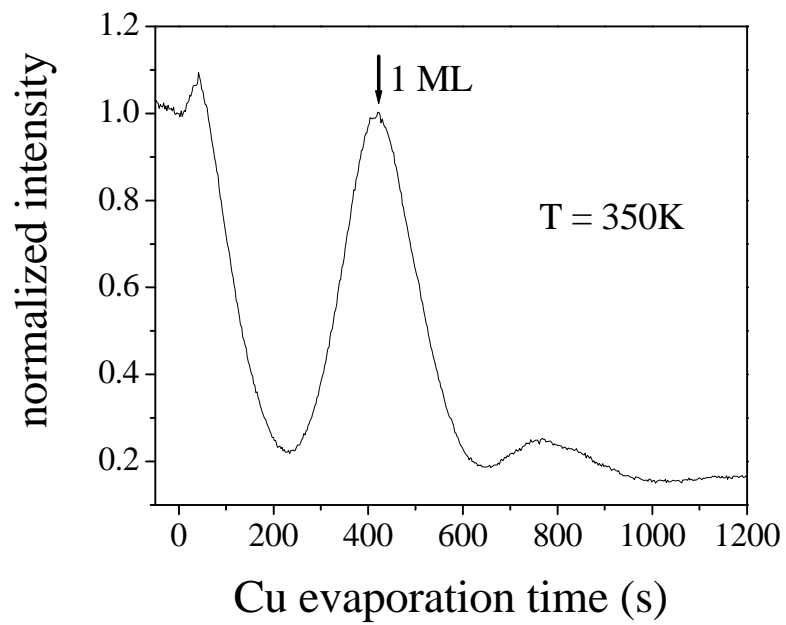


Figure 8.1: Calibration curve for the flux of Cu, $\theta_i = 57.4^\circ$ $\theta_f = 44^\circ$.

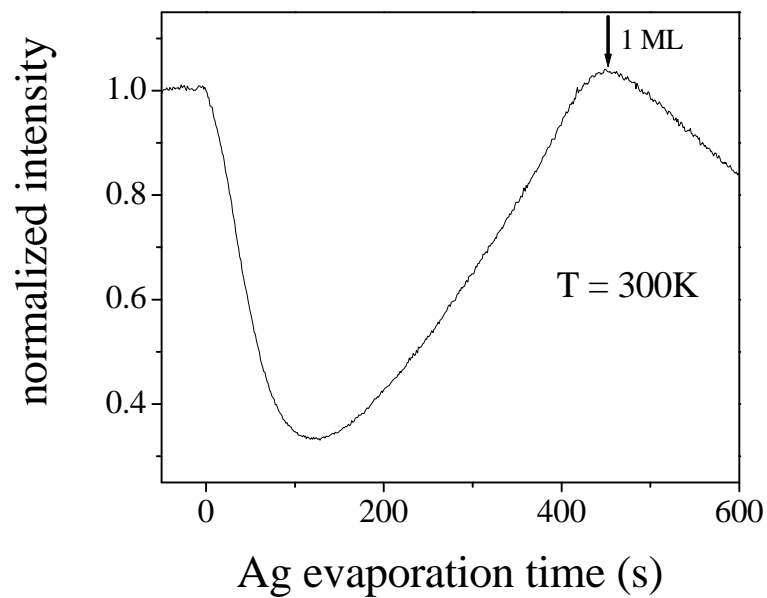


Figure 8.2: Calibration curve for the flux of Ag, $\theta_i = 57.4^\circ$ $\theta_f = 44^\circ$.

The calibration of the flux was done for both elements by recording the diffracted intensity in non-grazing geometry ($\theta_i = 57.4^\circ$ $\theta_f = 44^\circ$) where the first maximum corresponding to the completion of a monolayer. The typical flux was between $1 \cdot 10^{-3}$ ML/s and $3 \cdot 10^{-3}$ ML/s. Examples of calibration curves for Cu and Ag are given in Figs. 8.1 and 8.2, respectively. Due to variations in the real flux of the evaporated elements for similar evaporation conditions the calibration has a reproducibility error of about $\pm 15\%$. This error also effects the pre-deposition of the first element, which may lead to a corresponding over or under deposition of the amount need for exactly one row. This error is approximately of the same size as the local deviation (about 20%) of step coverage, which is due to the width of the terrace size distribution on a perfectly prepared sample.

8.3 Results

8.3.1 Ag/Cu-row/Pt(997)

Figure 8.3 shows the results for the experiments in which one Cu row was deposited before Ag is deposited. This corresponds to the evaporation order that is assumed to result in a stable non-alloyed structure. We find that upon Ag deposition a strong increase of the intensity is observed for temperatures up to 300K. The coverage for the peak intensity appears to shift to higher coverages with increasing temperature. At the lowest temperature (200 K) the intensity of the bi-metallic structure even exceeds the intensity of the clean step edge. This maximum occurs for a coverage of about 0.35ML (3 rows). Judged from its reflectivity this appears to be one of the best ordered bi-metallic structures that have been obtained. Between 250K and 450K, i.e. for a wide temperature range, the intensity increases strongly when monolayer completion is approached. For pure Cu this was only observed at 600K [79]. This increase in intensity can be due to the formation of an ordered alloy. Cu starts to alloy with Pt on a (111) surface above 500 K. But since intermixing is favored at step edges the alloying temperature can be lower on Pt(997). This may explain the high temperature limit for the growth of stable structures at about 350K.

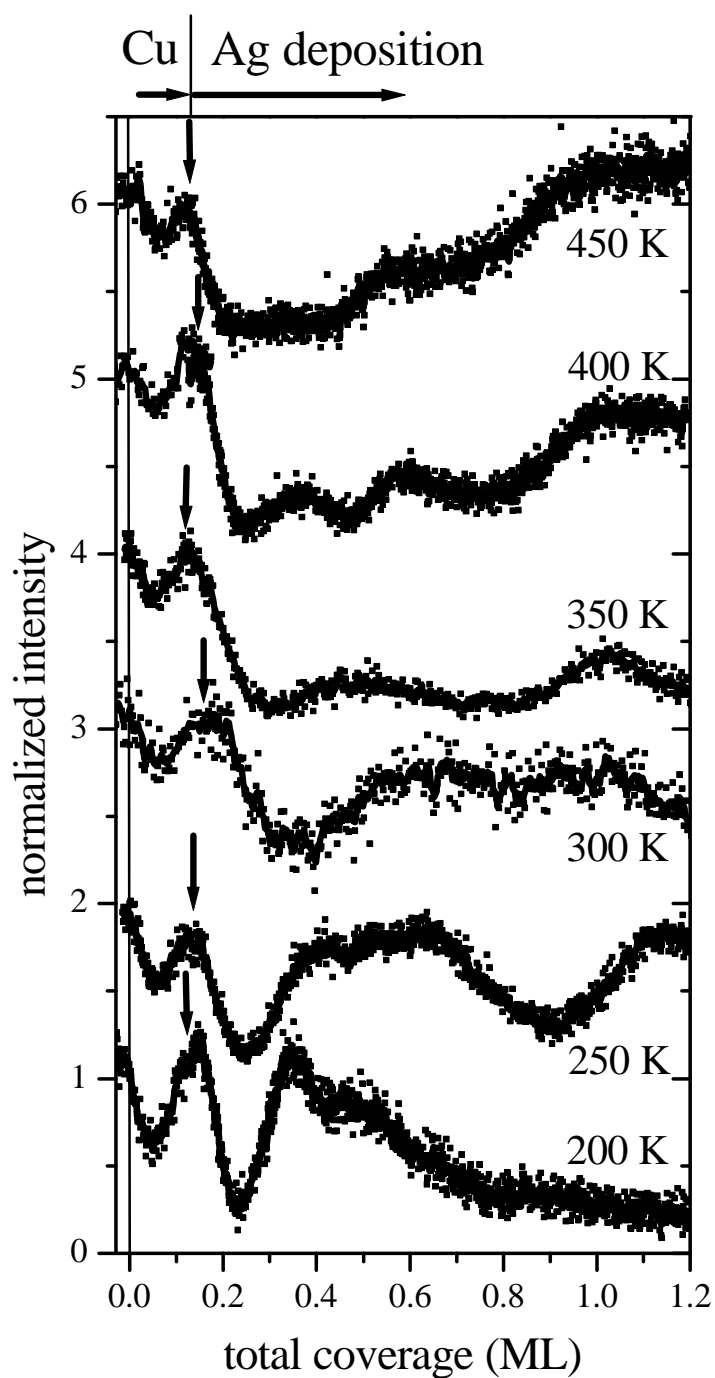


Figure 8.3: Deposition of Cu followed by Ag at the indicated temperatures monitored under grazing scattering geometry, ($n=0$), $\theta_i = 85^\circ$, $\theta_f = 85^\circ$. The curves for $T > 200\text{K}$ were offset by multiples of 1.

8.3.2 Cu/Ag-row/Pt(997)

Fig. 8.4 shows the results for the experiments in which one Ag row (0.13ML) was deposited before Cu deposition. In the experiments the reflectivity at completion of the Ag row was reproducibly lower than observed in earlier experiments [3, 17, 22]. The reason for this is not clear. However, we could exclude that this be due to strongly inhomogeneous deposition (evaporator alignment), an exhausted Ag source, and poor sample preparation. We also remark that the data sets shown in Fig.8.3 and Fig.8.4 were measured in a mixed fashion why the same problems should have appeared in both data.

An intensity maximum near 0.5ML is visible at 250K. It disappears above 325K. Similar as in the case of the opposite deposition order this peak appears to shift with higher temperature towards higher coverages. The intensity minimum observed at 0.5ML at 200K was reproducible. The high reflectivity at 200K around 0.25ML appears to continue the shift of the 0.5ML peak towards low coverage. A minimum between the deposition of the first row and this peak, which would indicate a half-filled second row, is barely visible. A possible explication might be a kink flow growth for which the number of kink-defects does not increase up to a coverage of 0.3ML. No peak at monolayer completion is observed in the studied temperature range.

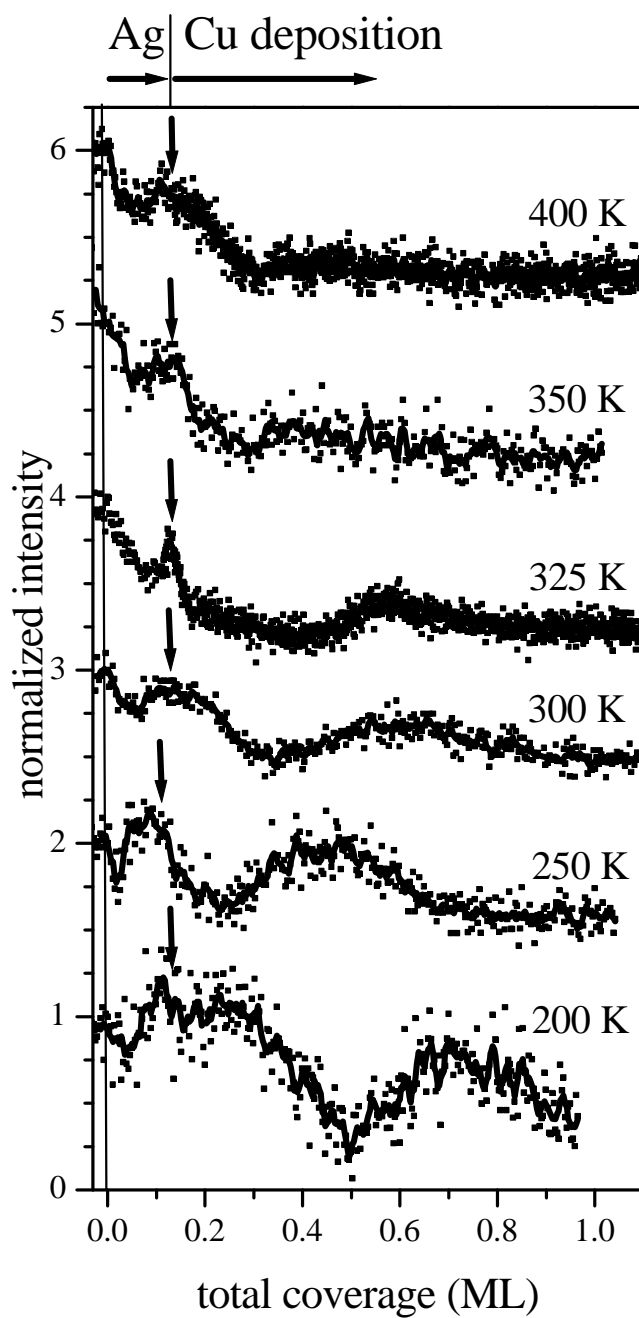


Figure 8.4: Deposition of Ag followed by Cu at the indicated temperatures monitored under grazing scattering geometry, ($n=0$) $\theta_i = 85^\circ$ $\theta_f = 85^\circ$. The curves for $T > 200\text{K}$ were offset by multiples of 1.

8.4 Discussion and Conclusion

The experiments show that during the growth of Ag on Cu-row/Pt(997) maxima with high reflectivity are observed up to 300K. The stability of this growth order is in good agreement with the theoretical results for the system [5]. Actually Ag is an element with one of the lowest surface free energies [69]. It has the tendency to exchange with atoms occupying sites with lower coordination. This is reflected in the possibility to protect Pt samples by the evaporation of Ag thin films as stable "capping". Similar to the case of Ag/Co-row/Pt(997) a "capping" of the step edge by a Ag row results in a high stability of the structure.

Deposition of Cu after evaporation of one row of Ag does not correspond to the energetically favored arrangement. However, the tendency for Cu and Ag atoms to exchange sites is weak enough to prevent this exchange. Moreover, with beginning exchange the system has to move up an energy barrier before it can arrive at its most favorable arrangement [5]. For this reason the reverse order does not rearrange during its preparation. This corresponds to a metastable arrangement. The fact that in this arrangement the reflectivity at 0.5ML and 250K exhibits a high maximum demonstrates that this behavior is actually observed. The occurrence of Cu-Ag exchange processes would disorder the structure and suppress the appearance of a reflectivity maximum as it is, in fact, observed for Co/Ag-row/Pt(997) where no metastable structure with reversed order is expected from theoretical consideration.

We can thus conclude that the experimental study supports the theoretical prediction that Cu and Ag rows can be attached in an ordered structure at the Pt(997) steps independent in which order of the two elements are deposited.

CHAPTER 9

New energy analysis detector

9.1 Introduction

Inelastic measurements require the energy analysis of the scattered He beam. The standard method relies on the time of flight (TOF) method [81]: The beam is chopped into short pulses and then the flight time between chopper and detector is measured. This method is efficient especially with a pseudo random chopping system [82] but the energy resolution is limited to $\Delta E/E \approx 0.01 \dots 0.02$ by different contributions [83]. These contributions are the shutter function of the beam chopper, the length of the ionization region, and the length of the flight path.

An alternative method is the selection of different wavelengths by scattering from a highly corrugated surface in a diffraction peak of non-zero order. The use of an echelette grating for this purpose has been proposed by Kuhnke *et al.* [84]. An example of such a surface is Pt(997) which has been described in detail in chapter 4. By rotating the crystal different wavelengths are selectively scattered into the ionization detector. The wavelength can be calculated from the scattering geometry. This method allows in principle to improve the energy resolution of the detector to the point where the angular width of the reflected beam is determined by the quality of the diffracting crystal.

9.2 Detector set up

Fig.9.1 shows a detailed view of the detector set-up. The other components of the He scattering apparatus were described in Chapter 3.

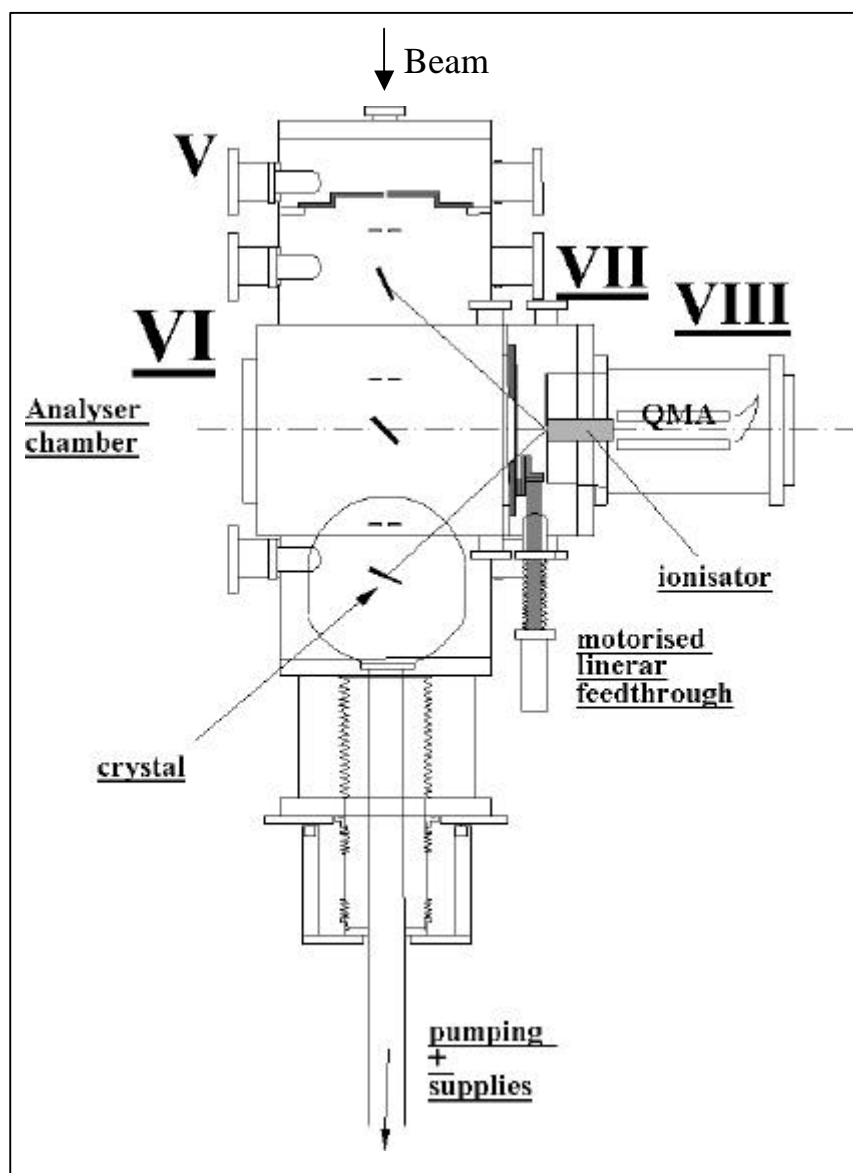


Fig. 9.1: Top-view of the analyzer.

Chamber V and VII are operated as differential pumping stages serving the purpose to decrease the final background pressure in the ionizer. The Pt(997) surface echelette grating is situated in chamber VI. It is mounted at the end of an arm allowing linear motion in the x, y, and z directions preformed from outside the chamber by three motorized linear stages. The absolute positioning of the crystal is controlled via a commercial measuring system (Ls 303C Heidenanhain).

Polar, azimuth and tilt angle of the Pt(997) crystal are adjusted with the help of goniometers located in a separate vacuum chamber below the crystal, because the goniometers and stepping motors are not UHV compatible. The rotation is transmitted through a flexible bellows to the sample. The idea was initially developed by H.Schief [13, 85] and further developed by M.Blanc [24]. The absolute position of the polar angle is controlled by a commercial rotary positioning measuring device system (ERO 1251 from Heidenhain) with a precision better than 0.001° . The accuracy in mechanical tilt and azimuth positioning is better than 0.01° .

9.3 Energy analysis

Fig. 9.2 shows the scattering geometry of the diffractive analysis spectrometer (DAS). Only the z movement and the polar degree of freedom are represented. The other degrees of freedom (x, y, tilt, and azimuth) are employed to correct for mechanical deviations. z can be scanned from +200 mm to -300 mm with the zero position being defined as the position for which the total scattering angle is 90° . The polar angle (\mathbf{q}_i) can be varied between 75° and -100° .

In order to obtain a maximum energy resolution the diffracted peak of a monochromatic beam must have minimum width. Thus the diffraction peak must be chosen to be in the ideal condition (see chapter 4). z and \mathbf{q}_i for the ideal position are a function of the energy which shall be selected.

If l_d is the distance between the detector entrance and the z-axis then we have

$$\frac{z}{l_d} = \tan(\mathbf{q}_i + \mathbf{q}_f - \frac{\mathbf{p}}{2}) \quad (9.1)$$

By introducing the ideal condition eq. (4.6) and using $\mathbf{f} = (\mathbf{q}_i + \mathbf{q}_f)/2$ we obtain

$$\mathbf{f} = \frac{\mathbf{p}}{4} - \frac{1}{2} \arctan\left(\frac{z}{l_d}\right) \quad (9.2)$$

and

$$I = \frac{2h}{n} \cos\left(\frac{\mathbf{p}}{4} - \frac{1}{2} \arctan\left(\frac{z}{l_d}\right)\right) \quad (9.3)$$

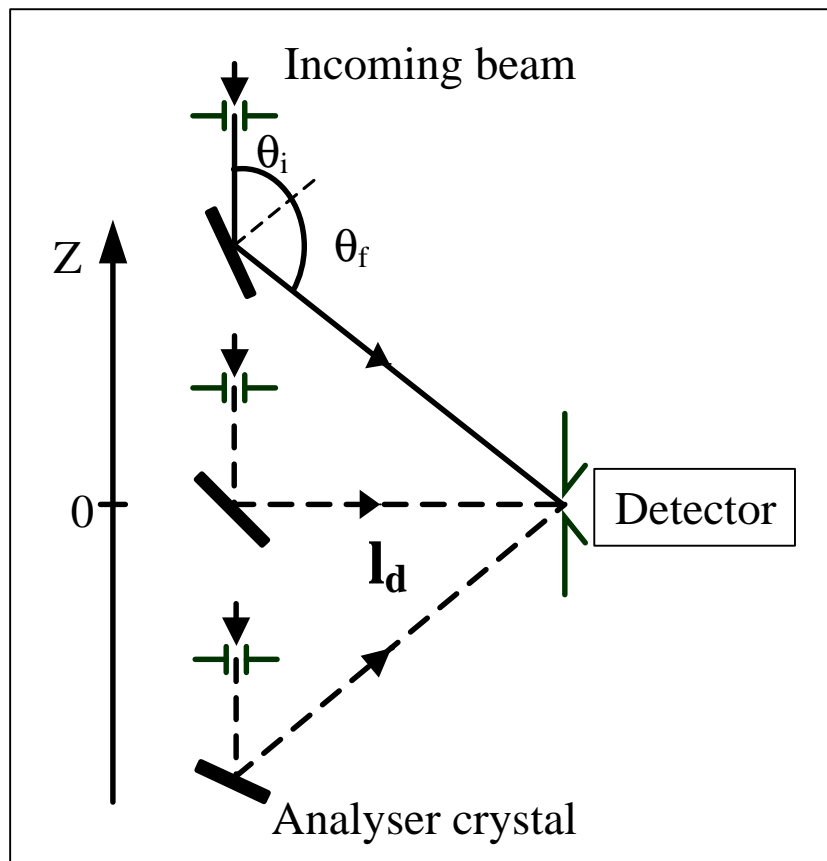


Fig. 9.2: Scheme of the DAS.

The relation between I and E is

$$E = \frac{h^2}{2m_{\text{He}} I^2} \quad (9.4)$$

where h is Planck's constant and m_{He} is the mass of one He atom, Using 9.4 we get

$$E = h^2 / \left(2m_{\text{He}} \left(\frac{2h}{n} \cos \left(\frac{\mathbf{p}}{4} - \frac{1}{2} \arctan \left(\frac{z}{l_d} \right) \right) \right) \right)^2 \quad (9.5)$$

The selected energy as a function of the z coordinate is given for different diffraction orders in Fig.9.3.

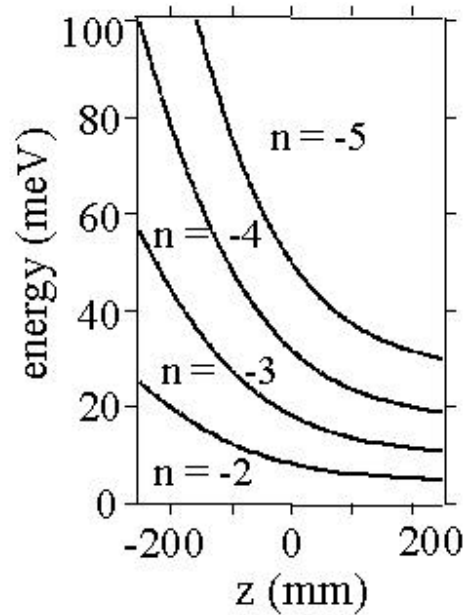


Fig. 9.3: Available energy as a function of z coordinate for different diffraction orders n .

Energies between 10 meV and 100 meV can be selected in at least two different diffraction orders. This allows the unique assignment of observed inelastic features. The possibility to measure each energy in at least two different diffraction orders is also required to calibration the detector.

9.3 Calibration of the detector

In order to operate the detector it must first be calibrated. In the first step we use a laser. A laser beam is adjusted to take the same path as the He beam scattered from the sample. It enters the detector through chamber V and continues in the analyzer chamber (VI) through the slit located between chambers V and VI. We then move the analyzer crystal along the z direction and adjust the positions x and y so that the laser beam always hits the crystal. This procedure allows to determine coarsely the corrective movements in x and y direction.

The calibration of the detector with the He beam begins with the determination of the parameter determining the position of the x, y, tilt, and diaphragm between the chambers VI and VII as function of the position of the z motor. The crystal is moved along the z direction by steps of about 10 mm and x, y, tilt, diaphragm, and the polar angle are then adjusted so that the intensity in the detector is maximal.

The position of the x, y, tilt, and diaphragm are fitted by a linear function. The results of these fits are given in the table 9.1.

Motor	linear coefficient	Constant
X	$3.97 \cdot 10^{-3}$	9.14
Y	$5.43 \cdot 10^{-3}$	-6.76
Tilt	$-1.84 \cdot 10^{-3}$	-0.137
Diaphragm	0.2335	0.611

Table 9.1 Coefficients for the movement of the x, y, tilt, and diaphragm in relation to z.

While the constant corresponds to the motor position at the position $z = 0$, the linear coefficient describes changes with z-position. In the case of the motors x and y it is equal to the tangent of the angle between the z-axis and the beam axis; for x it is the horizontal deviation, for y the vertical deviation. With these corrections the sample follows exactly the He beam incident from the sample in chamber IV.

The next step is finding the true value of the incident angle ϕ_i . To do so the crystal is once again scanned along the z direction in small steps (about 2 mm). At each step the intensity of the He diffracted in the detector is recorded as function of the polar position

of the crystal. Fig 9.4 shows the evolution of the width of the peak as a function of θ_i . The ideal position corresponds to the angle at which the width reaches its minimum. When two such *ideal* positions have been found for the same wavelength we can use (4.6) to calculate the values of ϕ_i and \mathbf{I} , n can be estimated without having to resort to a fit.

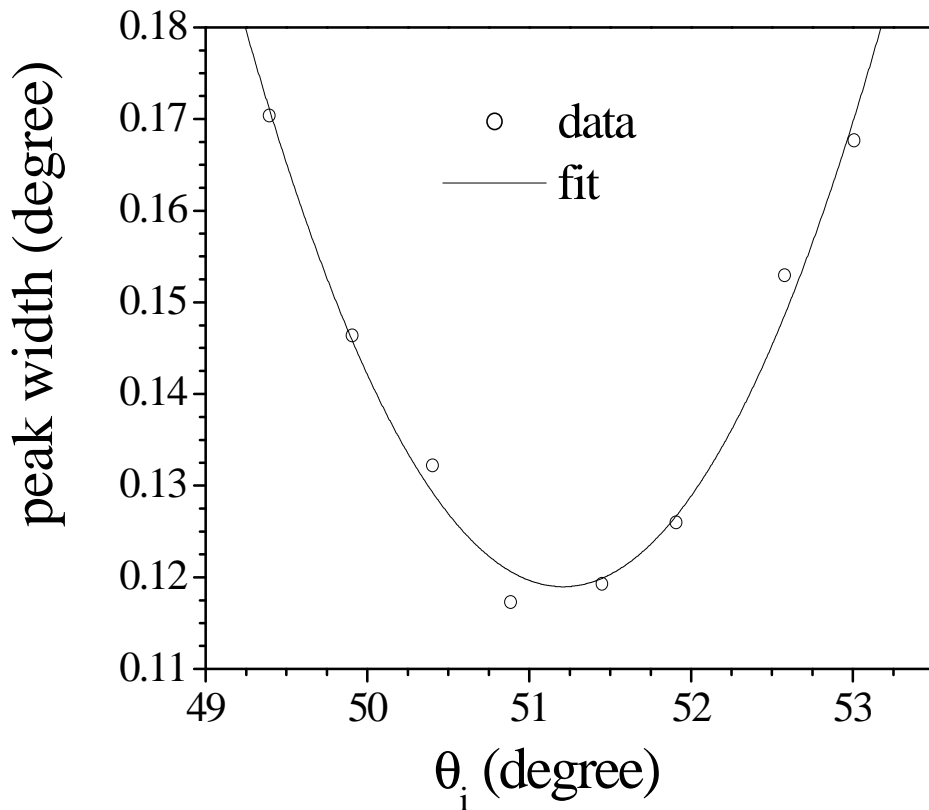


Fig. 9.4: Width of the diffracted peak as function of the incident angle. Fit is second order polynomial function.

The position $z = 0$ is then set at the z position where $\phi_i = 45^\circ$. The only missing parameter at that point is the distance l_d . This parameter is calculated making use of eq. (9.1). The valued l_d was determined in the set-up as 304.709 mm. Actually, it is in theory possible to determine the position $z = 0$, l_d , and the real position of ϕ_i only from one fit to eq. (9.1)

but in that case the fit would depend on three parameters. As the distance over which the crystal can be moved is restricted the function eq. (9.1) becomes almost linear which allows the determination of three parameters only with unacceptable large errors.

9.4 Results

After having adjusted and calibrated the motion control for the detector we measured an energy scan of the He supersonic beam, directly incident from the nozzle at a nominal temperature of 71.3 K. An energy scan of this beam is shown in the figure 9.5.

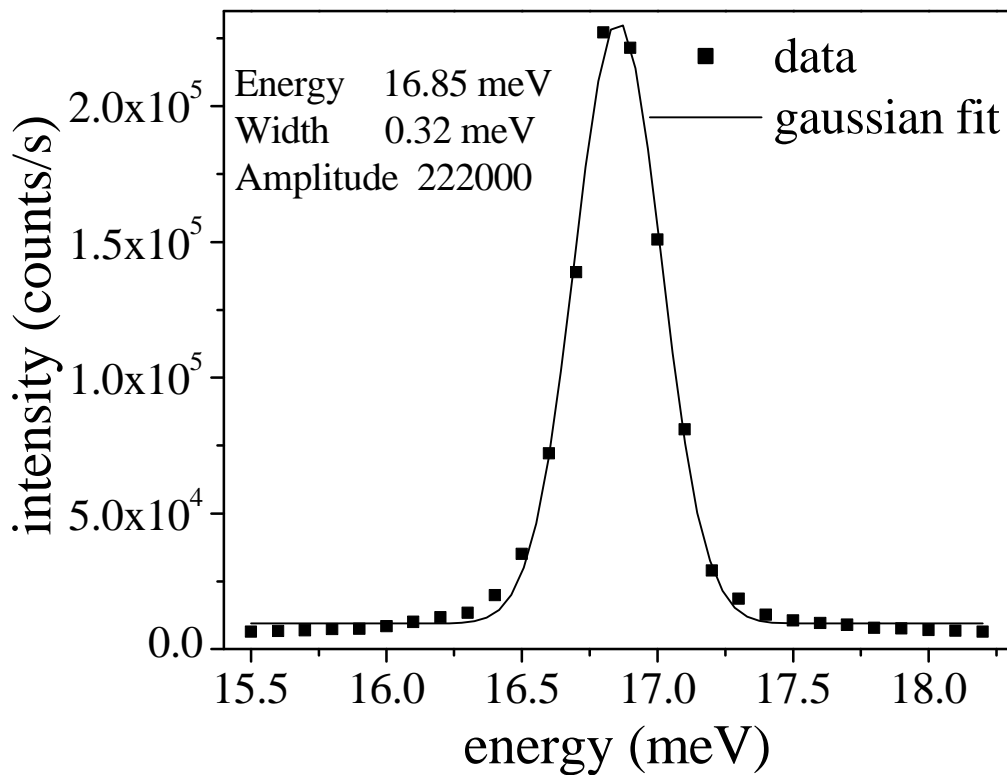


Fig. 9.5: Energy scan of a supersonic beam with nozzle temperature of 71.3 K.

A Gaussian fit of the curves give a peak at an energy of 16.85 meV with a width at half maximum of 0.32 meV ($\Delta E/E = 0.019$). The energy distribution of the beam contributes with about 1.4% to the width of the peak [81]. This means that the energy resolution of the detector is better than 1.3%.

The maximum intensity is 220,000 counts/s and the background is 5,000 counts/s ($S/N = 46$). The background counting rate is due to the background pressure in chamber VI which arises from the destruction of the beam in that chamber. In cases when we tried to do inelastic measurements (surface phonons) the background came from the scattering chamber IV, mostly. This background was probably one reason, why we did not succeed to obtain phonon spectra.

CHAPTER 10

Conclusions and Outlook

The present work focuses on growth and properties of metallic nanostructures at vicinal surfaces. We studied the growth in the range 0 to 3 monolayers and analyzed particularly the conditions for the formation of nanowires along the step edges and surface alloying.

The decoration of the Pt(997) surface by Ag, well characterized from earlier studies [3], has been employed to obtain information on the role which steps play in the sticking behavior of O₂, H₂, and CO adsorption from the gas phase. Ag step decoration was employed to change the electronic structure of the step edges without changing the substrate morphology. We find that the sticking coefficient of O₂ and H₂ is reduced by factors of 10 and 4, respectively, already by the deposition of one monatomic Ag row at the step edge (0.13 ML). No significant change for CO adsorption is observed. Because all three adsorbates preferentially occupy step sites they were all affected by the modification of the step edge. The details of adsorption pathway and energy barriers lead to the substantial differences between the three gases. In the case of O₂ the reduced sticking probability is due to a change of the chemisorbed molecular precursor state: Ag decoration shifts the partitioning between desorption and dissociative adsorption towards desorption. For H₂ it is likely that a changed adsorption site is at the origin of the reduced sticking probability as it is found that preferential adsorption after Ag decoration is no more in the vicinity of the step edges. For CO the Ag step decoration changes the adsorption energy, which is, however, not sufficient to change its sticking behavior remarkably.

The study of Fe growth on Pt(997) showed that interaction with the step forces the growth of nanowires at that step edges between surface temperatures of 175K and 600K

with optimal conditions around 300K. The high regular step density of the Pt(997) also induced the formation of a smooth first monolayer between 200K and 450K and even the formation of a relatively smooth second layer at 350K. We find evidence for the formation of a surface restricted alloy between 450K and 550K. Energy barriers of 0.32eV and 0.66eV have been obtained for the alloying process. The lower value is obtained for incomplete step decoration by Fe, the higher value for the deposition of more than 13% of a ML of Fe. Possible processes associated with those activation energies can be the exchange at the step edge or the creation of vacancies in the substrate terrace. For temperatures above 600K diffusion of Fe atoms into the Pt bulk plays an important role.

For the deposition of Rh and Mo on Pt(997) we find that Rh forms a smooth layer between 250K and 500 K. At about 700K Rh bulk diffusion begins. Between 400K and the onset of bulk diffusion it is possible to grow nanowires at the step edges. Mo is found to grow three-dimensionally on Pt(997). The formation of monatomic rows at the step edges is not observed between 150K and 500K substrate temperature. Mo is the first element to exhibit this behavior.

We studied the growth of ordered Cu-Ag and ordered Ag-Cu structures at the substrate step edges. The deposition of Ag at Cu pre-covered step edges corresponds to an energetically stable ordered structure. It was also possible to create an ordered structure with the reverse order of evaporants up to at least 250 K. This agrees well with a theoretical study suggesting that the second case which does not result in the structure with the lowest total energy can still be obtained as a metastable structure [5].

We have validated the concept of a DAS spectrometer and achieved a relative energy resolution of better than 1.3%. With the installation of smaller slits in the detector the energy resolution may still be improved to become better than TOF spectrometers.

References

1. P. Gambardella, A. Dallmeyer, K. Maiti, M.C. Malagoli, W. Eberhard, K. Kern, and C. Carbone, *Nature*, 2002. **302**: p. 416.
2. H.Brune, *Surf. Sci.Rep.*, 1998. **31**: p. 121.
3. P. Gambardella, M. Blanc, L. Bürgi, K. Kuhnke, H. Brune and K. Kern, *Phys. Rev. B*, 2000. **61**: p. 2254.
4. K. Wildberger, V.S.Stepanyuk , P. Lang, R. Zeller, and P.H. Dederichs, *Phys. Rev. Letters*, 1995. **75**(3): p. 509.
5. P. Gambardella, M. Blanc, K. Kuhnke, K. Kern, F. Picaud, C. Ramseyer, C. Girardet, C. Barreteau, D.Spanjaard, and M.C. Desjonqueres, *Phys. Rev. B*, 2001. **64**: p. 045404.
6. B. Poelsema, and G. Comsa, *Springer Tracts in Modern Physics*. Vol. Vol. 115. 1989: Springer Verlag, Berlin-Heidelberg.
7. K.Rieder, and T.Engel, *Phys. Rev. Letter*, 1979. **43**: p. 373.
8. R. Kunkel, B. Poelsema, L. K. Verheij, and G. Comsa, *Phys. Rev. Lett.*, 1990. **65**: p. 733.
9. G.Brusdeylins, R.Bruce Doak, and J. Peter Toennies, *Phys. Rev.*, 1983. **B 27**: p. 3662.
10. Toennies, J.P., *J. Vac. Sci. Technol.*, 1984. **A2**: p. 1055.
11. P. Zeppenfeld, K. Kern, R. David, K. Kuhnke, and G. Comsa, *Phys. Rev.*, 1988. **B 38**: p. 12329.
12. Marsico, V.E., *Ph.D. thesis*. 1995, Ecole Polytechnique Fédérale de Lausanne.
13. Schief, H., *Ph.D. thesis*. 1995, Ecole Polytechnique Fédérale de Lausanne.
14. J. Toennies, and K. Winkelmann, *J.Chem. Phys.*, 1977. **66**: p. 3695.
15. M.Blanc, *Diploma thesis*. 1995, Ecole Polytechnique Fédérale de Lausanne.

16. D.Y. Petrovykh, F.J. Himpsel, and Jung T, Surf. Sci., 1998. **407**: p. 189.
17. V. Marsico, M. Blanc, K. Kuhnke, and, K. Kern, Phys. Rev. Lett., 1997. **78**: p. 94.
18. P. Gambardella, M. Blanc, L. Bürgi, K. Kuhnke, and K. Kern, Surf. Sci., 2000. **93**: p. 449.
19. E. Hahn, H.Schief, V.Marsico. A.Fricke and K.Kern, Phys. Rev. Lett., 1994. **71**: p. 3378.
20. G.Comsa, G.Mechtersheimer, and B Poelsema, Surf. Sci., 1979. **89**: p. 123.
21. C.Kittel, *Introduction to solid state physics*. 1996: Wiley.
22. M. Blanc, V. Marsico, K. Kuhnke, and, K. Kern, Surf. Sci. Lett., 1998. **414**: p. L964.
23. H. Brune, H. Röder, K. Bromann, K. Kern, J. Jacobsen, P. Stoltze, K. Jacobsen, and J. Nørskov, Surf. Sci.Let., 1996. **407**: p. 379.
24. M.Blanc, *Ph.D. thesis*. 1998, Ecole Polytechnique Fédérale de Lausanne.
25. G.Mechtersheimer, *Ph.D. thesis*. 1981, Uni. Bonn.
26. Kern, K., et al., Phys. Rev. Lett., 1986. **57**(3187).
27. Zangwill, A., *Physics at Surfaces*. 1988, Cambridge: Cambridge University press.
28. Christmann, K. and G. Ertl, Surf. Sci., 1976. **60**: p. 365.
29. Kaukonen, H.-P. and R.M. Nieminen, Surf. Sci., 1991. **247**: p. 43.
30. Gee, A.T., et al., J.Chem.Phys., 2000. **112**: p. 7660.
31. Gee, A.T. and B.E. Hayden, J.Chem.Phys., 2000. **113**(22): p. 10333.
32. A. Winkler, X.Guo, H. Siddiqui, P. Hagans, and J.Yates, Surf. Sci., 1988. **2001**: p. 419.
33. A.Rar, and T. Matsushima, Surf. Sci., 1994. **94**: p. 89.
34. H.Wang, R.Tobin, D.Lambert, C.Dimaggio, and G.Fisher, Surf. Sci., 1997. **372**: p. 267.
35. B. C. Stipe, M. A. Rezaei, W. Ho, S. Gao, M. Persson, and B. I. Lundqvist, Phys. Rev. Lett., 1997. **78**: p. 4410.
36. Stipe, B.C., M.A. Rezaei, and W. Ho, J.Chem.Phys., 1997. **107**: p. 6443.
37. J.Gland, Surf. Sci., 1980. **93**: p. 487.
38. C.Cambell, G.Ertl, H.Kuipers, and J.Segener, Surf. Sci., 1981. **107**: p. 220.
39. A. Eichler, and J. Hafner, Phys. Rev. Lett., 1997. **79**: p. 4481.

40. P.J.Feibelman, S.Esch, and T.Michely, Phys. Rev.Lett., 1996. **77**: p. 2257.
41. Z.Sljivančanin, and B.Hammer, to be published.
42. Gland, J.L., Surf. Sci., 1978. **75**: p. 733.
43. Hammer, B. and J.K. Nørskov, Phys. Rev.Lett., 1997. **79**: p. 4441.
44. J.Luo, R.Tobin, D.Lambert, G.Fisher, and C.Dimaggio, Surf. Sci., 1992. **274**: p. 53.
45. P. Gambardella, and K. Kern, Surf. Sci., 2001. **475**: p. L229.
46. Hammer, B., Phys.Rev.Lett., 1999. **83**: p. 3681.
47. F.B.Monget, U.Valbusa, and M.Rocca, Surf. Sci., 1995. **339**: p. 291.
48. T. Zambelli, J. Wintterlin, J. Trost, and G. Ertl, Science, 1996. **273**: p. 1688.
49. B.Hammer, O.Nielsen, and J.Nørskov, Cat.Lett., 1997. **46**: p. 31.
50. Baró, A.M. and H. Ibach, Surf. Sci., 1980. **92**: p. 237.
51. Poelsema, B., G. Mechttersheimer, and G. Comsa, Surf. Sci., 1981. **111**: p. 519.
52. Olsen, R.A., G.J. Kroes, and E.J. Baerends, J.Chem.Phys., 1999. **111**: p. 11155.
53. Henderson, M.A. and J.T. Yates, Surf. Sci., 1992. **268**: p. 189.
54. Andzelm, J., Surf. Sci., 1981. **108**: p. 561.
55. E.E. Shalyguina, and K.H. Shin, J. Alloy. Compd., 2001. **326**: p. 298.
56. M. Zhang, F. Pan, and B.X. Liu, J. Phys.- Condens. Mat., 1997. **9**: p. 7623.
57. M. Abid, H. Lassri, R. Krishnan, M. Nyvlt, and S. Visnovsky, J. Magn. Magn. Mater., 2000. **214**: p. 99.
58. A. Simopoulos, E.D., A. Kostikas, A. Jankowski, M. Croft, and T. Tsakalakos, Phys. Rev., 1996. **B 54**: p. 9931.
59. Y.J. Kim, C. Westphal, R.X. Ynzunza, H.C. Galloway, M. Salmeron, M.A. Van Hove, and C.S. Fadley, Phys. Rev., 1997. **B 55**: p. 13448.
60. Y.J. Kim, C. Westphal, R.X. Ynzunza, Z. Wang, H.C. Galloway, M. Salmeron, M.A. Van Hove, and C.S. Fadley, Surf. Sci., 1998. **416**: p. 68.
61. Th. Schedel-Niedrig, W. Weiss, and R. Schlögl, Phys. Rev., 1995. **B 52**: p. 17449.
62. M. Ritter, W.R., and W. Weiss, Phys. Rev., 1998. **B 57**: p. 7240.
63. W. Weiss, and M. Ritter, Phys. Rev. B, 1999. **59**: p. 5201.
64. D.I. Jerdev, and B.E. Koel, Surf. Sci., 2002. **513**: p. L391.

65. D.Payer, *Diplomarbeit, 2001*. Institut für Allgemeine Physik, Wien: Technische Universität.
66. M. Croft, D. Sills, A. Sahiner, A.F. Jankowski, P.H. Ansari, E. Kemly, F. Lu, Y. Jeon, and T. Tsakalakos, *Nanostruc. Mater.*, 1997. **9**: p. 413.
67. A.F. Jankowski, G.D. Waddill, and J.G. Tobin, *J. Vac. Sci. Technol.*, 1994. **A 12**: p. 2215.
68. *Binary Alloy Phase Diagram 2nd ed.*, ed. T.B. Massalski. 1996, Ohio: ASM International.
69. A.Christensen, A.V.Ruban. P.Stoltze, H.L.Skriver, J.K.Norskov, and F.Besenbacher, *Phys. Rev.B*, 1997. **56**: p. 5822.
70. A. Atli, M. Abon, P. Beccat, J.C. Bertolini, and B. Tardy, *Surf. Sci.*, 1994. **121**: p. 302.
71. Y. Gauthier, R. Baudoing-Savois, J. M. Bugnard, U. Bardi, and A. Atrei, *Surf. Sci.*, 1992. **1**: p. 276.
72. David R. Lide, Editor in Chief, *Handbook of CHEMISTRY and PHYSICS*. 80th ed. 1999-2000: CRC Press LCC.
73. Q.J.Gao, and T.T.Tsong, *Surf. Sci.Let.*, 1987. **191**: p. L787.
74. Bassett, D.W., *Surf. Sci.*, 1995. **325**: p. 121.
75. J.Sierra, F.C.M.J.M van Delft, A.D. van Langerveld, and B.E. Nieuwenhuys, *Surf. Sci.*, 1992. **264**: p. 435.
76. D.Brown, P.D.Quinn, D.P.Woodruff, T.C.Q.Noakes, and P.Bailey, *Surf. Sci.*, 2002. **497**: p. 1.
77. E.L.D.Hebenstreit, W.Hebenstreit, M.Schmid, and P.Varga, *Surf. Sci.*, 1999. **441**: p. 441.
78. G.A.Attard, R.Price, and A.Al-Akl, *Surf. Sci.*, 1995. **335**: p. 52.
79. Gambardella, P., *Ph.D. thesis*. 2000, Ecole Polytechnique Fédérale de Lausanne.
80. R.David, K.Kern, P.Zeppenfeld, and G.Comsa, *Rev.Sci.Instrum.*, 1986. **77**: p. 2771.
81. G.Comsa, R.David, and B.Schumacher, *Rev.Sci.Instrum.*, 1981. **52**: p. 789.
82. D.-M. Smilgies, and J.Toennies, *Rev.Sci.Instrum*, 1988. **59**: p. 2185.

83. K.Kuhnke, E.Hahn, R.David, P.Zeppenfeld, and K.Kern, Surf. Sci., 1992. **27**: p. 118.
84. H. Schief, V. Marsico, and K. Kern, Rev. Sci. Instr., 1996. **67**: p. 2026.

Remerciements

J'aimerais en premier lieu remercier le Professeur Klaus Kern, pour m'avoir donné la possibilité d'effectuer ce travail dans son groupe et m'avoir dirigé au cours de cette thèse.

J'aimerais ensuite remercier le Dr. Klaus Kuhnke pour son aide ainsi que pour les corrections de ce manuscrit. Je tiens également à remercier les Dr. M. Blanc et Dr. P. Gambardella avec qui j'ai eu le plaisir de travailler au début de ma thèse.

Merci aussi à mon camarade de laboratoire Taeyon Lee.

Je tiens encore à remercier tous les membres du groupe qui ont su instaurer une bonne ambiance de travail.

Merci encore à toute l'équipe de l'atelier mécanique et d'électronique de l'Institut de Physique Expérimental de l'EPFL ainsi qu'à tous les techniciens du Max Planck Institut für Festkörperforschung de Stuttgart.

Finalement je remercie ma famille pour son soutien durant toutes ces années.

Curriculum Vitae

Nom: Samuel Sarbach

Date de naissance: 5 juin 1972

Nationalité: Suisse (Origine: St Niklaus/VS)

Formation:

1991 Maturité Fédérale de type E

1998 Diplôme en physique de l'université de Fribourg

- Branche principale : Physique expérimentale
- Branche secondaire : Mathématiques

1998-2002 Doctorant dans le groupe du Prof. K.Kern